Experimental Investigation of Rock Dynamic Geomechanical Properties at Seismic Frequencies

by

Chuan Lu

A thesis submitted in partial fulfillment of the requirements for the degree of

Doctor of Philosophy

in

Geotechnical Engineering

Department of Civil and Environmental Engineering

University of Alberta

Abstract

Time-lapse seismic reservoir monitoring has advanced quickly over the past decade to become a common technique for monitoring subsurface processes, especially for steam and CO_2 injection. It has been widely used to determine and monitor changes occurring in a reservoir during hydrocarbon production or injection of water or gas into the reservoir. Petroleum engineers can predict the evolution of pressure and temperature and the saturation of oil, gas, and water during reservoir production with time-lapse seismic data. To understand the changes in seismic attributes during oil and gas production, researchers are challenged to combine rock physics models, geomechanics and laboratory measurements. Traditional laboratory measurement of reservoir rocks is conducted in the high kHz to MHz frequency range, which differs from seismic surveys (0.1-100Hz). Additionally, dynamic moduli determined from the elastic wave velocity and static moduli derived from the slope of a stress-strain curve from a deformational experiment are different for reservoir rocks due to the different strain measurement levels. Consequently, it is valuable to measure both dynamic and static elastic properties of rocks in the laboratory on core scale samples from seismic frequencies to ultrasonic frequencies.

From this perspective, experimental research was undertaken to design reasonable and feasible experimental protocols that guide the infrastructure and process required to conduct seismic frequency dynamic property measurements under shear stress at elevated temperatures. A new experimental system within the Reservoir Geomechanical Research Group at the University of Alberta has the capacity to measure dynamic and static elastic properties at seismic and ultrasonic frequencies under deviatoric stress. This rock physics research is based on stress-strain method, and focus on the temperature, frequency (seismic – 0.01 Hz to 20 Hz) and most critically deformation (both isotropic compressibility and shear stress-induced) dependent properties of the poorly consolidated oil sands and highly overconsolidated (clay) shales associated with the McMurray and Clearwater Formations of NE Alberta. The results were shown that the frequencies within the reservoir are capable of significantly influencing reservoir properties. Acoustic impedance changes 59% at different effective pressures and up to 40% at different frequencies. An interpretation workflow based on the application of the newly gained understanding of frequency-dependent elastic properties was developed and validated by previous experimental

studies. The newly acquired seismic frequency properties can then be applied in forwarding modelling using sequentially coupled reservoir geomechanical simulations to assess whether improvements in a priori predictions of fluid saturations and steam chamber development are altered.

Preface

This thesis is an original work by Chuan Lu. The research was carried out under the supervision of Dr. Rick Chalaturnyk at the University of Alberta. The experiment design, data collection, data analysis and composition of research papers have all been completed by Chuan Lu. Several sections of the current thesis either have been published or are pending publication.

Chapter 3 was published 4th EAGE Workshop on Rock Physics 2017 as “Chalaturnyk, R.J., Lu, C.; Zambrano, G. (2017). Experimental system for seismic dynamic elastic property measurements under elevated temperature and shear deformation.”. Data collection, analysis, and manuscript writing have all been accomplished by Chuan Lu.

Part of chapter 5 and chapter 6 has been published in the SPE Annual Technical Conference and Exhibition 2019 for publication as “Lu, Chuan, Brandl, Jakob , Deisman, Nathan , and Richard Chalaturnyk. "Triaxial Testing System for Seismic Frequencies Measurements with Laser Displacement Sensors." Paper presented at the SPE Annual Technical Conference and Exhibition, Calgary, Alberta, Canada, September 2019. doi: https://doi.org/10.2118/195934-MS.” Chuan Lu was responsible for conducting the research and writing the manuscripts, and Dr. Rick Chalaturnyk was responsible for reviewing the papers and providing feedback.

Acknowledgements

I would like to express my sincere thanks to my supervisor Dr. Rick Chalaturnyk for his supervision and guidance. Dr. Rick Chalaturnyk was a constant source of encouragement during times when I struggled to get used to the new culture and to find a motivation to conduct my research. He always gives me many insightful advice and comments. During my years of study with him, I have had numerous opportunities to attend conferences and symposiums, to meet new people all around the world working in industry and academia, and to show my research and exchange ideas with others. Dr. Rick Chalaturnyk not only helped me formulate this study but also provided invaluable guidance for my future career. I am incredibly grateful for studying with Dr. Rick Chalaturnyk.

Special thanks go to Dr. Nathan Deisman for the valuable discussion with him and his great input in this research. It would be impossible to build the experimental apparatus without his kindly help. I would also like to thank Dr. Gonzalo Zambrano Narvaez for his encouragement and insight into my research.

I would like to acknowledge Jakob Brandl for his technical help in my experimental design, Gilbert Wong for his support during the experimental tests and Keivan Khaleghi for his comments and help in the lab.

I am also grateful for the friendship with people in our Reservoir Geomechanics Research Group at the University of Alberta. It is my luck to work and study with enthusiastic, considerate, and intelligent people with different cultures and backgrounds.

I wish to thank my friends for all the fantastic company and wonderful memories we had in the past years. It is a valuable experience in hiking, fishing, camping, cooking and road trip together.

I gratefully acknowledge the financial support from Energi Simulation Industrial Research Consortia in Reservoir Geomechanics for Unconventional Resources and Alberta Innovates Technology Futures (AITF).

Any amount of words would not be sufficient to express my gratitude to my family for their unfailing support, encouragement, and understanding. You are the reason for all the achievements in my life.

Table of Contents

List of Tables

List of Figures

1 INTRODUCTION

1.1 Background

Canada is the fifth-largest producer of natural gas and the sixth-largest producer of crude oil in the world, with large oil and natural gas reserves across the country. Total Canadian proven oil reserves - approximately 10% of the world's proven reserves - are estimated at 171.0 billion barrels, of which 166.3 billion barrels are found in Alberta's oil sands. Only about 20% of Alberta's oil sands are shallow enough to be mined. The remainder can only feasibly be extracted through in situ techniques such as thermal recovery processes. To image the pressure, temperature, and saturation changes during these thermal recovery operations and to distinguish areas of bypassed reserves, time-lapse seismic monitoring has been widely used in Alberta, Canada (Eastwood et al., 1994; Hiebert et al., 2014; Nakayama et al., 2008; Schmitt, 1999, 2005; Zou, Bentley et al., 2005; Landrø M, 2015; Ketineni et al., 2020; Danaei, Shahram, et al, 2020).

Time-lapse seismic monitoring is the process of acquiring and interpreting multiple seismic surveys repeated at the same site over calendar time after a period of oil, gas, or water production or fluid injection (Lumley, 2001). Seismic time-lapse monitoring provides a petroleum engineer with surveillance data on the likely volume and shape of the zones in the reservoir affected by a particular recovery process. As a result, seismic time-lapse monitoring helps determine the need for and location of infill wells or provide options for modifying thermal operating parameters (e.g., steam cycle length, steam volumes and rates, and multiwell steaming patterns) (Vanorio et al., 2011; Al Hosni et al., 2016). Time-lapse seismic methods were first reported by Winkler and Nur (1982), where they discussed the potential application for monitoring thermal recovery projects based on the mechanics of seismic attenuation. Isaac (1996) researched seismic methods for heavy oil reservoir monitoring and demonstrated that the use of the time-lapse seismic techniques can provide refined input into the reservoir simulation models. Jenkins et al., (1997) determined that time-lapse seismic monitoring could enhance injector profile management even in the heterogeneity of sandstone reservoirs. Sun (1999) developed new reservoir characterization and monitoring technologies by using time-lapse seismic data and analysis methods. Lumley (2001) summarized the advantage of time-lapse seismic techniques and defined a risk analysis workflow to examine the feasibility of using time-lapse seismic. Zou et al., (2006) presented a practical

procedure for using reservoir simulation results to generate synthetic time-lapse seismic responses. Relevant to this research, Kato et al. (2008) studied the change of elastic properties in a bitumen reservoir during steam injection. Hiebert et al. (2014) ran several SAGD simulations to determine how steam or gas chamber volume, stress and temperature change induced volume changes would impact a time-lapse seismic survey. To integrate time-lapse seismic methods with reservoir simulation, improved rock physics models that would help improve our understanding of reservoir processes should be developed (Wang, 1997, 2001; Ruiz and Cheng, 2010; Vanorio, Nur and Ebert, 2011).

However, lab measurement of dynamic properties at seismic frequencies is uncommon due to the challenge of obtaining the data in the seismic frequencies range. (Spencer, 1981; Jackson and Paterson, 1987; Paffenholz and Burkhardt, 1989; Batzle et al., 2006; Tisato and Madonna, 2012; Madonna and Tisato, 2013; Mikhaltsevitch et al., 2014b; Szewczyk et al., 2018; Mikhaltsevitch et al., 2021). To extract rock and fluid properties information from seismic data, laboratory measurements are essential for a better understanding of physical mechanisms that are dominant at seismic frequencies. In addition, the immature linkage between rock physics and geomechanical deformations presents challenges for including the rock property changes (e.g., volume change) in time-lapse seismic interpretations which is essential during SAGD production and gas injection (Zhang and Okuno, 2015).

To simulate the strain-induced from a seismic wave travelling through the formation, the strain within a test specimen should be smaller than 10^{-6}, where attenuation is linear (Iwasaki et al., 1978; Winkler and Nur, 1979). Piezoelectricity was widely used as a force generator for seismic frequency measurement, but the force generated by the piezoelectric technique was too small and only small specimens could be used for testing. Full triaxial stress condition testing could not be conducted by using piezoelectric due to capacity restraints.

Most researchers use strain gauges as a displacement sensor. Specimens need to be polished very well to attach the strain gauge, but the strain gauge measurement is only a point measurement and is likely influenced by isotropic behaviour and fractures. Strain gauges are also highly temperature-dependent, making them challenging to use in tests at elevated temperatures. Another disadvantage of the existing seismic frequency measurement infrastructure is that specimens are loaded under

hydrostatic pressure conditions, so combining typical geomechanical triaxial test conditions with seismic frequency rock physics tests is uncommon but is increasingly the focus of research.

1.2 **Problem Statement**

There is a practical case study from Kato et al., (2008) for time-lapse interpretation where several ultrasonic laboratory measurements were made under varying differential pressure and temperature conditions. By combining the data and employing the Gassmann equation, he calibrated the velocity dispersion and built a sequential model adapted for the low-frequency band of the surface seismic data. From the study results, an approach to predict elastic property changes induced by steam injection was generated. However, for steam injection, unconsolidated sediments will undergo shear volume changes as well as isotropic compressibility-related volume changes. These shear-induced volume changes were not included in Kato's study. Figure 1-1 illustrates the volumetric and axial strain changes that can occur during a triaxial test. In this example, the specimen dilates (i.e., volume increases) during the test which alters the porosity and density. Given the dependence of the compressional and shear wave velocity on density, these values will change as a function of shear-induced volume change. While compressibility-related volume change (i.e., hydrostatic stress changes) is the primary loading path for most rock physics experiments, the focus of this reservoir geomechanics research is the variation in seismic frequency dynamic properties under shearing conditions.

Figure 1-2a illustrates how amplitude and frequency cover many magnitudes for different applications and measurements of rock elastic and anelastic properties. Figure 1-2b shows how velocity dispersion for different methods can vary widely over a range of frequencies. The additional experimental results (Islam and Skalle, 2013) illustrated in Figure 1-3 show that static Young's modulus and Poisson's ratio changed 40% and 50%, respectively, under shear deformation. To better understand the influence of shear deformation on dynamic elastic properties, it is important to combine static measurement, seismic frequency measurement, and ultrasonic measurement to calibrate the velocity dispersion. Using an experimental system that covers these frequency ranges will allow us to determine parameters for the low-frequency band rock physics model.

If we ignore these effects from rock deformation and frequency, utilizing the results from the Kato et al. (2008) case study would be misleading (Figure 1-4). What if the shear wave velocity is not affected by the pressure and temperature and what if the compressional wave velocity contributes to the interpretation? More data are needed at seismic frequencies under shear stress to calibrate the velocity model under shear stress conditions.

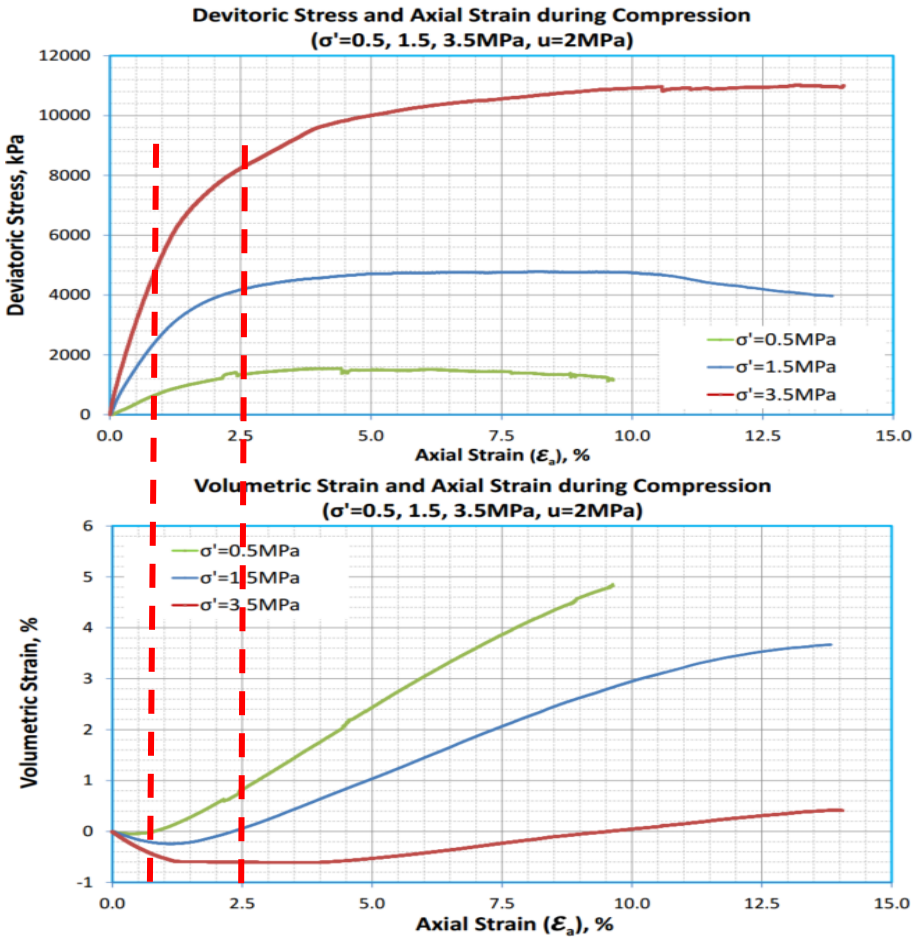

Figure 1-1 Example of three triaxial tests under different effective confining stresses to illustrate the volume changes that occur during triaxial deformation of unconsolidated sands.

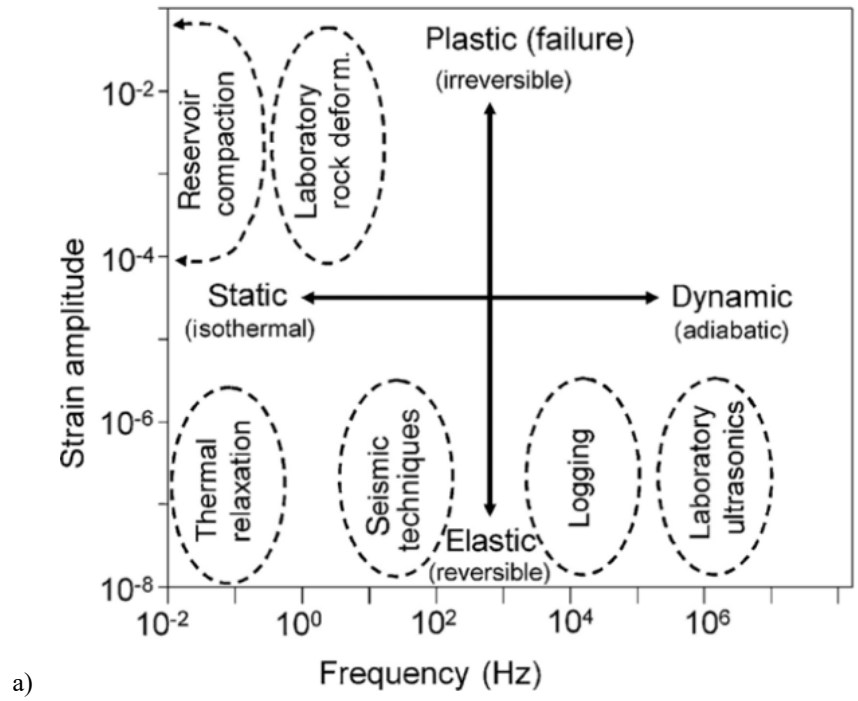

a)

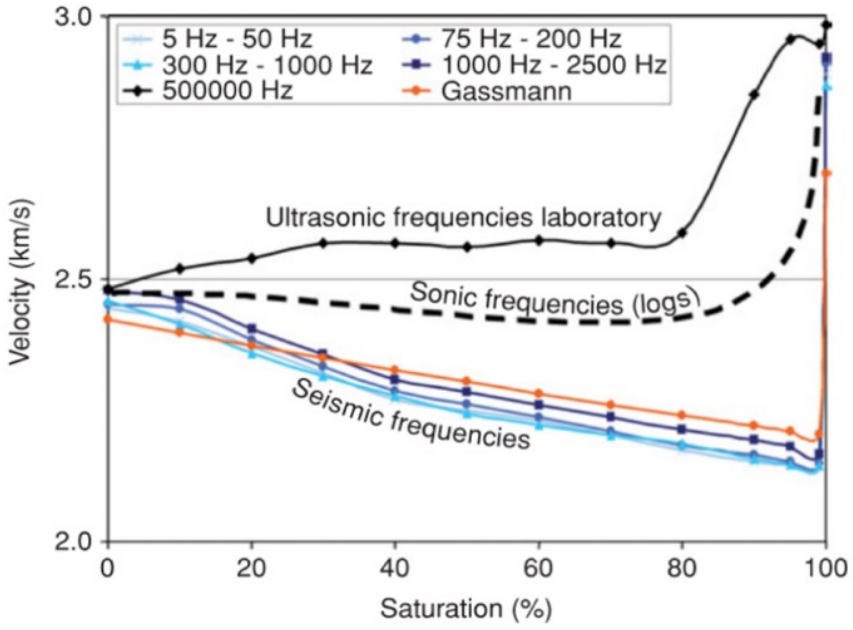

b)

Figure 1-2 a) chart of deformation processes over a wide range of frequencies and amplitudes and b) an example of velocity dispersion at various degrees of saturation (Batzle et al., 2006).

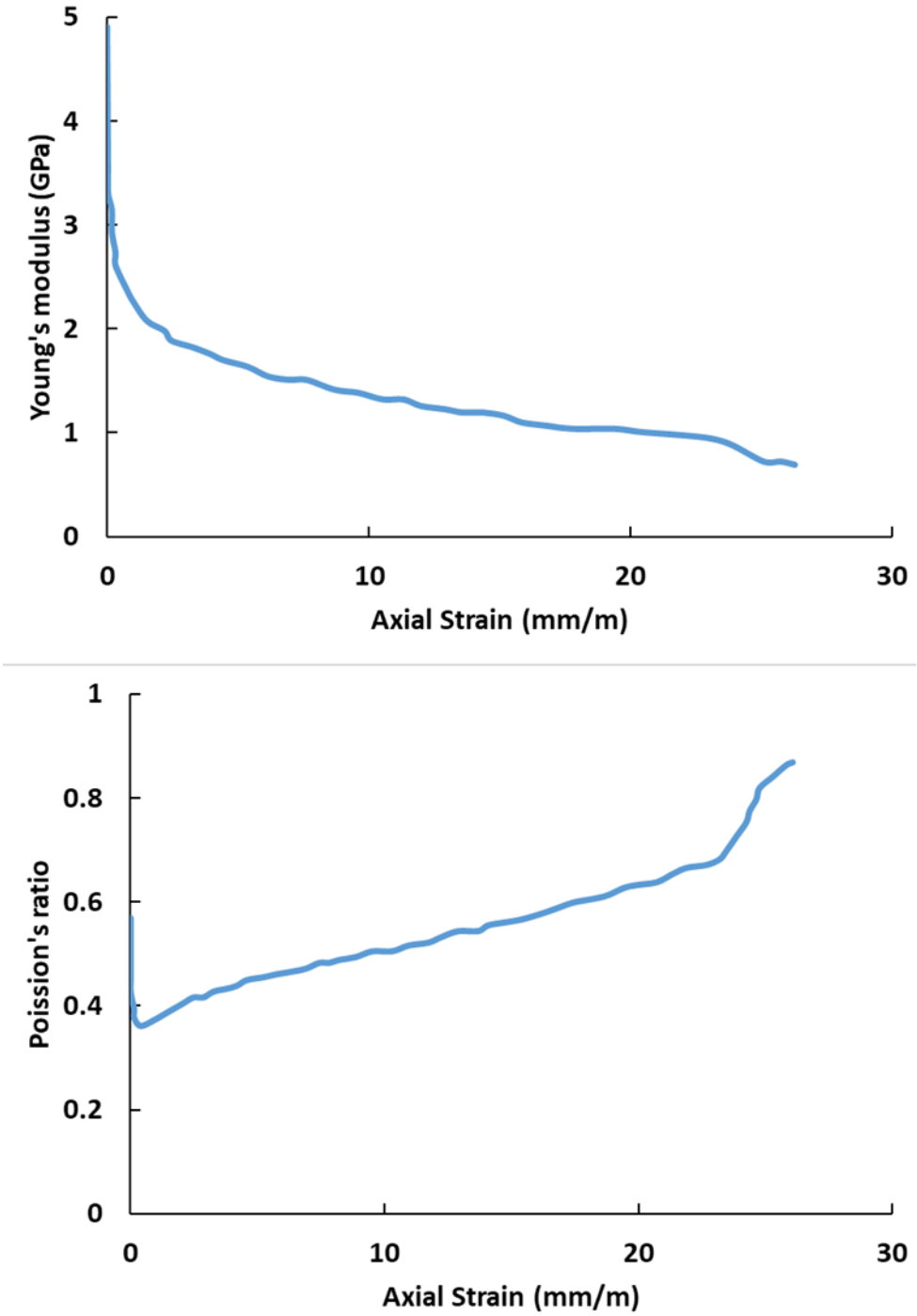

Figure 1-3 Example of the changing of Young's modulus and Poisson's ratio under shear deformation, modified from (Islam and Skalle, 2013).

As highlighted in Table 1-1, experimental systems that will permit examining how seismic frequency dynamic elastic properties vary during triaxial shear tests are not common and pose significant engineering challenges in their construction and operation. Seismic velocity cannot be identified directly because the seismic wave (at least 30m) is too long to obtain at the laboratory. To obtain seismic velocity in the laboratory, stress-strain techniques must be applied but as noted earlier, strain under the influence of a seismic wave is very small. To combine seismic frequencies measurement and static measurement, a relatively large load cell is needed with a force generator that could generate a small uniform sine wave force. However, the challenge is that the higher resolution load cell must have a small load capacity. Combining static moduli and seismic dynamic moduli with a single load cell within the testing system will not work and, due to the limitations of the load cell, the existing load cell cannot be used in the seismic measurement.

The strain induced by a seismic wave is up to 10^{-6}, which means for a 5-inch length sample, it is near nm scale measurement. The second challenge is therefore measurement at the nm scale during vibration. Strain gauges are widely used in geotechnical applications, however, few of them have the capacity for seismic measurement application. Anisotropy widely exists for the natural samples, but strain gauge only measures local strain and is highly sensitive to temperature. The workflow outlined in Figure 1-5 has been followed to solve these problems.

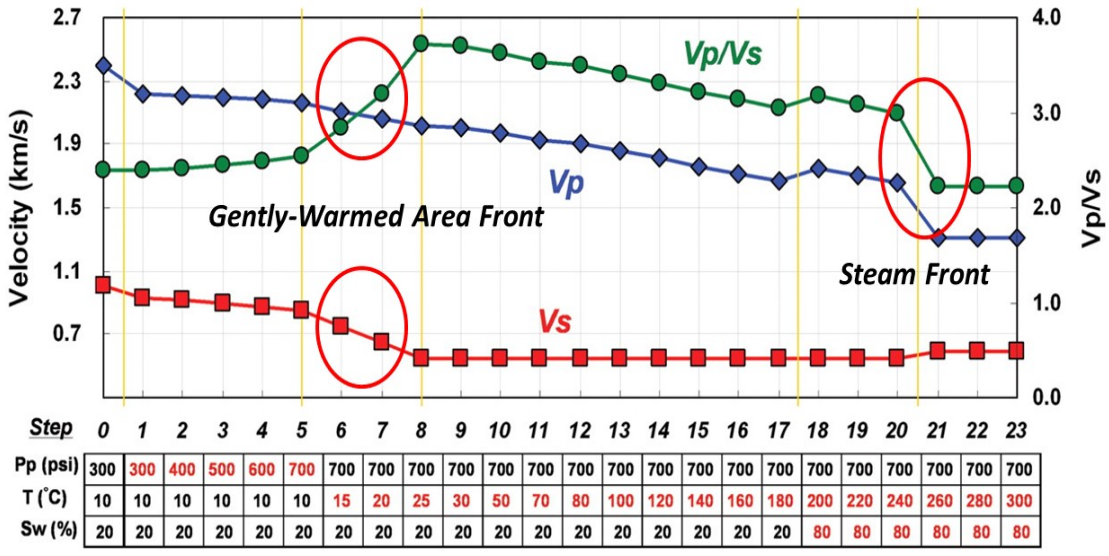

Figure 1-4 Sequential P- and S- wave velocities and VP/VS ratio changes induced by steam injection. Sequential reservoir condition changes are represented by 23 steps (Kato, Onozuka and Nakayama, 2008).

Table 1-1 Comparison of forced oscillation setups.

	Sample Length × diameter	Displacement Sensor	Frequency Range (Hz)	Confining Pressure (MPa)	Deviatoric Stess	Temperature ( )
Spencer (1981)	140×38.1	Capacitive Transducer	4-400	70 (Nitrogen)	No	No
Paffenholz and Burkhardt (1989)	150×50	Inductive Transducer	0.03-300	No	No	No
Batzle *et al.* (2006)	45×30	Strain Gauges	1-2000	10 (Nitrogen)	No	No
Takei et al. (2011)	15×32.5	Laser Displacement Sensor	0.001-10	No	No	40
Tisato and Madonna (2012)	250×76	Strain Gauges	0.01-100	25(Oil)	No	No
Madonna and Tisato (2013)	60×25.4	Linear Varialbe Differential	0.01-100	50 (Argon)	No	No
Mikhaltsevitch et al. (2014)	70×38	Strain Gauges	0.1-400	70 (Oil)	No	No
Szewczyk et al. (2016)	50.8×25.4	Strain Gauges	1-155	5-20 (Oil)	Yes	No

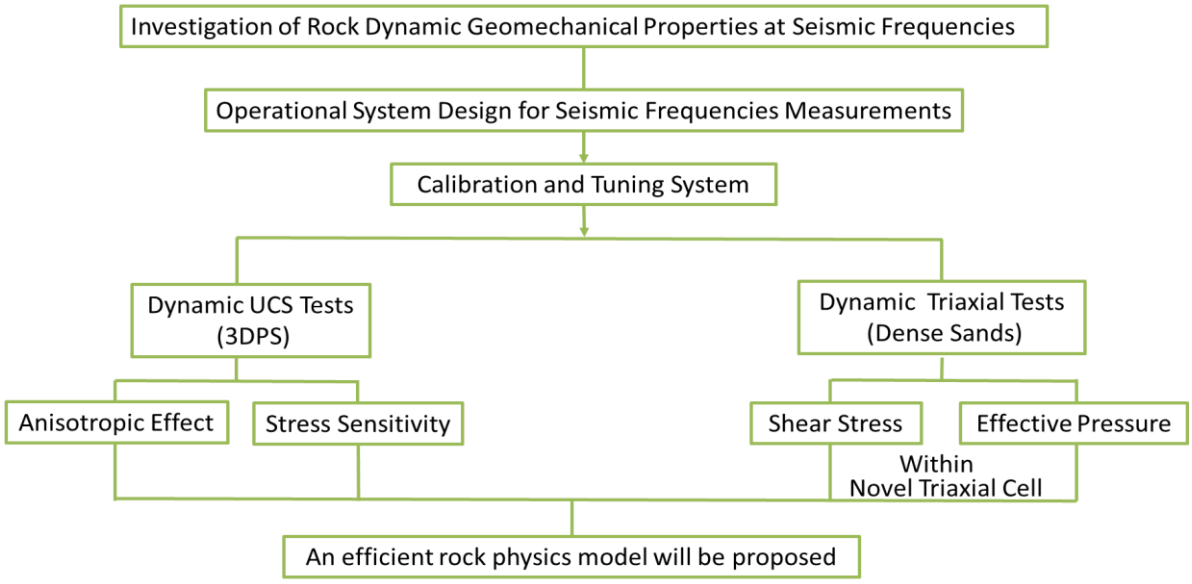

Figure 1-5 Workflow developed for this research study.

1.3 **Hypothesis**

It is known that large deformations of a reservoir in high pressure and temperature conditions will have a significant effect on both porosity and permeability. Thus, assuming hydrostatic and no

shearing conditions exist in the reservoir may cause errors in the application of time-lapse seismic simulation for reservoir management since porosity, permeability and density will change during the shear deformation. If we measure dynamic geomechanical properties at seismic frequencies under shearing conditions, existing rock physics models can be updated with the experimental results. The dynamic geomechanical properties error between hydrostatic condition and shearing condition will be minimized to be within the range of uncertainties of seismic modelling.

Currently, stress-strain techniques are the only way to obtain seismic velocity in the laboratory since seismic frequency wavelengths are in m scale. A servo-hydraulic load frame will be used to generate a small uniform sin wave force at seismic frequencies to control the strain below 10^{-6} which is the same as seismic velocity in actual reservoir conditions. A pair of laser displacement sensors are used to measure the vertical displacement during the cyclic tests. By using this technique, seismic velocity will be used for updating the rock physics model.

1.4 **Research Objectives**

The objective of this research is to develop a seismic frequencies measurement system to investigate both static and dynamic properties of dense sand samples under shear deformations. The objectives of this study are as follows:

1) To review and understand the mechanism of seismic velocity dispersion and attenuation which are affected by rock and fluid properties, the boundary conditions and inhomogeneities of this rock-fluid system in unconventional resource formations such as oil sand, bitumen carbonates, and shale;
2) To design reasonable and feasible experimental protocols that can conduct seismic frequencies dynamic property measurement at elevated temperatures under shear deformations;
3) To conduct UCS tests by using 3D printer samples to determine the impact of stress and frequencies on the dynamic properties of 3D printed samples with different bedding orientations and discontinuities;

4) To conduct triaxial tests by using artificial dense sand at seismic frequencies to determine the static and dynamic properties. Material property characterization focussed on frequencies, volume change, compressibility and stress-strain-strength;
5) To investigate the effect of frequencies and rock deformation on the dynamic properties of dense sand to verify the application of field 4D seismic interpretation template using for the SAGD process.

1.5 **Outline of thesis**

This thesis is subdivided into seven chapters. A short description of the contents of each chapter is given below.

Chapter 2 reviews the existing seismic frequencies measurement setups and rock physics models and discusses the advantages and disadvantages of the existing setups.

Chapter 3 introduces the equipment (MTS and sensors) used for this research as well as the tuning and the operation procedure.

Chapter 4 presents the 3D printed sample geomechanical properties. The 3D printed samples are printed by different orientations.

Chapter 5 provides the design of the triaxial cell for the seismic frequencies dynamic test and the calibration method using several standard samples.

Chapter 6 describes the oil sand preparation and the triaxial test procedure. Discusses the experiment results and compares them with others' results. Interpretation templates for time-lapse seismic are proposed.

Chapter 7 summarizes the work and provides some general conclusions including suggestions for improvements to the experimental setup.

2 LITERATURE REVIEW

2.1 **Elastic Wave Theory**

Seismic survey is an important method commonly used to gather information about the characteristics of geological structures and monitor fluid distribution during production. The P-wave and the S-wave are the two main types of seismic body waves, which are both linearly polarized in the isotropic medium. Rock properties could be described in terms of their elastic moduli by combining with measurement of density or porosity. According to Hooke's law, the simplest equation is the equation of linear elasticity:

$$\sigma_{ij} = C_{ijkl}\varepsilon_{kl} \qquad i,j,k,l = 1,2,3 \tag{2-1}$$

where σ_{ij} is related stress, $C_{ijkl}$is elastic stiffness, and $\varepsilon_{kl}$is strain.

The infinitesimal strain can be described by

$$\varepsilon_{kl} = \frac{1}{2}\left(\frac{\partial u_k}{\partial x_l} + \frac{\partial u_l}{\partial x_k}\right) \qquad k,l = 1,2,3 \tag{2-2}$$

and combined with the time derivative of the equation for linear momentum

$$\frac{\partial \sigma_{ij}}{\partial x_j} = \rho \frac{\partial^2 u_i}{\partial t^2} \qquad i,j = 1,2,3 \tag{2-3}$$

to give the full elastic wave equation:

$$\rho \frac{\partial^2 u_i}{\partial t^2} - \frac{\partial}{\partial_{x_j}}\left[\frac{1}{2} C_{ijkl}\left[\frac{\partial u_k}{\partial x_l} + \frac{\partial u_l}{\partial x_k}\right]\right] = 0 \qquad i,j,k,l = 1,2,3 \tag{2-4}$$

where u is displacement, x is position, ρ is rock density and t is time.

Owing to the symmetries of the stress and strain tensors,

$$C_{ijkl} = C_{jikl} = C_{ijlk} = C_{klij} \quad i,j,k,l = 1,2,3 \qquad 2\text{- }5$$

So the equation 2-4 will be reduced to:

$$\rho \frac{\partial^2 u_i}{\partial t^2} - \frac{\partial}{\partial_{x_j}} \left[C_{ijkl} \frac{\partial u_k}{\partial x_l} \right] = 0 \quad i,j,k,l = 1,2,3 \qquad 2\text{- }6$$

For the isotropic case, only two constants are required when all stress directions are equivalent, and Hooke's law is obtained:

$$\sigma_{ij} = \lambda tr\varepsilon\delta_{ij} + 2\mu\varepsilon_{ij} \qquad 2\text{- }7$$

where λ and μ are Lame's coefficients, μ is the shear modulus and the term δ_{ij} is the Kronecker's delta:

$$\delta_{ij} = 0 \quad j \neq i \qquad 2\text{- }8$$

$$\delta_{ij} = 1 \quad j = i \qquad 2\text{- }9$$

So the Hooke's law is alternatively written:

$$\varepsilon_{ij} = \frac{1+\upsilon}{E}\sigma_{ij} - \frac{\upsilon}{E} tr\sigma\delta_{ij} \qquad 2\text{- }10$$

where E and ν are Young's modulus and Poisson's ratio, so:

$$\lambda = \frac{E\nu}{(1+\nu)(1-2\nu)} \qquad 2\text{- }11$$

$$\mu = \frac{E}{2(1+\nu)} \qquad 2\text{- }12$$

These moduli relate back to the P-wave velocity,v_P, and the S-wave velocity, v_S. In an isotropic case:

$$v_P = \sqrt{\frac{K + \frac{4}{3}\mu}{\rho}} = \sqrt{\frac{\lambda + \frac{4}{3}\mu}{\rho}} = \sqrt{\frac{\left(\frac{\mu(4\mu - E)}{3\mu - E}\right)}{\rho}} \quad 2\text{- }13$$

$$v_S = \sqrt{\frac{\mu}{\rho}} \quad 2\text{- }14$$

It should be noted that the moduli given in equations 2- 13 and 2- 14 are the dynamic moduli, which can deviate significantly from the static moduli, as discussed in the following section.

2.2 **Static and Dynamic Moduli**

Commonly, the elastic moduli calculated from elastic wave velocities and density are the dynamic moduli while the static moduli are obtained from deformational experiments. Corresponding static and dynamic moduli are equal for a linearly elastic material. However, static, and dynamic moduli deviate significantly for heterogeneous materials like porous rocks (Simmons and Brace, 1965; Walsh, 1965; Fjær, 2015). Static moduli describe a material's response to strain rates normally smaller than 10^{-2} s^{-1} with large amplitudes. However, dynamic moduli are the measurement of material response to quick stress oscillations where the strain rate is typically 1-10^{-4} s^{-1} and the amplitude is small where the strain is typically less than 10^{-6} (Winkler et al., 1979; Fjaer, 2019). Because of the nonlinear stress-strain relationship for rocks, the strain amplitude is the most significant difference between measurements of static and dynamic moduli. Additionally, rocks are often inelastically affected by frictional sliding across microcracks and grain boundaries during deformation. Several processes may be involved during deformation. For example, minor fractures and internal deformation are more likely to occur during a big strain experiment than small strain cycling testing. The relevant strain rate for a dynamic modulus is primarily given by the frequency of the elastic wave (Fjær, 2015). The strain rate is potentially another important reason for the difference between static and dynamic moduli. The rock's resistance against deformation may depend on the strain rate. The strain rate associated with a static modulus depends on the loading conditions, like confining pressure or pore pressure but the frequency of the elastic wave is key for a dynamic modulus. The strain associated with an elastic wave can be expressed as $\varepsilon = \varepsilon_0 sin(2\pi f)$, where f is the frequency and ε_0 is the strain amplitude. The average strain rate associated with the wave is:

$$\langle \dot{\varepsilon} \rangle = \frac{1}{T}\int_0^T \left|\frac{\partial}{\partial t}\varepsilon\right| dt = \frac{2\pi f}{T}\int_0^T |cos(2\pi f t)| dt = 4 f \varepsilon_0 \quad \text{2-15}$$

where $f = \frac{1}{T}$. By comparing the strain rates, we also could conclude that the moduli are frequency dependent. This will be explained in the following section 2.3.

2.3 **Velocity dispersion**

Velocity dispersion refers to the dependence of seismic wave speeds on the frequency of the seismic wave (Winkler and Nur, 1982; Schijns et al., 2018). All materials have a loss mechanism in micro-structures. Therefore, the energy is absorbed and decays with propagation distance x and time t according to:

$$A(x,t) = A_0 e^{-\alpha x} e^{i(\omega t - k_r x)} = A_0 e^{i(\omega t - k^* x)} \quad \text{2-16}$$

where $A(x,t)$ is amplitude, α is the attenuation coefficient, ω is the angular frequency, x is the distance from the origin, $k_r = \frac{\omega}{c}$ is the real part of wavenumber, and t is the time.

The quality factor Q is often used to calculate attenuation (O'Connell and Budiansky, 1978). The loss mechanism could be more easily conceptualized by using Q. So, Q is the 2π times the ratio of the energy stored (E) to that dissipated (ΔE) per cycle:

$$Q = \frac{2\pi E}{\Delta E} \quad \text{2-17}$$

The mechanisms behind attenuation have been widely discussed (Biot, 1956a; Zemanek and Rudnick, 1961; Paffenholz and Burkhardt, 1989; Lienert and Manghnani, 1990; Dvorkin et al., 1995). Extrinsic attenuation and intrinsic attenuation are two types of mechanisms that lead to attenuation.

For extrinsic attenuation, the energy of a seismic wave is conserved but distributed. The energy density decreases as the seismic wave propagates. Extrinsic attenuation includes:

1. geometric spreading (Klimentos, 1991): the energy of a spherical wave radiating from a point source is propagating over an increasing sized spherical surface;
2. scattering (Mavko et al., 2009): the energy of the seismic wave is scattered due to heterogeneity of the medium; and
3. multi-pathing: a form of scattering resulting from refractions and reflections.

For intrinsic attenuation, wave energy is lost into other forms of energy, such as heat and many theories have been proposed for this mechanism. The birth of rock physics occurred with the establishment of initial theories for the propagation of elastic waves in a system composed of a porous elastic solid saturated by a viscous fluid (Gassmann, 1951; Biot, 1956a, 1956b). These initial theories treated rock as a homogenous medium. Gassmann's relation is one of the most widely used theories to predict the effects of saturation, or of fluid substitution within a saturated rock:

$$K_{sat} = K_{dry} + \frac{\left(1 - \frac{K_{dry}}{K_0}\right)^2}{\frac{\emptyset}{K_{fl}} + \frac{(1-\emptyset)}{K_0} - \frac{K_{dry}}{K_0^2}} \quad 2\text{-}17$$

$$\mu_{sat} = \mu_{dry} \quad 2\text{-}18$$

where K_{sat} is the bulk modulus of the saturated rock, K_{dry} is the modulus of the dry rock with no pore fluids, K_0 is the modulus of the constituent mineral of the rock, K_{fl} is the bulk modulus of the pore fluid, and ϕ is the porosity of the rock. The theory requires the shear modulus to be invariant to saturation, which is widely held to be true at low frequencies.

Biot theory, also known as the global flow mechanism, considers inertial flow and the relative motion between the solid rock frame and the pore fluid but does not consider heterogeneity which is universal in real rocks.

White (1975) proposed patchy saturation by studying wave propagation in porous rocks with mixed fluid saturation. This mechanism does include consideration of heterogeneity. Fluid heterogeneities exist on a scale that is greater than the pore scale, but less than the wavelength scale (Toms *et al.*, 2006). Squirt flow is proposed to consider flow between cracks and microscopic

pore structure (Mavko and Nur, 1975; O'Connell and Budiansky, 1978; Dvorkin and Nur, 1993; Dvorkin et al., 1995). This mechanism contributes most to attenuation at 100Hz – 1MHz. At lower frequencies, pore fluids can move more easily, which gives rise to more viscous friction loss and squirt-flow and leads to more attenuation. At higher frequencies, pore fluids cannot move completely and make the material stiffer. Squirt-flow mechanisms lead to frequency dependence, f_{sq}, as:

$$f_{sq} \cong \frac{K_0 \alpha^3}{2\pi\eta} \qquad 2\text{-}19$$

where K_0 is the bulk modulus of the intact medium and α is the crack aspect ratio.

From all these mechanisms, we can conclude the wave velocity is frequency-dependent. The velocity will increase as the frequency increases. At the same time, the attenuation will peak when the velocity increases very quickly. Because the modulus of fluid is much bigger than the modulus of gas, the velocity of the sample filled with fluid is higher than the sample filled with gas. The attenuation is "0" when the viscosity is very high because it takes longer for pore pressure to reach equilibrium. For low frequency, low permeability, and low pore pressure samples, squirt-flow can explain seismic attenuation. Extensional wave attenuation is dependent on saturation history, as well as the degree of saturation and boundary flow conditions. Two mechanisms giving rise to dispersion and frequency-dependent anisotropy are scattering of seismic waves by preferentially aligned inhomogeneities and fluid flow in porous rocks with micro-cracks and macro-fractures.

Frequency as well as other material properties such as porosity, fluid saturation, stress, and temperature will affect velocities. Each of these parameters will change significantly under triaxial testing conditions. This research will utilize reconstituted dense sand specimens, so the following sections discuss how these parameters can influence velocities under triaxial compression shear tests.

2.4 **Velocities vs. Porosity**

Porosity is defined as the ratio of pore volume to total volume, which has a significant influence on the elastic properties and velocity of a material. In 1958, Wyllie et al,. (1958) derived the

empirical equation, time-average equation, which is a volume-weighted average of the travel times in the solid and fluid phase. The formula states that:

$$\frac{1}{v_p} = \frac{\varphi}{v_f} + \frac{1-\varphi}{v_s} \qquad 2\text{-}20$$

where v_p is velocity measured, v_f is velocity in the saturated fluid, v_s is velocity in the rock solid, and φ is porosity.

The results (Wang, 1988; Batzle and Wang, 1992) show that both wave velocities will decrease by up to 50% with increasing porosity. However, the result also proved that the porosity dependence will change with fluid saturation, as fluid saturation will change the density of the sample and the bulk modulus.

Porosity changes under shear deformation. At the beginning of the triaxial compression shear tests, dense sand contracts and porosity decreases as the deviatoric stress increases. Plastic geomechanical dilation occurs if the deviatoric stress reaches the yielding point. Such geomechanical dilation is expected to greatly increase porosity. At the end of testing, the specimen porosity was larger than it had initially been.

2.5 **Velocities vs. Fluid Saturation**

Fluid in the rock sample will affect both the bulk modulus and the density. The relationship between velocity, bulk modulus, and density are (Equation 2-13 and Equation 2-14). For compressional velocity, when dry rock becomes saturated, the velocity may increase or decrease, but for shear velocity, the velocity will decrease since G is not affected by the fluid saturation.

Gregory (1976) conducted several tests to show the variation of P-wave velocity with full and partial water saturation. From Figure 2-1, we could conclude that the velocity in dry rock is smaller than the velocity in a saturated sample. The explanation is that the pores are more difficult to compress when the rock is saturated so the P-wave velocity will increase. For samples with higher porosity, the density of the fluid will dominate the velocity, so the velocity will decrease. When the rock becomes saturated, the rock will trend to the stiffer material, so the velocity will increase.

However, this phenomenon is generally not applied to tight sandstone because the density of the fluid is not essential for tight sandstone.

For time-lapse seismic applications, the effect of different types of fluid with variable saturation is important. Laboratory data will help us identify the movement of the fluid and distinguish the oil and water zones. We should, however, pay attention to the ultrasonic data as the elastic-stiffening effect is significant at high frequencies. Therefore, the density effect is not easily found in the laboratory. This research will utilize reconstituted dense sand specimens that will be resaturated in a triaxial system. The issues identified for fluid saturation require that careful attention is given to the degree of saturation of the test specimens prior to conducting dynamic property measurements.

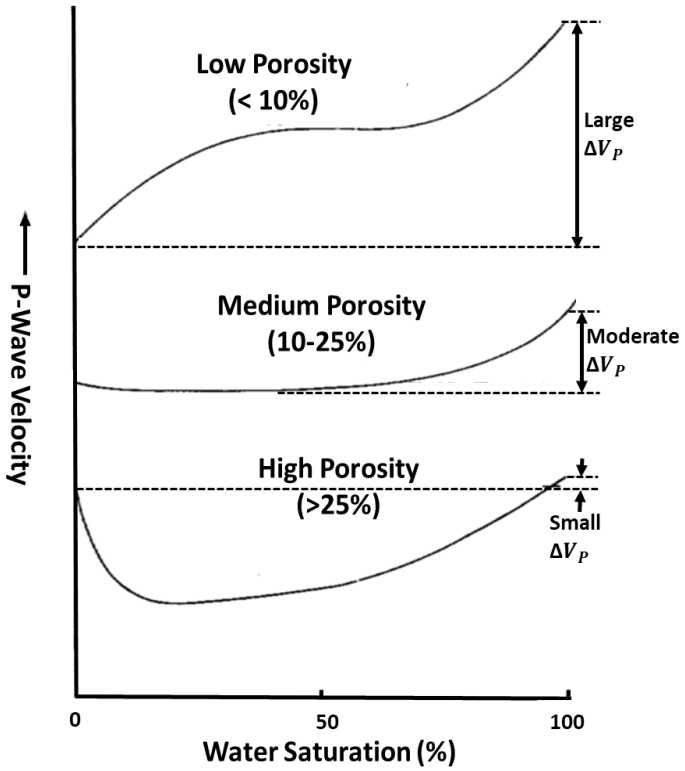

Figure 2-1 Characteristic behaviour of velocity as a function of water saturation for consolidated sediments and confining pressure of 35 MPa (Modified from Gregory, 1976).

2.6 **Velocities vs. Stresses**

From many tests (Han, 1986; David et al., 2013), we could observe that the wave velocity is strongly stress-dependent at low stress. This is because grain-to-grain contact and/or microcrack closure will improve with external stress. However, the velocity is less affected by the pressure at high pressure because grain contacts will be surrounded by the fluid that is insensitive to the pressure. In addition to the total stresses applied to the rocks, effective stress is also important and is defined by,

$$\sigma' = \sigma - \alpha p_p \qquad 2\text{-}21$$

where $\sigma'$is effective stress, σ is total stress, α is related to the degree of saturation of the soil and p_p is pore water pressure.

If the pore water pressure increases, the elastic stiffness will decrease with opening cracks and flaws. We know that velocity is more sensitive to saturation - the pore water pressure can also change saturation as gas in and out of the solution. and.

During the SAGD process, the stress change and steam injection will lead to new faults or fractures. This can be expected to have a significant effect on the 4D seismic response. This research developed a novel triaxial testing system with controllable pore pressure and confining pressure to conduct dynamic property measurements under shear deformation.

2.7 **Temperature-Dependent Wave Velocities**

Temperature has a relatively minor influence on wave velocity in rocks within most temperature ranges of interest. The velocity increases by only 7% as the temperature rises from 10 ℃ to 100 ℃ (Xu and White, 1995). As temperature increases the velocity will decrease because the bulk modulus of the pore fluid and the mineral will change.

Although the effect of temperature is slight, it does influence saturated rocks. As discussed previously, the saturation of the specimens significantly affects the velocity of a rock (e.g., the

viscosity of the saturating fluid and phase changes). If we then consider temperature-dependent wave velocities, attention should be paid to other factors. For seismic frequency measurement, data is rare at elevated temperatures due to the engineering challenge of displacement sensors and load cells. One of the goals of the research was to develop a technique that would allow triaxial tests to be conducted up to temperatures of 200 ℃. Previous research in this area is discussed in the following sections.

2.8 **Laboratory Measurement Methods**

Methods to measure velocity in the laboratory can be separated into three categories based on the frequency ranges. The three methods are ultrasonic measurement (kHz to MHz range), resonance bar techniques (from 0.1 kHz to 50 kHz) and forced oscillation method (below 1000 Hz).

2.8.1 **Ultrasonic Measurement**

Ultrasonic measurements are used to measure the travel time and the change of the waveforms' amplitude in the samples to obtain the acoustic parameters of the rock such as bulk modulus, shear modulus, and attenuation coefficient. This method works by placing transducers on opposite sides of a sample. One of the transducers works as the source and the other as the receiver. Due to the size of the specimen and the power of the vibration exciter, propagation time techniques are used for the MHz range, which is a high frequency.

(Wyllie et al.1958) conducted experiments of sandstone to find the factors which can affect the velocity of vibratory signals in porous media. However, Wyllie's formula can only be used when the effective pressure is high. (Birch 1960, 1961) used the travel time to obtain compressional velocities under 1 GPa confining pressure. He also gave numerical tables of velocity as a function of the direction of propagation, initial density, and pressure in the igneous rock. Due to the high confining pressure, the results are not suitable for seismic survey application. After Birch (1960,1961), numerous experiments have been done to study how seismic properties may be affected by factors such as pressure, temperature, saturation, fluid type, porosity, pore type, etc. (King, 1966; Toksöz *et al.*, 1976; Raymer *et al.*, 1980; Wang, 1988; Dvorkin and Nur, 1993; Dvorkin *et al.*, 1995; Xu and White, 1995). Ultrasonic experiments with CT, NMR and analogous

mineralogy using sedimentary rock help us experimentally correlate velocities by using parameters such as clay content and cementation (Murphy, 1984; Xu and White, 1995). Results show that even minor cracks will decrease the velocity significantly. Cadoret et al. (1995) used x-ray techniques to show that fluid in rock pores display a patchy distribution and only approach a uniform distribution when the degree of saturation is high. Cadoret also concluded that the velocity of drainage is higher than the velocity of injection. Lebedev (Lebedev *et al.*, 2009) observed that the Gassmann-Wood formula is fit for low permeability saturated sandstone. Lei (Lei and Xue 2009) injected CO_2 into saturated rock. They found that fluid flow induced by a wave can explain why velocity and attenuation change with saturation.

Ultrasonic measurements in the past couple of decades are of particular interest because of data obtained from the field for time-lapse seismic monitoring. Time-lapse seismic methods were first reported by Winkler and Nur (1982). They discussed the potential for application to monitoring thermal recovery projects based on the mechanics of seismic attenuation. Time-lapse seismic monitoring and reservoir simulations were carried out in Alberta, Canada (Eastwood et al., 1994), helping petroleum engineers to track the volume and shape of the reservoir affected by thermal in situ processes. The application of time-lapse monitoring helped determine the need for and location of infill wells and provided information for modifying operational parameters (e.g., steam cycle length, steam volumes and rates, and multiwell steaming patterns). Isaac (1996) also researched seismic methods for heavy oil reservoir monitoring and demonstrated the use of the time-lapse seismic techniques for providing refined input into reservoir simulation models. Jenkins et al., (1997) showed that time-lapse seismic data could enhance injector profile management even within heterogeneous sandstone reservoirs. Sun (1999) developed new reservoir characterization and monitoring technologies by using time-lapse seismic data and analysis methods. Zou et al., (2006) presented a practical procedure for using reservoir simulation results to generate synthetic time-lapse seismic responses. Kato et al. (2008) studied the change of elastic properties in a bitumen reservoir during steam injection. Hiebert et al., (2014) ran several SADG simulations to determine how steam or gas chamber volume, stress change volume or temperature change volume would impact the time-lapse seismic surveys.

Efforts in time-lapse seismic modelling on thermal projects generally try to separate the impact of stress change and fluid saturation. However, the seismic surveys collected in the field are conducted at seismic frequencies (Hz range) while the laboratory data used to calibrate the data are obtained in MHz frequency range. As per the discussion above, the velocity dispersion will be found in these frequency ranges. If these dispersion impacts are not included in the modelling, then the subsequent results may be wrong. This research is aimed to challenge how we can measure dynamic properties under shear while the material undergoes shear-induced volume changes, with a focus on capturing how Young's modulus varies over a range of seismic frequencies.

2.8.2 **Resonance Bar Techniques**

Resonance bar techniques are based on the principle of standing waves. Sinusoidal vibration is applied at its resonant frequency to make the rock deform. The prepared specimen is clamped at its midpoint in an aluminum frame and electromagnets driven by a sinusoidal voltage designed to drive a particular resonance mode are mounted at each end of the frame (Mccann, 2009). The P-wave and the S-wave could be obtained from:

$$V_P^2 = V_P^2 \frac{4V_P^2 - V_E^2}{3V_P^2 - V_E^2} \qquad 2\text{-}22$$

where V_E is extensional velocity.

There are two methods of vibration; the first one makes the longitude change (sensitive to Young's modulus) and the other makes bending and torsional deformation (sensitive to the shear modulus). Velocities are 1%–7% higher in sonic logging than in lab tests (a much larger dispersion than in heavy oil sands). This technique is used to measure the relationship between frequency and attenuation. Winkler and Nur (Winkler and Nur, 1982) studied influencing factors, such as saturation, pressure, pore pressure and strain amplitude, from 500 Hz to 9000 Hz. The results showed that partial saturation is a reason for velocity attenuation in the reservoir. In addition, Murphy (Murphy, 1984) worked on high porosity sandstone to find the peak of attenuation from 300 Hz to 14 kHz. Yin (Yin et al., 1992) found that the attenuation relied on the saturation, the saturated mode, and the fluid boundary condition by using a different way of injection and

discharge in Berea sandstone. Vogelaar (Vogelaar, 2009) obtained the low-frequency data from two-phase media. He compared the result with the Gassmann formula and got a reasonable result. However, to measure the seismic frequency, the sample should be durable and isotropic, and the length of the sample needed is 0.2-1 m, depending on the testing frequencies and subsequently makes, it difficult to use this technique in oil fields, especially for loose sand and shale.

2.8.3 **Forced Oscillation Method**

Forced oscillation techniques are relaxation processes. These are straightforward methods for acquiring core acoustic properties by recording the forced deformation. These techniques can show accurate and continuous velocity and attenuation in a lower frequency. The forced oscillation method works by applying sinusoidal stress to material and measuring the resulting strain. The phase delay between the stress and the strain is then calculated (Spencer, 1981; Batzle et al., 2006). The axial strain ε_{33} under the boundary condition is given by,

$$\varepsilon_{33} = \frac{\partial u}{\partial x} = F cos\left(\sqrt{\frac{\rho}{E}} \times \omega x\right) sin(\omega x) \qquad 2\text{-}23$$

where u is displacement, x is location, ω is frequency, ρ is density, E is Young's modulus, and F is an elastic constant defined by the geometry.

From the horizontal strain we can extract Poisson's ratio υ, where the superscript rx refers to the rock value:

$$\upsilon^{rx} = -\frac{\varepsilon_{11}^{rx}}{\varepsilon_{33}^{rx}} \qquad 2\text{-}24$$

If aluminum is used as a standard sample, the Young's modulus of the rock is derived from:

$$E^{rx} = E^{al}\frac{\varepsilon_{33}^{al}}{\varepsilon_{33}^{rx}} \qquad 2\text{-}25$$

Then, other elastic properties for an isotropic homogeneous sample can be calculated by equations 2- 13 and 2- 14.

The principle of forced oscillation techniques is simple, but it is experimentally difficult as the magnitudes of measured values of attenuation are relatively low (0.01– 0.1) and the amplitudes of strain applied to the rock samples are particularly low, of the order of 10^{-6} (i.e., similar orders of magnitude to seismic waves) (Winkler et al., 1979; Spencer, 1981; Paffenholz and Burkhardt, 1989).

Spencer (1981) developed an instrument with frequencies ranging from 4 Hz to 400 Hz and a strain of 10^{-7}. He worked on saturated sandstone and limestone to get the velocity and attenuation. Cole-Cole mechanics can explain why the attenuation and velocity consist of the frequency. The results explain pore fluids lowering the free energy of the surface of rock-forming minerals. An electromechanical shaker induced the sinusoidal force and a capacitive was used as a displacement transducer. An in-line piezoelectric transducer measures the applied stress. The confining pressure can be up to 70 MPa with high-pressure nitrogen gas. This instrument was updated to measure Poisson's ratio by adding radial transducers (Spencer et al., 1994; Spencer and Shine, 2016). Paffenholz and Burkhardt (1989), designed a device to measure the shear modulus G and the shear attenuation $1/Q_S$ by using torsional and volumetric mode experiments. The sample is glued to the reference cylinder (aluminum). A pre-stress of 1.5 MPa, some 30 times greater than the harmonic applied stress, is applied in the axial direction to ensure proper contact of surfaces. An inductive displacement transducer is used for displacement measurement and two piezoceramic displacement transducers are used to oscillate the sample. The frequency range is 0.03-100 Hz. No confining pressure can be applied to this system.

Batzle et al., (2006) measured sandstone and carbonates from 1 Hz to 2 kHz. A shaker was used for force oscillation and several pairs of strain gauges were used for strain measurements (around 10^{-7}). Strain gauges are glued to the sample with impermeable polyimide film that serves as the jacket for the samples. High-pressure nitrogen gas is used for hydrostatic confining pressure. Results from their testing showed that fluid flow had a significant influence on velocity and attenuation and that dispersion was large when the fluid is in the seismic range. They also improved the experimental system by integrating a servo-controlled pressure intensifier and decreasing the volume of the downstream reservoir. Adam *et al.*, (2009) worked on carbonates from 10 Hz to 1000 Hz. They concluded that the attenuation increases largely when we use saline to replace the

hydrocarbon. Madonna and Tisato (2013) also developed a testing system for measurements at seismic frequency, but it only works under normal pressure and temperature. They developed a Seismic Wave Attenuation Module (SWAM) laboratory apparatus based on the strain-stress technique with longitudinal forced oscillations and an operating frequency range of 0.01 to 100 Hz. The apparatus can measure the complex Young's moduli of rock samples at confining and uniaxial pressures as high as 50 MPa. It uses a piezoelectric actuator for force generation and linear variable differential transformers (LVDTs) for displacement measurements on both the sample and the aluminum standard. Tisato *et al.*, (2012; 2014; 2016) collected a large amount of data with the broadband attenuation vessel (BBAV) and other laboratory devices to analyze the physics of wave-induced fluid flow in Berea Sandstone. They developed a new sub resonance apparatus, paired with a micro-CT system, which can be used to further investigate the influence of fluid distribution and microstructural features on attenuation. The frequency range is 0.01-100 Hz with strains around 10^{-6}. The force generator is a multilayer piezo stack and the applied stress was measured by a load cell. A strain-gauge cantilever measured the displacement under confining pressures up to 25 MPa, with oil as the confining medium.

Mikhaltsevitch et al., (2014a) developed a seismic frequency (SF) laboratory apparatus based on the strain-stress technique with the longitudinal type of forced oscillations and an operating frequency range of 0.1 to 400 Hz. The SF system can measure the complex Young's moduli of rock samples at confining and uniaxial pressures as high as 70 MPa and at pore pressures as high as 20 MPa. The sample is cylindrical in shape: 70 mm in length and 38mm in diameter. Axial and radial strain gauges are glued to the sample for displacement measurements. The device employs a piezoelectric actuator for the sinusoidal stress, whereas an aluminum standard acts as the stress sensor. They measure elastic and anelastic parameters of dry and glycerol-saturated Berea sandstone. The apparatus operates at confining pressures from 0 to 70 MPa. The elastic moduli and extensional attenuation of dry and glycerol-saturated sandstone were measured at a differential pressure of 10 MPa at both 23 °C and 31 °C. Peaks of attenuation in the glycerol-saturated sample were found at frequencies of ~0.6 Hz (23°C) and ~1.5 Hz (31°C).

Szewczyk et al., (2016) introduced a new laboratory apparatus that could measure seismic dispersion under deviatoric stress conditions. The frequency range is 0.1 Hz–200 Hz. A

piezoelectric force sensor is used to measure force. Stress at seismic frequencies was generated by a piezoelectric actuator. Strain gauges attached to the sample were for displacement measurement. Table 2-1 (Subramaniyan et al., 2014) lists laboratory apparatuses that measure attenuation/dispersion in reservoirs based on the above discussions.

Table 2-1 Comparison of forced oscillation setups.

	Sample Length × diameter	Displacement Sensor	Frequency Range (Hz)	Confining Pressure (MPa)	Deviatoric Stess	Temperature (□)
Spencer (1981)	140×38.1	Capacitive Transducer	4-400	70 (Nitrogen)	No	No
Paffenholz and Burkhardt (1989)	150×50	Inductive Transducer	0.03-300	No	No	No
Batzle *et al.* (2006)	45×30	Strain Gauges	1-2000	10 (Nitrogen)	No	No
Takei et al. (2011)	15×32.5	Laser Displacement Sensor	0.001-10	No	No	40
Tisato and Madonna (2012)	250×76	Strain Gauges	0.01-100	25(Oil)	No	No
Madonna and Tisato (2013)	60×25.4	Linear Varialbe Differential	0.01-100	50 (Argon)	No	No
Mikhaltsevitch et al. (2014)	70×38	Strain Gauges	0.1-400	70 (Oil)	No	No
Szewczyk et al. (2016)	50.8×25.4	Strain Gauges	1-155	5-20 (Oil)	Yes	No

2.9 Summary

Forced oscillation setups are composed of three main components: (i) force generator, (ii) displacement sensor to record the sample strain response, and (iii) force sensor to estimate the applied stress (Subramaniyan *et al.*, 2014).

1. Force generator. The force generator can be an electromechanical shaker (Spencer, 1981) or a stack of piezoelectric elements (piezoelectric) (Paffenholz and Burkhardt, 1989). The piezoelectric actuator is widely used for generating force at seismic frequencies. Piezoelectric actuators are transducers that convert electrical energy into mechanical stress based on a piezoelectric effect. Piezoelectric actuators have lower power consumption and better lateral stability to prevent tilting of the sample (Liu and Peselnick, 1983; Paffenholz and Burkhardt, 1989). The piezoelectric actuator is sensitive to a small variation of voltage,

resulting in high-resolution oscillation at seismic frequencies. However, there are two disadvantages to the piezoelectric actuator. First, the piezoelectric actuator can only induce small stress which requires that the specimens are smaller. The second disadvantage of the piezoelectric actuator is that it is unable to work under high loading which means testing cannot be conducted under shear deformation to investigate how stress could affect the dynamic properties at seismic frequencies.

2. Displacement sensor. So far, the displacement sensors used in forced oscillation apparatuses include strain gauges mounted on the sample (Batzle et al., 2006) or cantilever (Tisato and Madonna, 2012), capacitive (Spencer, 1981), and inductive transducers (Paffenholz and Burkhardt, 1989) (Tisato and Quintal, 2013). Transducers utilizing new technologies such as fiber optics, magnetostrictive, or Hall Effect might improve the measurement quality. Linear variable differential transformers (LVDT) and strain gauges are widely used for dynamic properties measurement.

   LVDTs are comprised of a cylindrical array of primary and secondary windings with a detached cylindrical core that passes through a hollow center. Highly sensitive, LVDTs can be used to measure axial displacement over the length of a core sample instead of just local deformation and are even suitable for samples exhibiting a high degree of heterogeneity such as carbonates. An LVDT is only applied for axial displacement measurements due to the sensitivity.

   In addition to LVDTs, strain gauges are used during dynamic experiments as a measurement for the axial as well as the radial deformation. The strain gauge has a rosette with two independent resistors measuring the deformation in a perpendicular direction. Each of the two circuits has two soldering tabs where wires are connected. These components are attached to foil glued onto the rock (Kobayashi, 2015). The fundamental formula for the resistance of a wire with uniform cross-section, A, and resistivity, ρ, can be expressed as:

$$R = \rho \frac{L}{A} \quad \text{2-26}$$

The change in resistance is transformed to deformation by a linear relationship. The linear relationship between the changes in resistance is the gauge factor (GF):

$$GF = \frac{\frac{dR}{R}}{\varepsilon} = 1 + 2\upsilon + \frac{\frac{d\rho}{\rho}}{\varepsilon} \quad \text{2-27}$$

For this equation, we could conclude that GF directly represents the Poisson effect, i.e., the tendency in an elastic material to contract laterally in response to axial stretching.

Strain gauges are glued directly to the specimens and sealed by impermeable polyimide film, making it so fluid information cannot be obtained and causing errors from boundary effects. Furthermore, during testing the sample will dilate or expand with shear deformation, also resulting in errors. Lastly, strain gauges are temperature-sensitive, so fluctuations in ambient and operating temperatures will have severe effects on the measurement circuitry, making the strain gauge unsuitable for high-temperature testing.

3. Force sensor. The applied force can be measured in two ways: (i) with a pre-calibrated load cell/transducer and (ii) by employing a low attenuating material to serve as a reference. In the latter case, the displacement of the standard is measured with a strain sensor; this calibration, which allows the conversion of voltage to displacement, must be defined prior to the measurements. As the standard is in phase with the applied stress, values for the modulus and the corresponding attenuation (e.g., E and $1/Q_E$) can be obtained through the comparison of the displacement signals obtained from the sample and the standard (Madonna and Tisato, 2013).

2.10 **Literature Overview**

As indicated previously, laboratory results are needed to verify the existing theoretical models. Most of the tests are conducted at ultrasonic frequencies due to numerous engineering challenges. There is no calibration workflow before inputting data into time-lapse seismic modelling allowing

separation of the impact of stress change or fluid saturation. As very little experimental research has been conducted on rock dynamic geomechanical properties at seismic frequencies, it is also important to acquire further experimental observations of velocity dispersion under different fluid saturations, elevated temperatures, and confining pressures to have a sufficient understanding of the dynamic geomechanical properties during shear deformation.

This study develops and implements a novel triaxial testing system based on a servo-hydraulic load frame to investigate seismic dynamic properties of a specimen under shear deformation. A dual-load cell system could obtain static and dynamic loading at the same time with a force up to 100 kN. To conduct high-temperature testing, a pair of laser displacement sensors are used instead of strain gauges and LVDTs. Reconstituted dense sand from Fort McMurray will be used for my research. It is rare to measure this kind of material under shear -previous tests were typically done isotropically and under larger confining pressures (100 MPa) to try and close all the cracks. Complete details of the novel system will be discussed in the following chapter.

3 EQUIPMENT, INSTRUMENTS, AND CALIBRATIONS

The principle of a seismic frequency apparatus is to apply an oscillating force (stress) and measure the resulting displacement (strain). By calculating the incremental stress and resulting strain, moduli at seismic frequencies can be determined. The time lag between stress and strain is the attenuation of the specimen. Many researchers have proven that the stress-strain method is the only way to measure geomechanical properties at seismic frequencies (Batzle et al., 2006; Subramaniyan et al., 2014), and although the principle is straightforward, many hurdles exist.

The forced oscillation system consists of three essential components:

1. An actuator that can generate uniform force to the specimen in a sine wave pattern below a strain of 10^{-6};
2. Force sensor that can measure the applied force;
3. A displacement sensor that can monitor the nm scale displacement of the sample.

The following sections will introduce the MTS system with trials and tribulations to illustrate the capacity and limitations of the whole system. Also, several sensors with calibration results are introduced to meet the testing standards.

3.1 MTS system

The MTS system (370.50) is a computer-controlled load frame delivering up to 250KN of axial load (Figure 3.1). Given the sophisticated operation of the MTS system, it is important to understand the technical specifications of each hardware component and the operation of the software to control the system. The MTS system contains hydraulic power units (HPU), which are (pumps) that provide fluid flow for the actuator. Temperature and oil level shut-off switches protect the pump. A hydraulic service manifold (HSM) is next to the HPU. With electrically operated valves, the HSM makes hydraulic oil available to the servo valve. The actuator, which is connected to the HSM, applies movement or force to the test specimen and is controlled by the internal MTS software. The actuator for the MTS was designed for a specific band of frequency (up to a maximum of 80 Hz) to allow for forced oscillation experiments to be conducted.

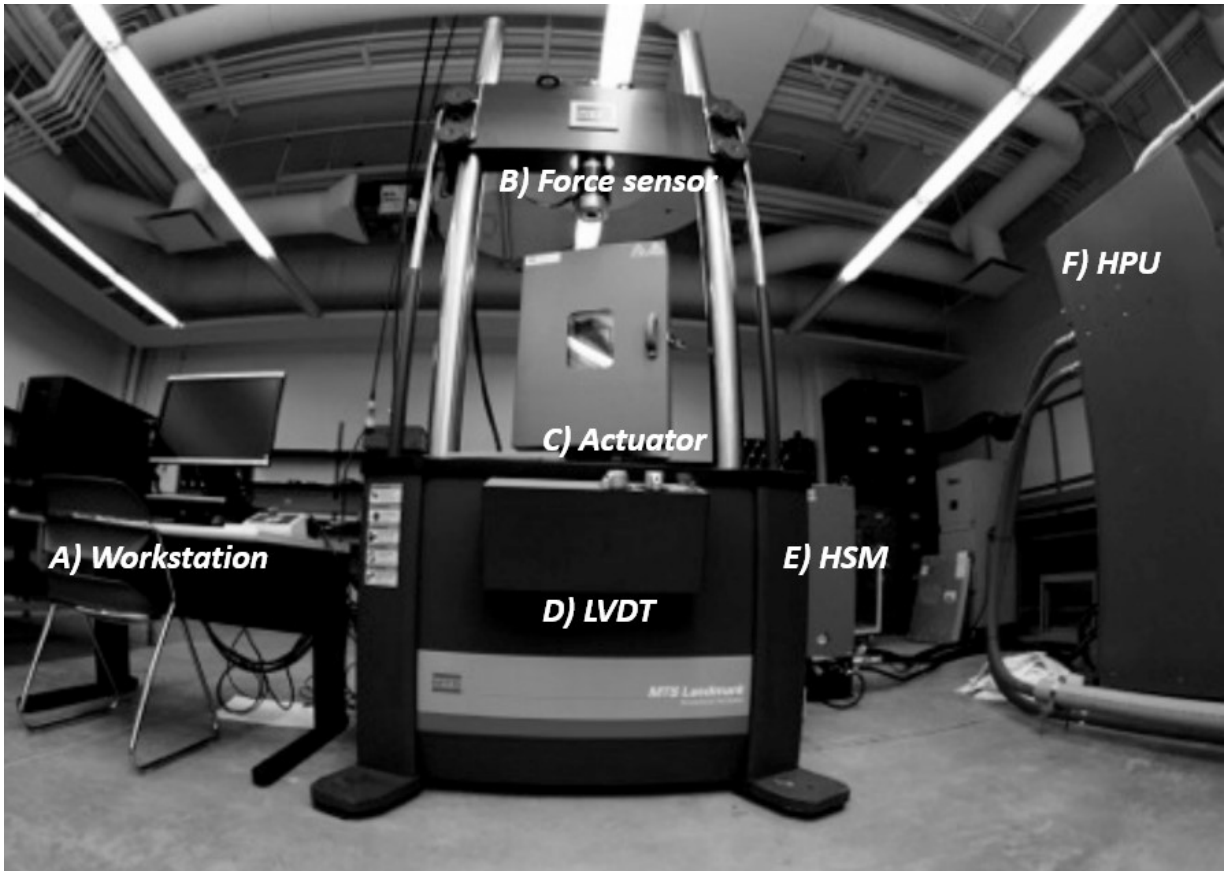

Figure 3-1 Overview of the computer-controlled load frame MTS system (A) workstation, (B) force sensor for measuring the applied force, (C) actuator for generating the sinusoidal force from 0.1Hz to 20Hz, (D linear variable displacement transducer (LVDT) to measure the moving displacement of the actuator), (E) hydraulic service manifold (HSM) and (F) hydraulic power unit (HPU).

This system has been designed to allow the actuator to move from 0.01 Hz to 80 Hz. An LVDT (Linear variable differential transformer) with a resolution of $\pm$ 1 μm positioned below the actuator is used to measure the displacement of the actuator. A 250 kN $\pm$ 0.002 kN capacity load cell is positioned above the actuator. The force transducer sends out a voltage proportional to the amount of force being applied and is used to measure the loading applied to the samples.

An integral MTS software control system is used to program the loading sequence on a sample. With software that can maximize electrical efficiency and minimize water consumption, and options for remote monitoring of pressure, temperature, and fluid level, the HPUs help reduce facility energy costs. MTS Hydraulic Service Manifolds (HSMs) provide independent pressure

regulation for the precise control, isolation and distribution of hydraulic fluid to test stations. Two flow rate controllers are used to operate the HSMs. High flow rates deliver high capacity at high speeds for the higher frequency test ranges while the low flow rate is used for system stability at the lower frequency test ranges.

3.1.1 **Tuning system**

Prior to forced oscillation testing, it is critical that the MTS system is "tuned". Tuning affects the response and stability of the servo control loop, and proper tuning improves the performance of the system, eliminating the stiffness effect from the specimen. Tuning must first be conducted each test with a different sample because the MTS system has two control modes (force and displacement) and each control mode uses a different sensor feedback signal for servo loop control.

Each control mode must be tuned via PID tuning provided by the MTS system. A proportional–integral–derivative controller (PID controller or three-term controller) is a control loop mechanism employing feedback that is widely used in industrial control systems and a variety of other applications requiring continuously modulated control. The speed of the actuator response is adjusted with a proportional gain switch. As the proportional gain increases, the actuator response improves, and the feedback signal matches the input commands more closely (Figure 3-2). Too much proportional gain causes the system to become unstable while too little proportional gain can cause the system to lag. Therefore, a proper proportional tuning gain should be identified so that its servo loop responds accurately to the command signal. Even for the same specimen, the signal is different at different frequencies. It is, therefore, best to adjust PID at different frequencies to improve the stability of the MTS system.

3.1.2 Tests with Cement Samples

To study the operation and performance of the MTS system, four unconfined compression (UCS) tests were conducted with the MTS system. No additional comments will be added on to the cement samples since the tests were conducted for the better understanding of the system operation and were treated as dummy samples. Figure 3-3 shows the stress-strain curves of the four tested samples and Table 3-1 is the summary of the test results. From the UCS tests, peak axial, undrained

cohesion, and the Young's modulus were determined. Cyclic tests (at different frequencies) based on these parameters were conducted.

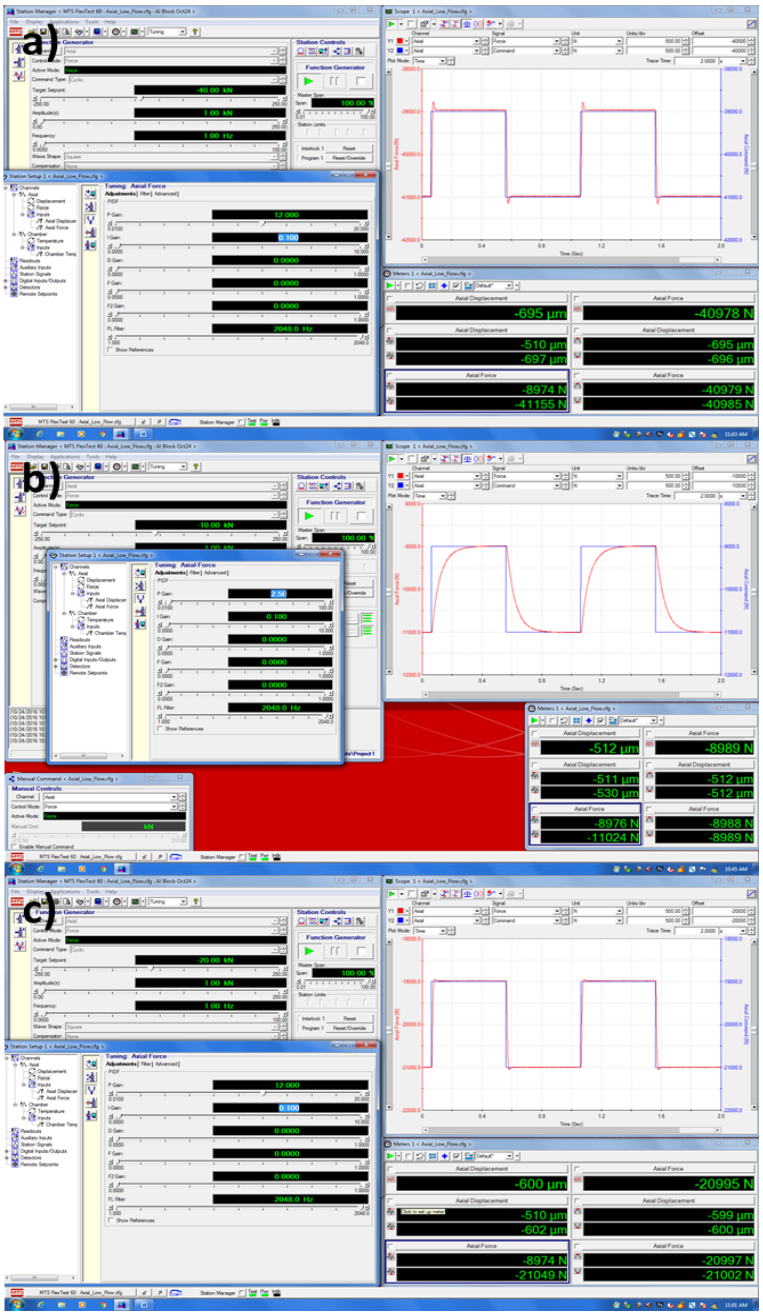

Figure 3-2 Screenshot of the tuning procedure where the red line indicates the feedback signal and the blue line indicates the command signal. a) proportional gain is too high; b) proportional gain is not enough, and c) proportional gain is proper.

Table 3-1 Summary of the four cement samples UCS test results.

Test No.	Peak Axial Stress (kPa)	Undrained Cohesion (kPa)	Modulus of Elasticity (MPa)	Axial Strain at Failure (%)
C1	2916	1458	359	1.46
C2	2482	1241	448	0.86
S7	2041	1020	319	0.77
S8	2460	1230	318	0.85

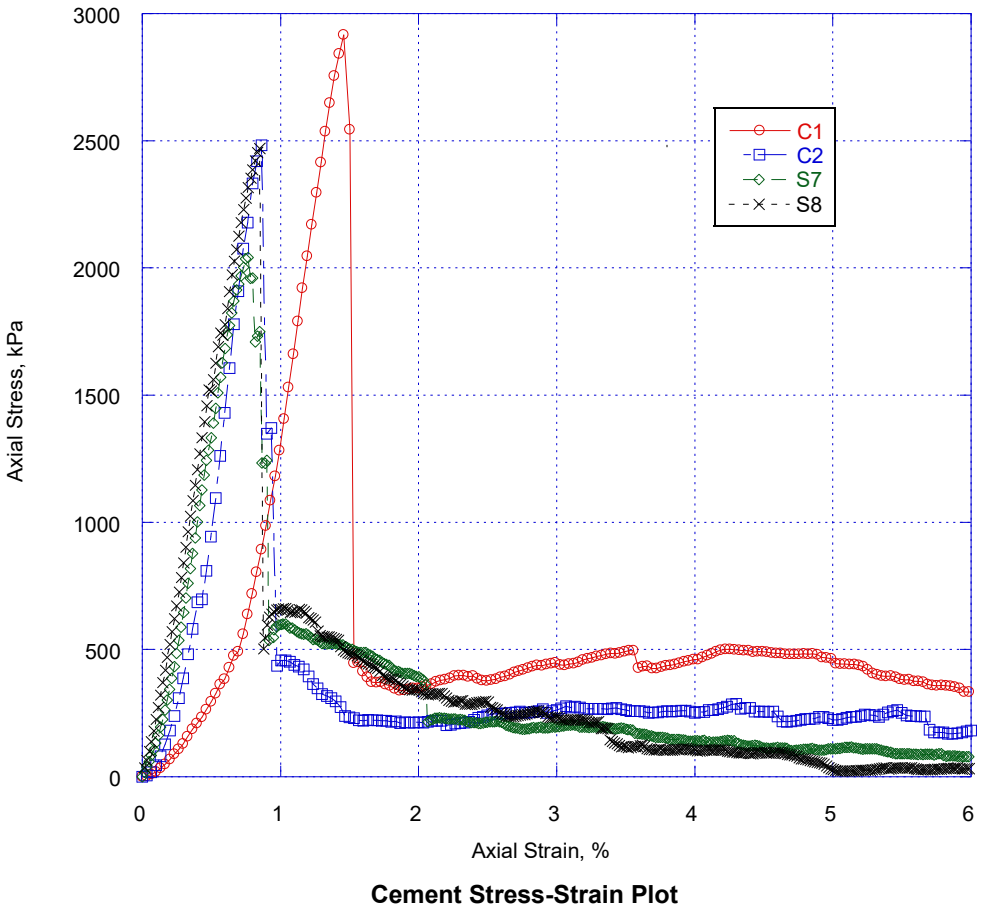

Figure 3-3 Stress-Strain curves from UCS tests on four cement samples.

Following the UCS tests, several cyclic tests are conducted. There are two modes for the MTS system: 1) force mode and 2) displacement mode. Force mode uses a strain gauge load cell to close

the loop. Displacement uses LVDTs to close the loop. The actuator can generate two wave shapes: 1) square curves and 2) sine curves.

First, three tests of the same amplitude were conducted at different frequencies (Figure 3-4). As expected, the force increased as frequency decreased. However, there was a notable displacement error that needed to be explained. At a higher frequency (10Hz), there is not enough time for the MTS system to obtain the expected amplitude. By decreasing the frequency to 1Hz, the amplitude is correct, indicating that displacement control mode is not accurate for small travel and high-frequency testing. Using the force control mode, the MTS works well at different frequencies and amplitudes.

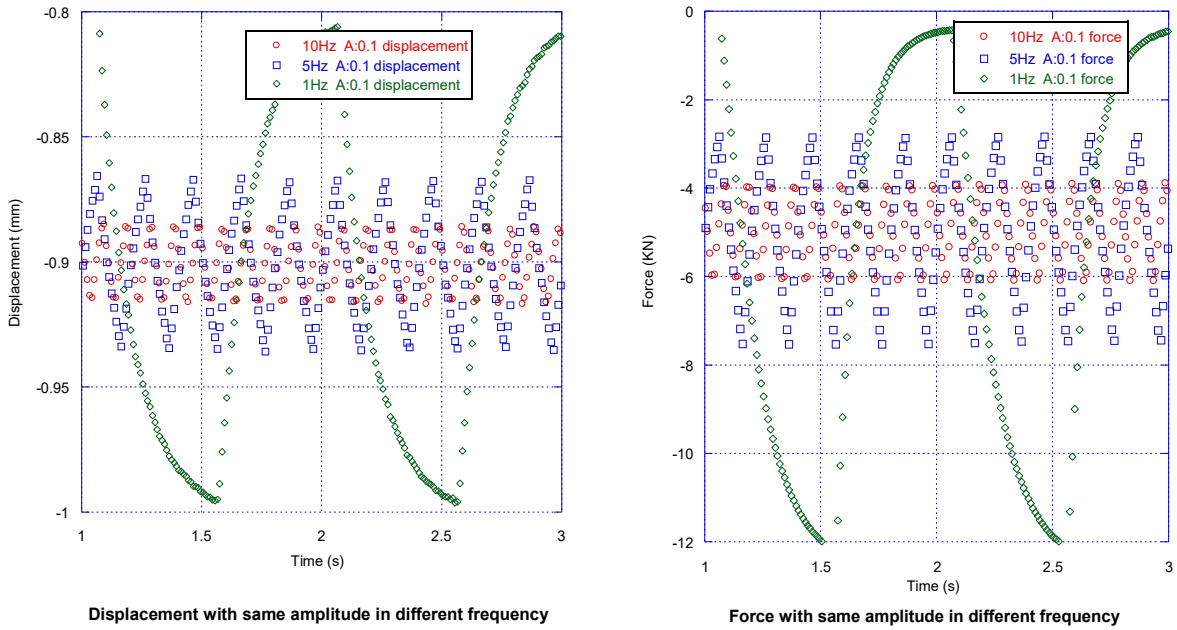

Figure 3-4 Tests with different frequencies as the same amplitude based on two control models.

Two tests of different amplitudes are then run at the same frequency (Figure 3-5). Displacement data sufficiently demonstrates that the MTS system will provide typical amplitude. It is also confirmed that Force control mode increases with tests at a larger amplitude, but the mid-point of force is different using displacement control mode. For an amplitude of 0.1mm, the midpoint is around -6KN. However, for an amplitude of 0.05mm, the mid-point is around -5KN. This is caused by the MTS feedback signal from the LVDT during displacement control mode. Since the LVDT is under the actuator, more loading needs to be added for larger displacement amplitudes. Attention

should therefore be paid if the amplitude is changed using displacement mode as loading will need to change. Otherwise, the MTS reading is stable in force control mode.

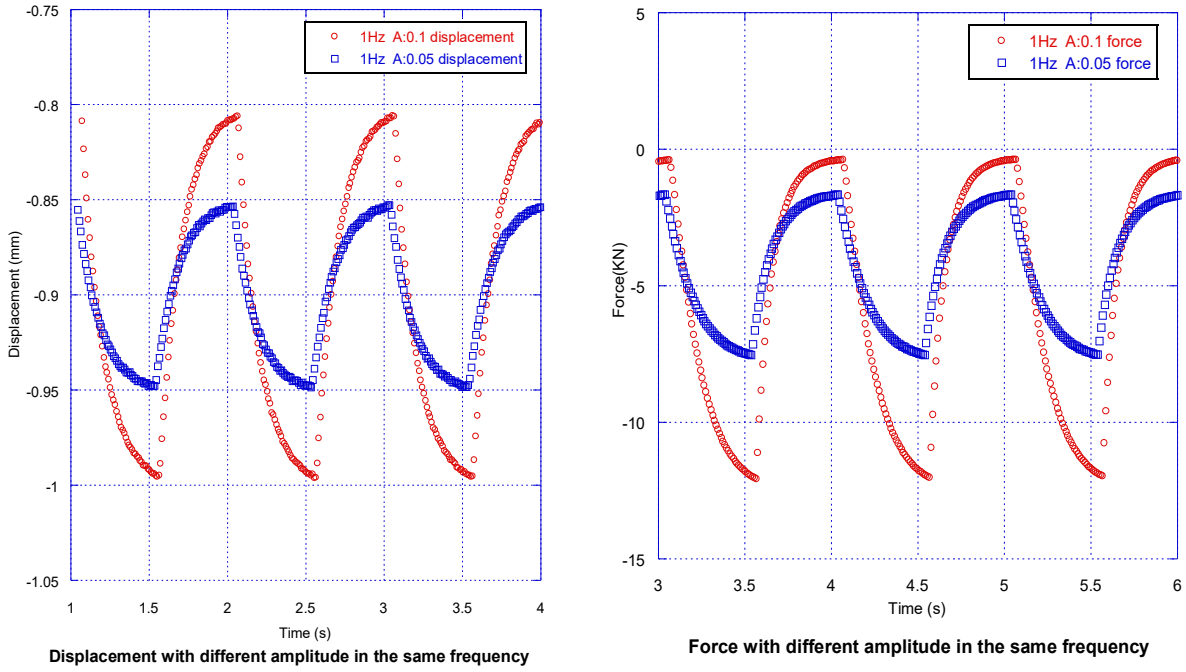

Figure 3-5 Tests with different amplitude as the same frequency based on two control models.

Next, two tests of the same amplitude are run with the same amplitude at different setpoints (Figure 3-6). The displacement is accurate regardless of the setpoint but changing to larger setpoint results in an increase of force.

Finally, two additional tests were run with modified amplitude shape curves (Figure 3-7) and it was concluded that the sin curve shape was more appropriate than the square curve shape.

3.1.3 Testing with Calibration Materials

Several tests are also conducted based on the previous section. From the tests, it was ascertained that the MTS performed well at greater force and lower frequency. The purpose of these tests is to check whether the instruments are capable of accurately measuring tests conducted under small strain levels and seismic frequencies. Aluminum (6.35 cm Diameter and 12.7 cm) has been used in these tests and calculations indicate that force should be 1745 N for 1 μm displacement and 3481 N for 2 μm displacement. These parameters are used for reference first.

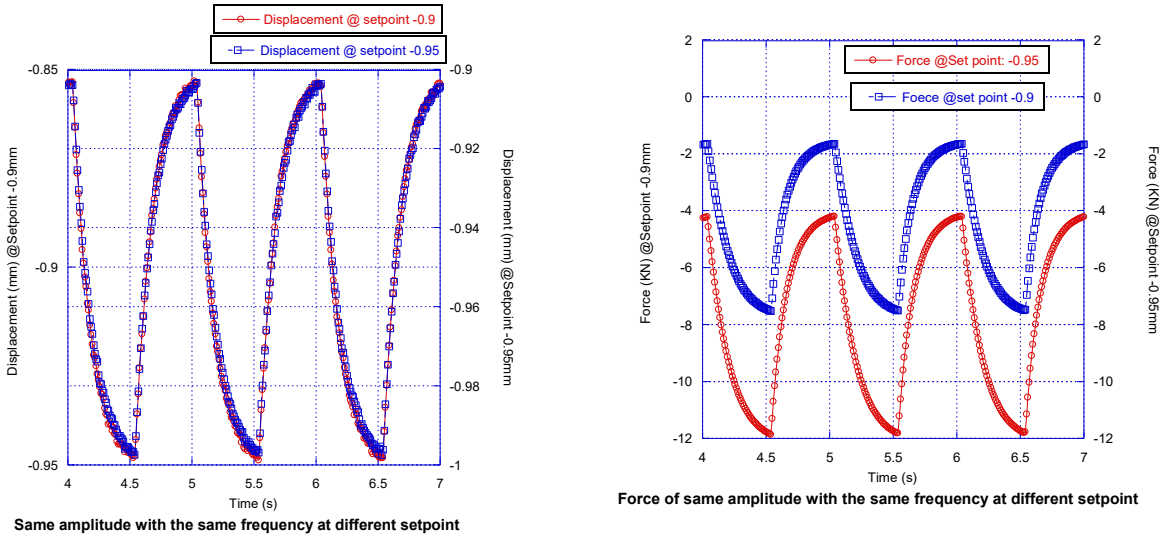

Figure 3-6 Tests using different setpoints with the same frequency and amplitude based on two control models.

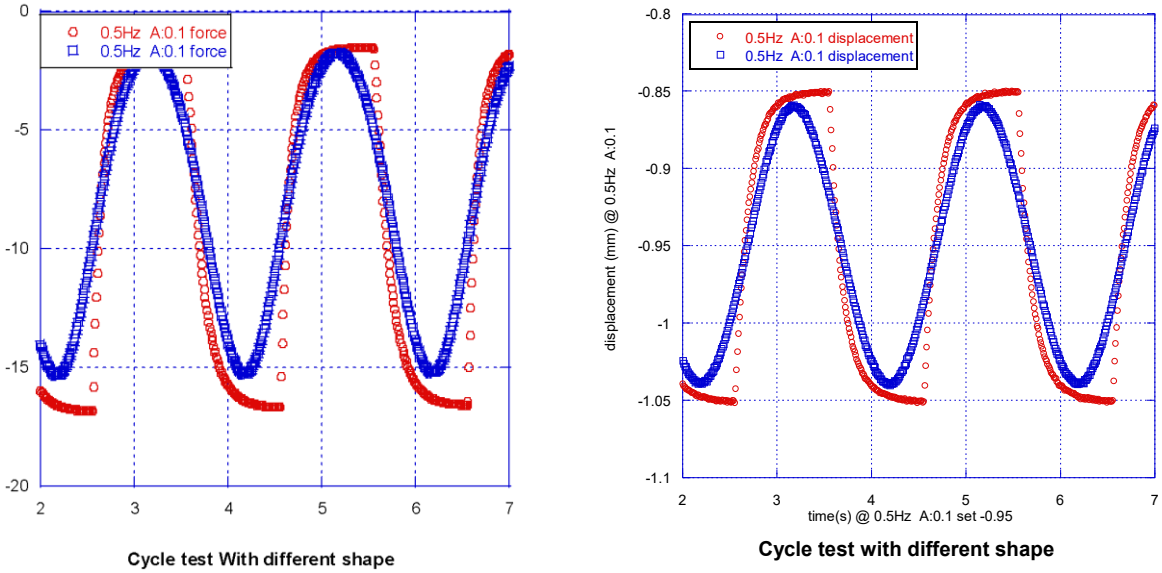

Figure 3-7 Tests with different shapes as the same frequency and amplitude based on two control models.

Tests are conducted using force mode with PVC compensation (Figure 3-8 and Figure 3-9). Performance is reliable and stable during the tests even at 80 Hz, but displacement is around 12 μm, which is much bigger than 1 μm. A Force of 3481 N is applied to the aluminum (Figure 3-10 and Figure 3-11) and displacement is 25 μm, indicating that the LVDT measurement is not tracking

the displacement of the aluminum specimen. Finally, displacement mode is used for another test. Compensation will not affect performance at small force and displacement.

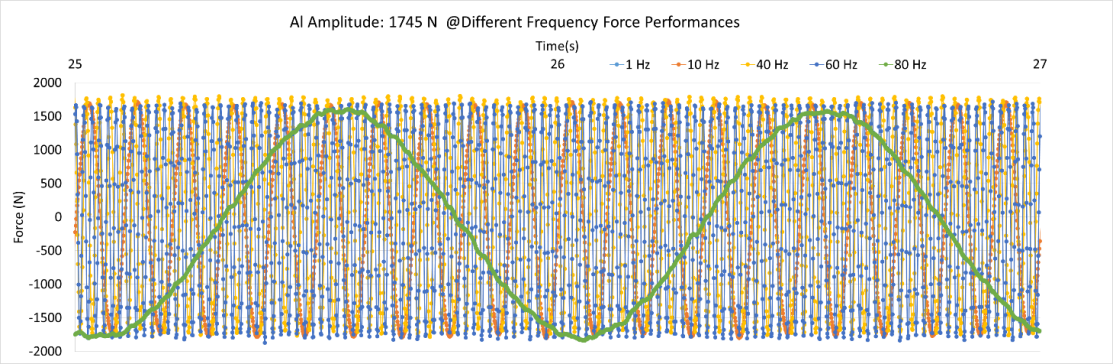

Figure 3-8 Dynamic testing based on the force control model (1745 N) at different frequencies with aluminum.

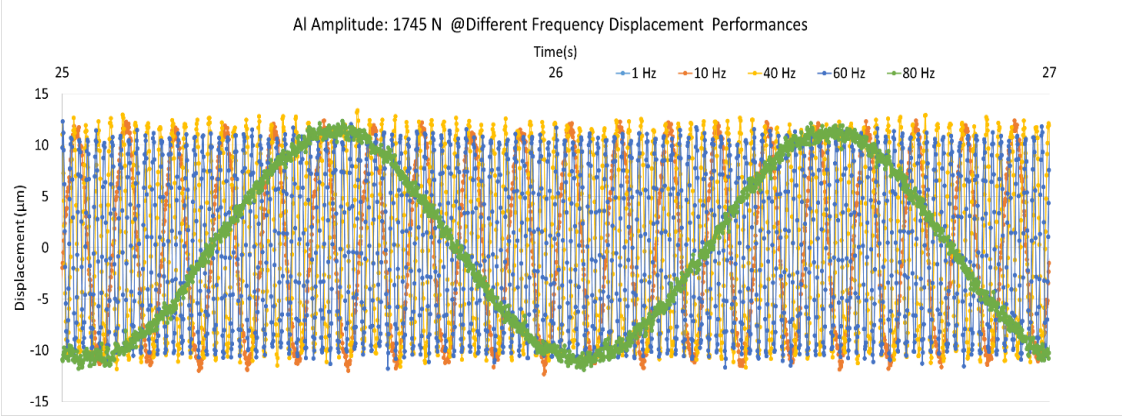

Figure 3-9 Dynamic testing based on the displacement control model (1 μm) at different frequencies with aluminum.

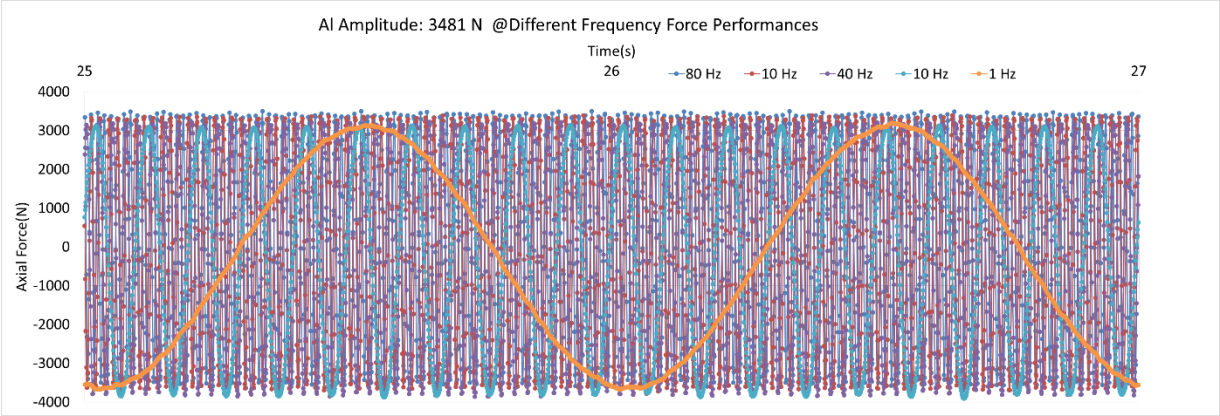

Figure 3-10 Dynamic testing based on the force control model (3481 N) at different frequencies with aluminum.

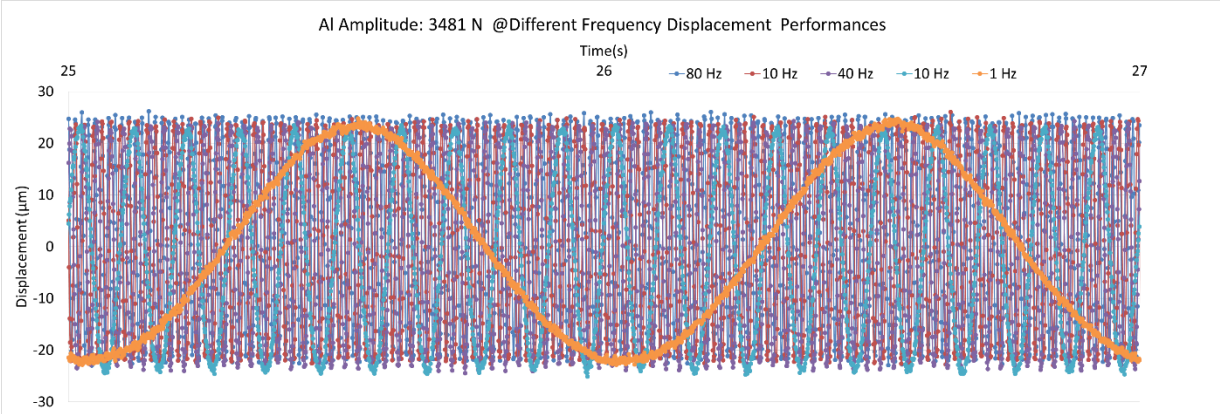

Figure 3-11 Dynamic testing based on the displacement control model (2 μm) at different frequencies with aluminum.

3.2 **Measurement sensors**

3.2.1 Displacement Sensors

From the testing results of cement and calibration materials, the limitation of LVDTs is only around 0.5 mm, but for seismic frequency measurements, the displacement will be in nm scale due to the 10^{-6} strain level. To measure displacement at dynamic frequency, displacement sensors should be used for this research. Strain gauges and LVDT are common displacement sensors and have been widely used in geotechnical laboratories for many years. An LVDT is an external

displacement sensor that can be used for anisotropic and unconsolidated specimens. LVDTs cannot measure on an nm scale with a high sampling rate. They also cannot measure samples with Young's modulus smaller, by one order of magnitude, than the modulus of the aluminum alloy. That means an LVDT can only measure at 7 GPa.

Many researchers are using strain gauges for testing. By using strain gauges, both vertical and horizontal displacement can be measured with no resonance effect, but silver soldering techniques must be used. It is impossible to use strain gauges for soft and anisotropic samples as the strain gauge is sensitive to temperature. During high-temperature testing, the sensitivity of the strain gauge decreases.

The latest technology is a vibrometer. Laser Vibrometer systems work well under both temperature and oil confined conditions. The velocity resolution of the instrument is 0.02 μm/ second, which changes to 0.1 μm/ second if the surface is rough. The frequency is low compared to what is typically measured with a vibrometer. Sub-nanometer displacement resolution with the measurement as low as 0.1 Hz can be found, but this could prove to be a challenging measurement for both low displacement and low frequency, through a liquid and on a non-reflective surface, as measuring at least 50 Hz is recommended for a Laser Vibrometer.

3.2.2 Displacement Sensor Installation

Laser displacement measurement is determined to be the best instrument. For temperatures at 200-300°C, it will require a special enclosure that has glass for the laser to shoot through, which suppliers could design. The LK unit comes as a set that includes an amplifier, cable, and sensor head. Information is digitally translated internally so as not to lose the signal. The resolution of the laser displacement is up to 2 nm with a maximum 316 kHz sampling rate.

The principle of the laser displacement sensor (Figure 3-12) is that a laser beam emitted from the semiconductor laser is applied to a target. The light reflected from the target is collected by the receiver lens and focused on the light-receiving element. To have high sensitivity, the measurement range needs to be controlled within 8 mm.

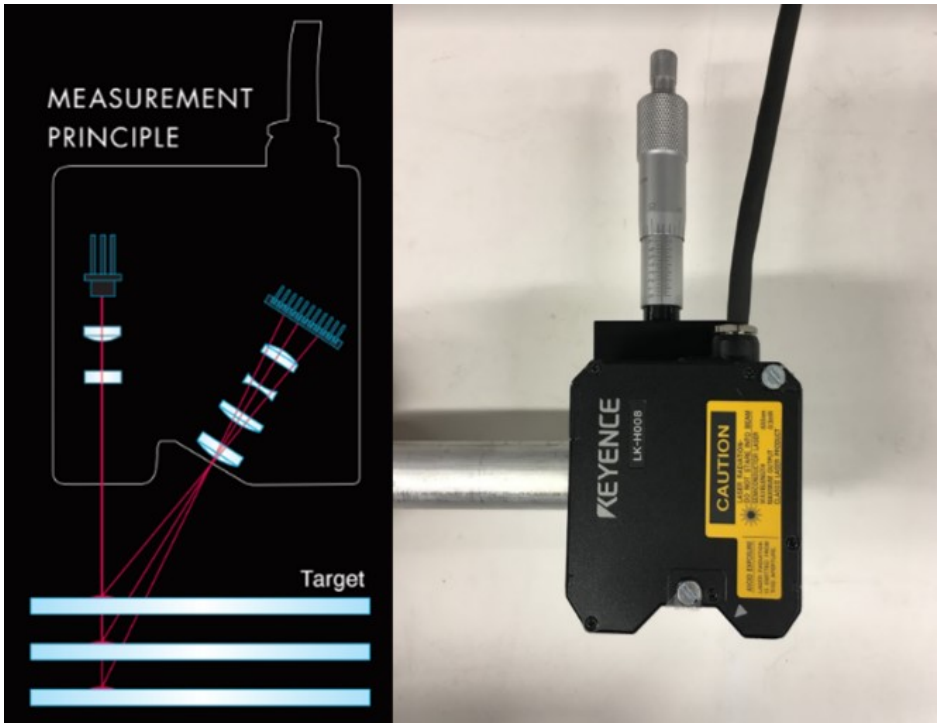

Figure 3-12 Principle of the laser displacement sensor.

Acrylic is used for all calibration tests with the laser sensors. During the testing, several issues needed to be resolved, beginning with determining where the laser sensors should sit. A pair of laser displacement sensors are placed at the bottom of the acrylic, but the result is not the same as the literature. The two laser displacement sensors are separated. One is put under the acrylic and the other is set on the top of the specimen. The Young's modulus obtained is the same as the result as the reference. The reading of the top laser displacement sensor is only around 0.3 μm, which is too sensitive for other displacement sensors, so an adjustable frame is designed for the pair of laser displacement sensors. The purpose of the adjustable frame is to provide a mount that allows the unit to obtain the highest accuracy possible. Longer extensions/bars will induce vibrations which will subsequently create noise. For the mount to be stable, a one-piece bracket made of steel or thick aluminum is required, and to eliminate the vibrations in the extension bars, several sandbags are put on the frame (Figure 3-13). The performance of the laser displacement sensors is improved significantly using this frame.

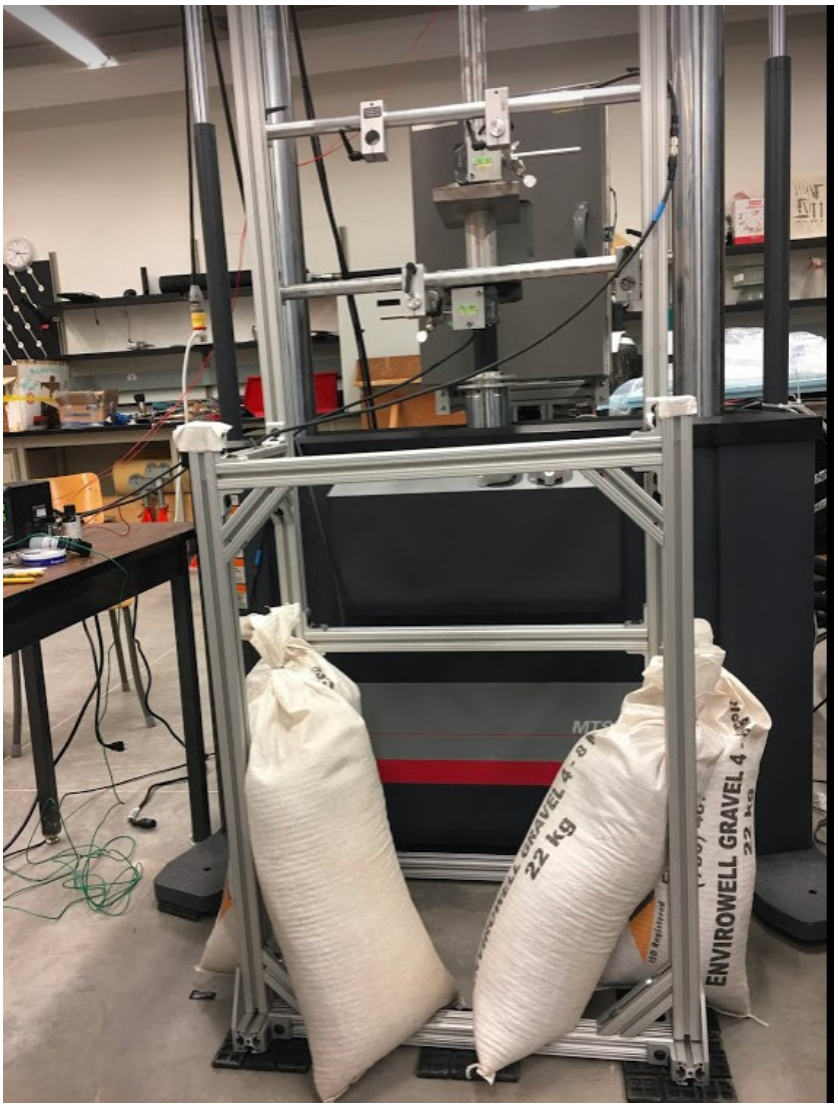

Figure 3-13 An overview of the mounting frame with sandbags.

Because the center range of the laser displacement sensor is at 8 mm with a +/-1mm area, fine adjustment is required to level and focus the pair of laser displacement sensors. A horizontal/vertical frame is ideal, but as any angle induced will result in a scaled reading, the adjustability of the mounting frame proves to be both good and bad. It is good in the sense it can be moved and changed to any angle, but this testing demands the laser be as perpendicular to the surface as possible. Generally, for these precise applications, a dedicated vertical mount with a scale for making fine adjustments would be preferred. The extension bar of the frame provides only rough adjustments. The laser displacement sensors will lose their signal if the specimen is softened or consolidated during the testing. The fine adjustment measurement device (Figure 3-

14) provides a 20 mm travel range with 0.5 mm sensitivity. Level set kits are used for monitoring the horizontal and vertical position before and during the testing to make sure no angle is induced.

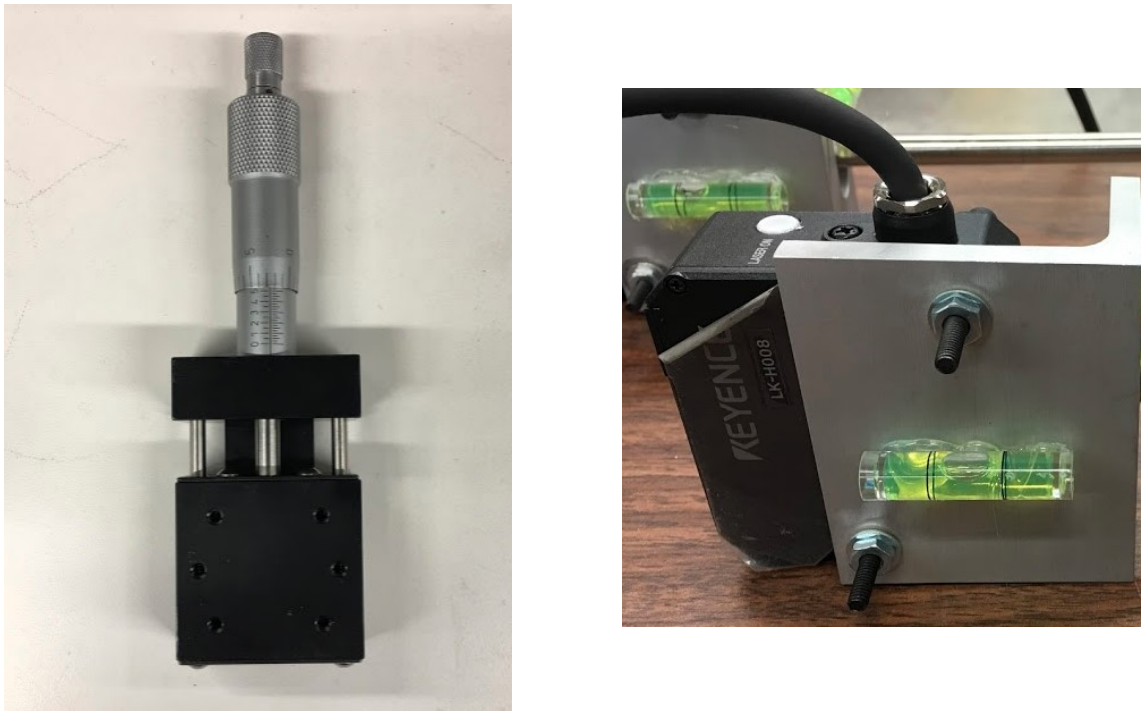

Figure 3-14 Fine adjustment measurement device with the level set kit.

Third, the setting is important to obtain a reasonable result. In the laser displacement sensor setting section, both the moving average and sampling rate are important. The moving average is a rolling average. If the moving average is high, the sampling is high. When the sampling rate is increased to its highest setting (e.g., 2.55μs) some accuracy could be lost. Experience during this research revealed that an average setting of 256 and 50 kHz or 100 kHz sampling rate would be sufficient for seismic frequencies testing.

3.2.3 Pressure Transducer

All the load cells, pressure sensors, and external LVDT are connected to the system with +/- 0.10% accuracy. The applied confining pressure, pore pressures, axial displacements, differential pressure, and cell and room temperature, and all pump data are logged, logged at 5 seconds increments using a custom-built logging software system. Figure 3-15, Figure 3-16, Figure 3-17, Figure 3-18, and Figure 3-19 are the calibration results of the sensors.

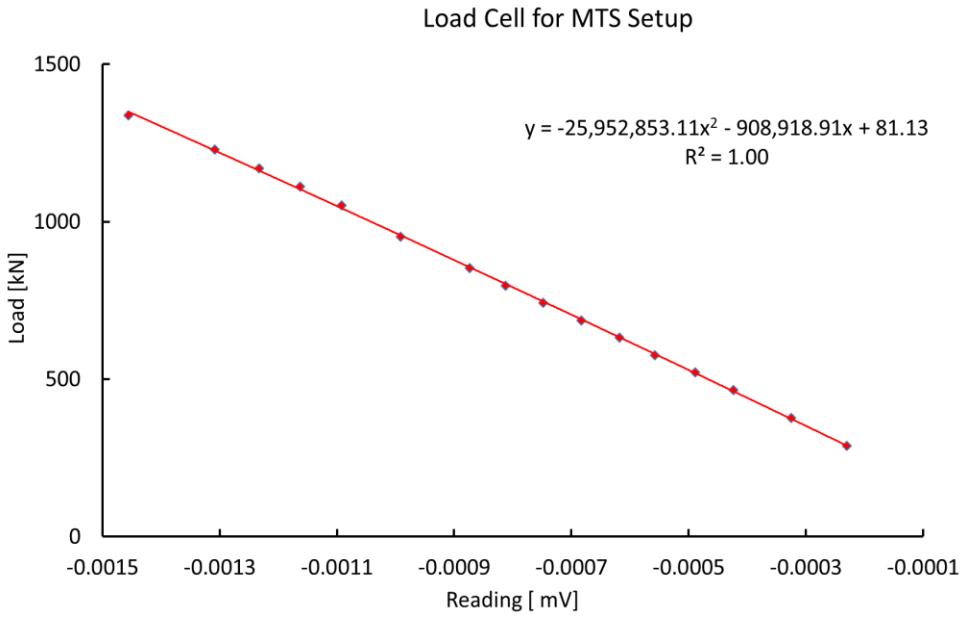

Figure 3-15 Calibration results of load cell.

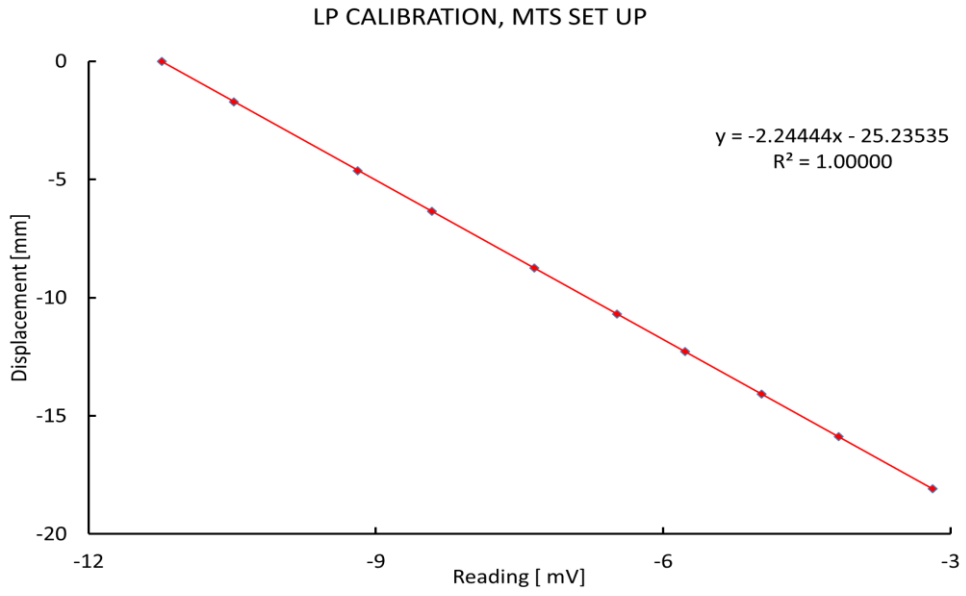

Figure 3-16 Calibration results of LVDT.

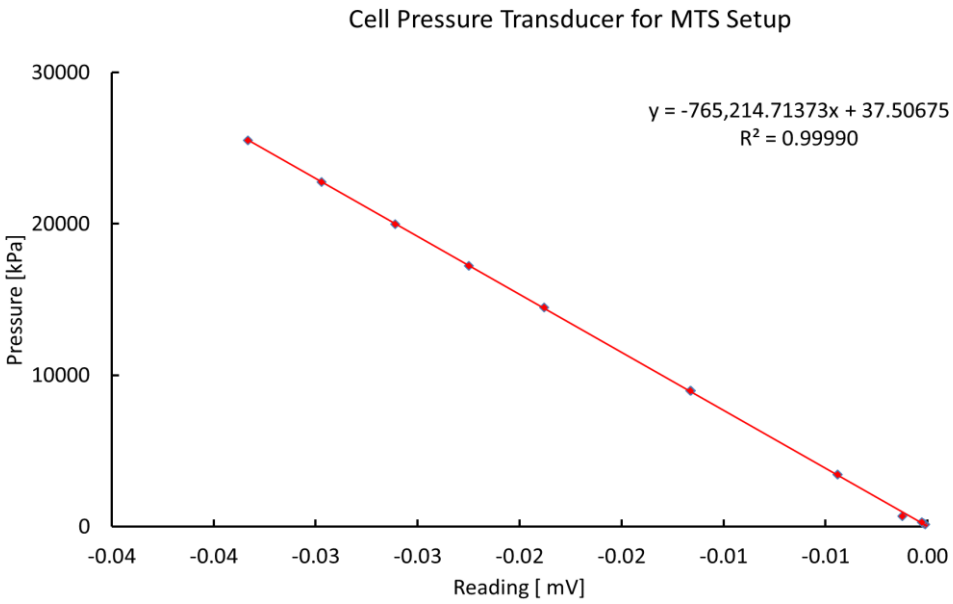

Figure 3-17 Calibration results of cell pressure transducer.

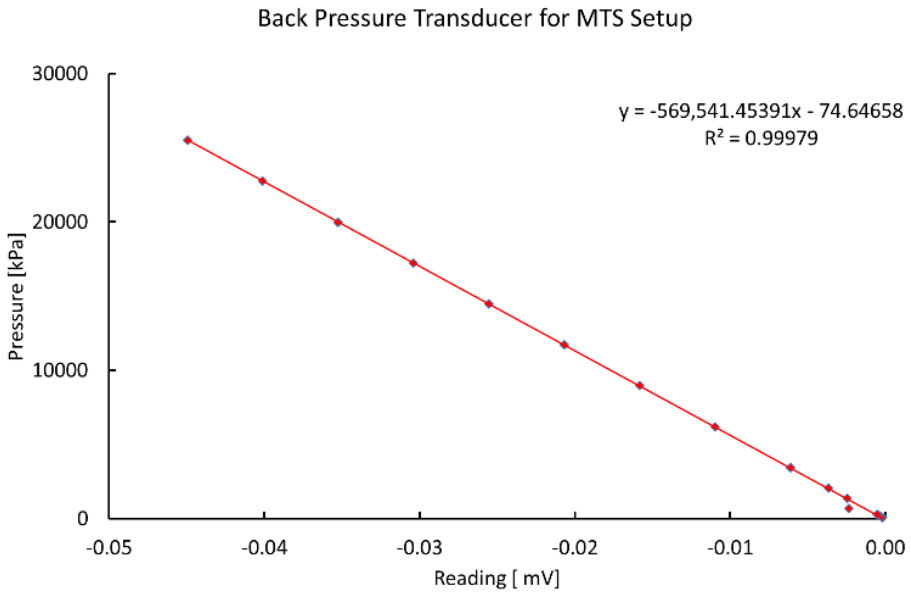

Figure 3-18 Calibration results of back pressure transducer.

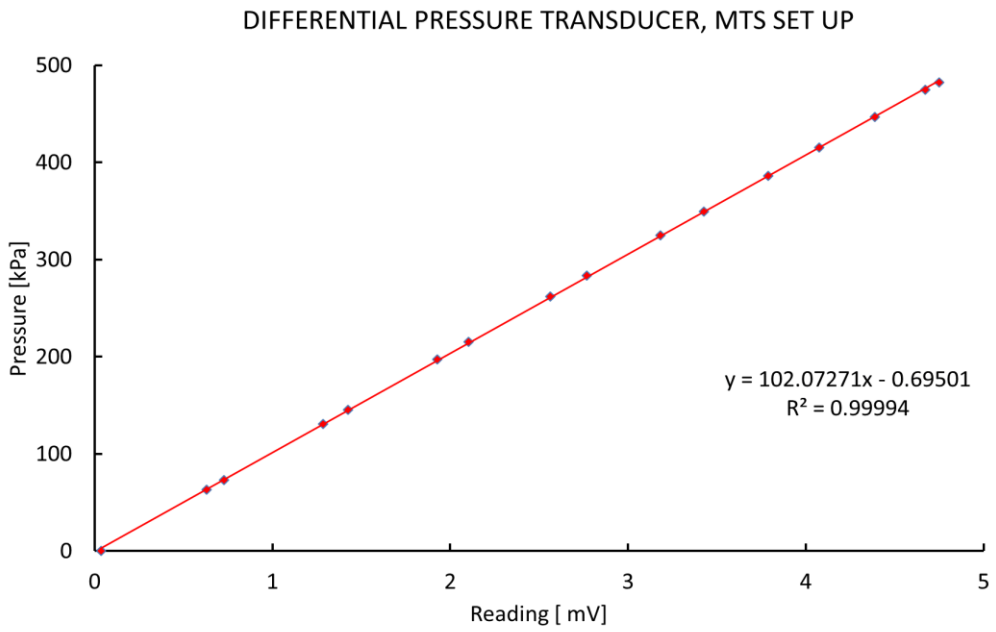

Figure 3-19 Calibration results of the differential pressure transducer.

3.2.4 Temperature Fluctuations

Since the measurement is in nm scale, the test result is sensitive to the room temperature. The findings in Figure 3-20 and Figure 3-21 only apply with MTS are not using the actuator. The two tests were conducted at different preloading, 7 kN and 8 kN respectively. The load cell of MTS and another mini load cell calibrated in the previous section were used. From the results, I concluded that the load drift was due to temperature fluctuations. Normally, the MTS system controls this with the actuator. This effect is more visual with the mechanic's crew is used for seismic frequencies measurement. It is better to insulate the frame and all the systems to reduce the temperature effect. However, during the dynamic testing, the actuator engages and can control the temperature fluctuation. Another test is conducted to check if the MTS actuator feedback loop will work to maintain an "external" load very steady by adding just 1kN with the same actuator, and the result shows a good performance (+/- 5N fluctuation).

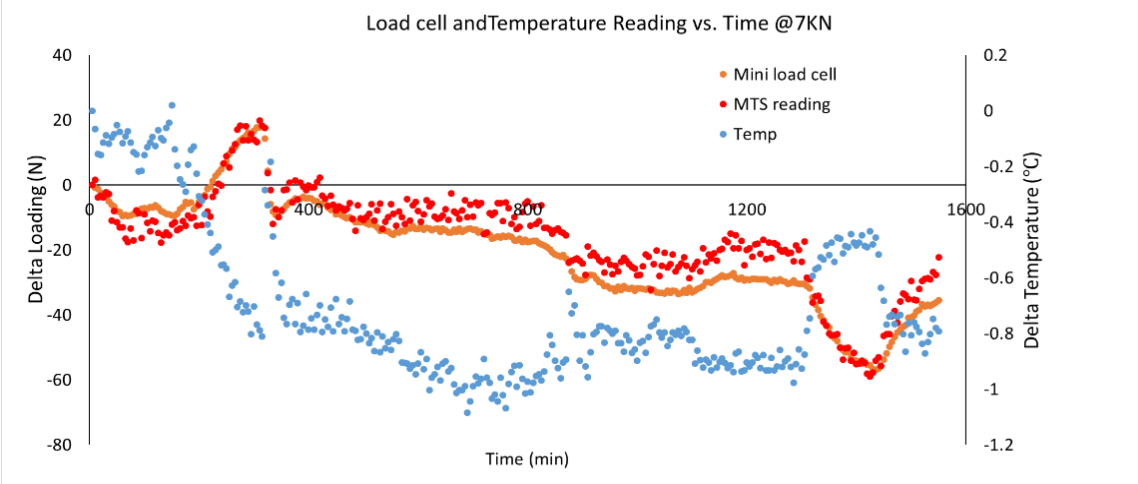

Figure 3-20 Temperature fluctuation from two different load cells at 7 kN without the actuator compensation during long-term testing.

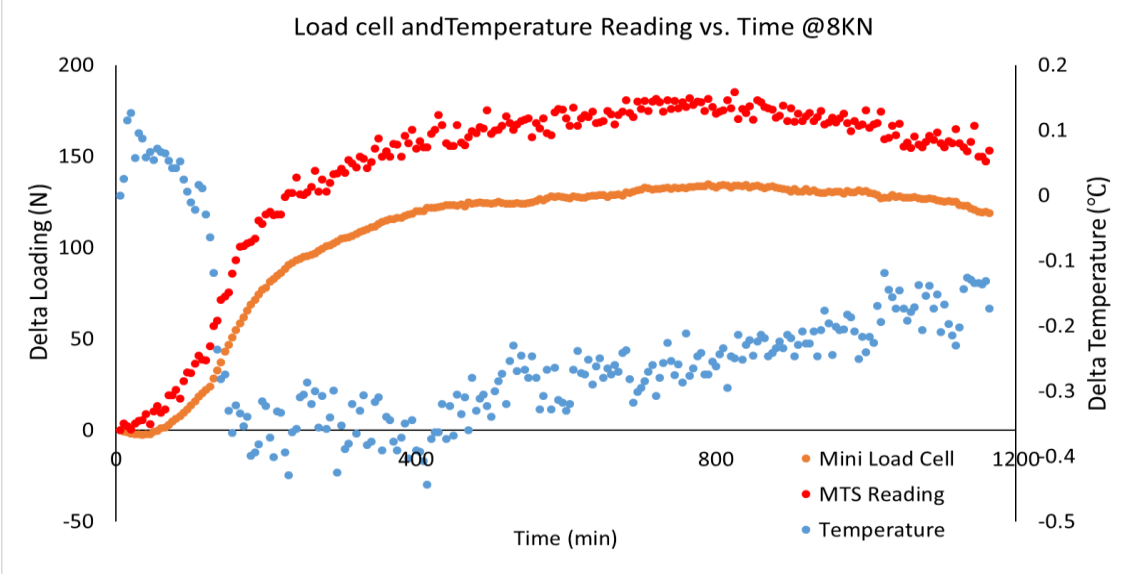

Figure 3-21 Temperature fluctuation at 8 kN from two different load cells without the actuator compensation during long-term testing.

This chapter shows all the tuning procedures and calibration results. Many trials have been conducted by using MTS. To obtain precise results with high resolution, all sensors have been calibrated under different pressure and temperatures. The following section will discuss the UCS tests which were conducted on 3D printed samples.

4 TESTING WITH 3D PRINTED SAMPLES

4.1.Abstract

In this study, a new experimental system that can measure static and dynamic elastic properties at seismic frequencies under deviatoric stress is described. This geomechanical rock physics system was developed specifically for poorly consolidated oil sands and highly overconsolidated (clay) shales and focused on the ability to measure in the seismic frequency range of 0.1 Hz to 20 Hz under anisotropic and deviatoric stresses. The system has been tested and calibrated using aluminum and acrylic specimens. Initial tests using additive manufacturing technology specimens as sandstone analogues were then tested and showed no observed dispersion. The loading stress path and unloading stress path have also been recorded during the seismic frequency measurements. The study results provide a possible analytical method to correlate ultrasonic data, well logging data, and seismic data, and will benefit time-lapse seismic simulation interpretation.

4.2.Introduction

Laboratory studies on several different rock types have been conducted using dynamic ultrasonic measurement (MHz) and high-amplitude static stress-strain measurement, however, the experimental data obtained from intermediate seismic frequencies band is still missing (Spencer 1981; Jackson and Paterson 1987; Paffenholz and Burkhardt 1989; Batzle et al., 2006; Tisato and Madonna 2012; Madonna and Tisato 2013; Mikhaltsevitch et al., 2014; Szewczyk et al., 2018). The effects of frequencies on geomechanical behaviour and the critical parameters that influence stress-strain behaviour require investigation. Information from seismic data and laboratory measurements of rock and fluid properties are essential for a better understanding of physical mechanisms at seismic frequencies. The research gap between rock physics and geomechanics leads to neglecting or not understanding dynamic rock property changes during rock deformation caused by SAGD production and gas injection recovery strategies (Zhang and Okuno, 2015). In order to interpret seismic waves travelling in the rock formations, the strain of the specimen should be smaller than 10^{-6}, where attenuation is linear (Iwasaki et al., 1978; Winkler, 1979).

Most researchers use strain gauges as a displacement sensor. However, there are several disadvantages. Strain gauge measurement is only capable of point measurement and the accuracy is likely influenced by the anisotropic behaviour. They are also temperature-dependent and require extensive calibration for high-temperature testing (Behura et al., 2007). Lastly, existing seismic frequency measurement apparatus is mostly performed under hydrostatic pressure conditions (Subramaniyan et al., 2014). These shortcomings make the apparatus unable to combine seismic frequency rock physics testing and geomechanical testing.

4.3.Objective

The primary objectives of this research are to design reasonable and feasible experimental protocols that guide the infrastructure and process required to conduct seismic frequency dynamic property measurements from 0.1 Hz to 20Hz. The new apparatus is designed based on the MTS system with a pair of laser displacement sensors and calibrated by using two standard samples, aluminum, and acrylic. Using additive manufacturing technology (3D printing), grain size, mineralogy, cementing type and amount, bedding orientation, and discontinuities can be controlled to demonstrate the capacity and stability of the system from 0.1Hz to 20Hz (Primkulov et al., 2017; Gomez et al., 2017; Chalaturnyk et al., 2017).

4.4.Methods

The principle of the seismic frequency apparatus is the application of an oscillating force (stress) and measurement of the resulting displacement (strain). Additive manufacturing technology is used in this research. The advantage of this technology is to reduces specimen-to-specimen heterogeneity. By calculating the incremental stress and resulting strain, moduli at seismic frequencies can be determined. The time lag between stress and strain is the attenuation of the specimen. Many researchers have proven that the stress-strain method is the only way to measure geomechanical properties at seismic frequencies (Batzle et al., Hofmann, 2006; Subramaniyan et al., 2014). Although the principle is straightforward, experimentation demands a uniform sinusoidal actuator, a sensitivity displacement sensor, and careful calibration. The following

sections will introduce the innovative seismic frequency apparatus established by the Reservoir Geomechanical Research Group at the University of Alberta.

The forced oscillation system consists of three essential components: 1) An actuator that can generate a uniform force in a sine wave pattern below a strain of 10^{-6} to the specimen; 2) A force sensor capable of measuring the applied force; 3) A displacement sensor to monitor the nm scale displacement of the sample.

The MTS (370.50) system is a computer-controlled load frame capable of delivering up to 250 kN (Figure 4-1). MTS contains a hydraulic service manifold (HSM) next to a hydraulic power unit (HPU). A. With electrically operated valves, the HSM makes hydraulic oil available to the servo valve. Pumps provide fluid flow for the actuator connected to the HSM and apply movement or force to the test specimen. The actuator is designed for maximum speeds, frequencies, or forces. Based on this hardware, the actuator can move from 0.1 Hz to 50 Hz.

Beneath the actuator, a Linear Variable Displacement Transducer (LVDT) with a sensitivity of one μm is used to measure the displacement of the actuator needed for static modulus calculation measurements. The force is measured with a 250kN load cell.

Prior to forced oscillation testing, tuning the MTS system is critical. Tuning affects the response and stability of the servo control loop, and proper tuning improves the performance of the system, eliminating the stiffness effect from the specimen. The MTS has two control modes, force and displacement, and each control mode uses a different sensor feedback signal for servo loop control. Each control mode must be tuned via PID tuning provided by the MTS system. The speed of the actuator response is adjusted with P gain. As proportional gain increases, the actuator response improves, and the feedback signal more closely matches the input commands. Too much proportional gain causes the system to become unstable (Figure 4-2) while too little proportional gain can cause the system to lag. Therefore, a proper proportional tuning gain should be identified so that its servo loop responds to the command signal accurately.

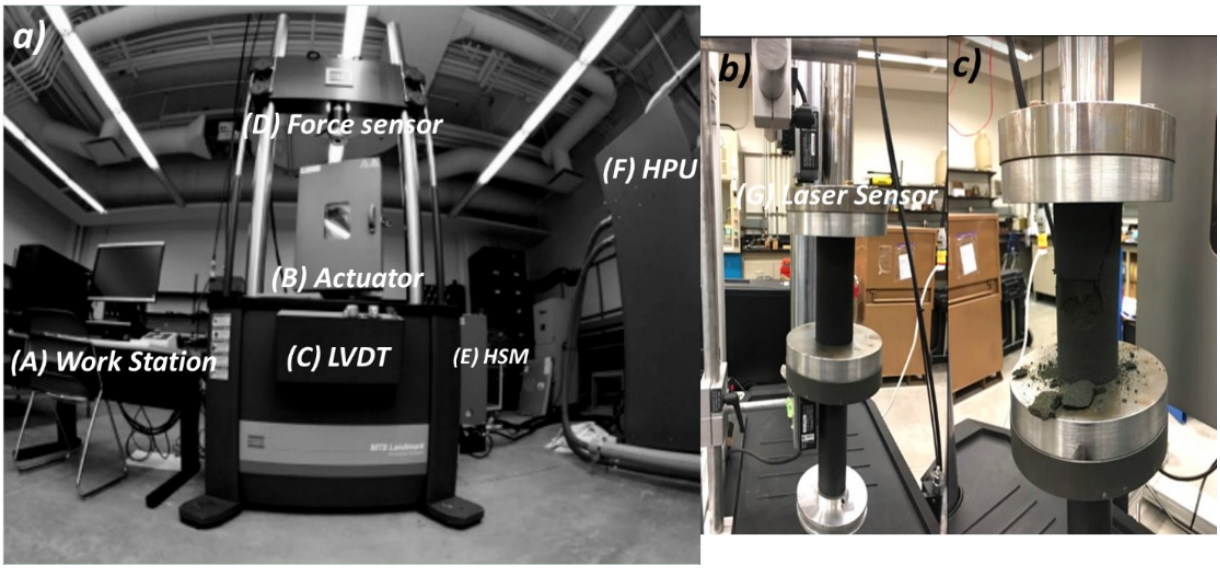

Figure 4-1 a) schematics of the MTS system (A) workstation, (B) actuator for generating the sinusoidal force from 0.1Hz to 20Hz, (C) linear variable displacement transducer (LVDT) to measure the moving displacement of the actuator, (D) force sensor for measuring the applied force, (E) hydraulic service manifold (HSM) and (F) hydraulic power unit (HPU). b) UCS test with laser displacement sensors (G) to measure the axial displacement. c) 3D printer sample after the UCS test.

Displacement of the sample is measured by a pair of LK-H008 laser sensors with a resolution of 5 nm ± 0.02% accuracy and a distance of 8mm, which is sufficient for seismic frequency measurement (Figure 4-1). The sensors measure the top and bottom platen movement and calculate the difference between the sensors to obtain the strain. Initially, the lasers were mounted to the MTS machine but vibration during testing caused measurement errors. A custom frame with vibration dampeners independent of the MTS was designed to mount the pair of sensors to eliminate these errors. A vertical and horizontal micrometre is incorporated to adjust the proximity of the laser displacement sensor to the platens, allowing for μm adjustments with 5mm total travel length.

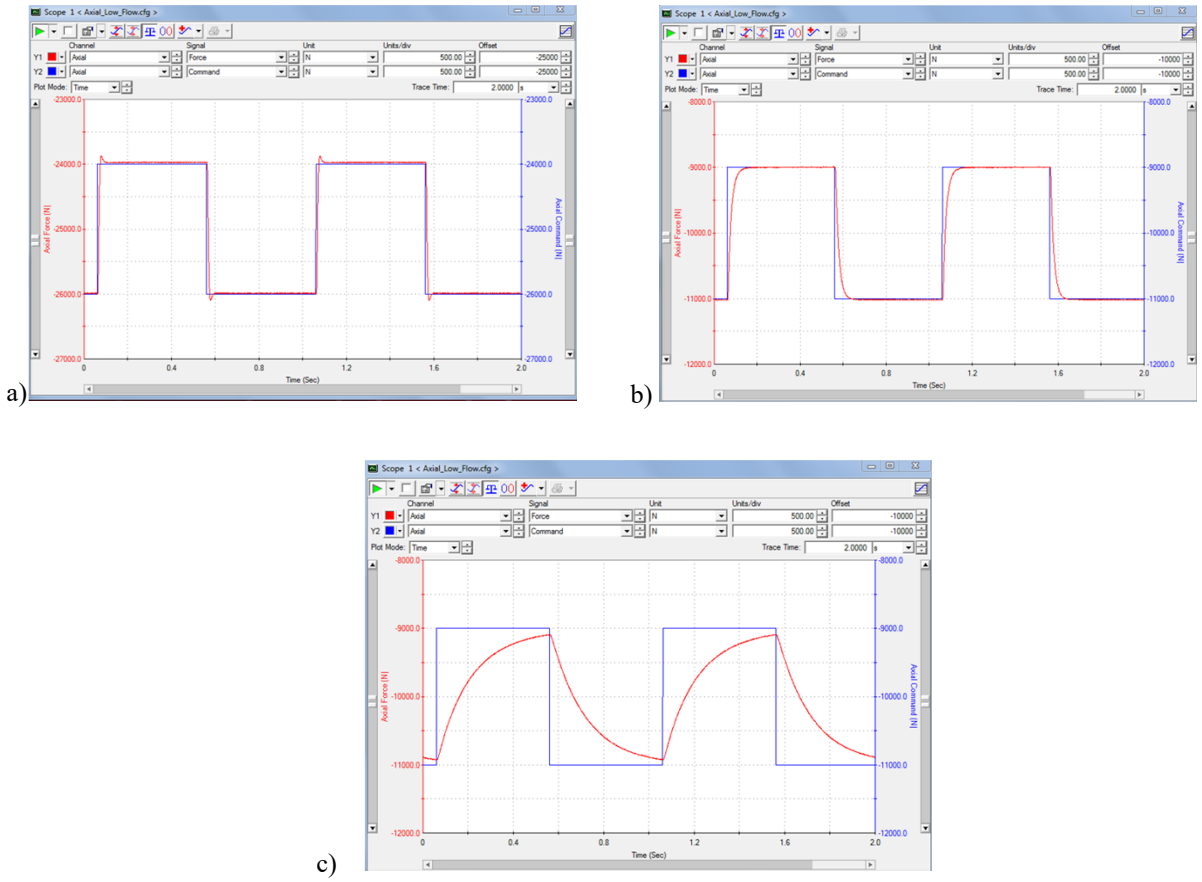

Figure 4-2 PID tuning in the force control mode of the 250 kN MTS system. a) The gain value is too high, b) Gain value is optimum and c) Gain value is too low.

The complete details to set up the MTS frame and laser sensors are:

1. Move the actuator to zero position to make sure the LVDT has sufficient travel;
2. Precisely center the specimen on the loading plate. If the specimen is not centred, a flexural motion of the platen will be observed;
3. Move the load frame slowly downward until the desired initial vertical load is measured;

From the PC, set the amplitude and the frequency for the test. All data from the load cell meter, laser displacement sensor, and LVDT is logged. By simulating the sine wave curve, the displacement can be obtained (Figure 4-3).

Young's modulus and attenuation can then be calculated.

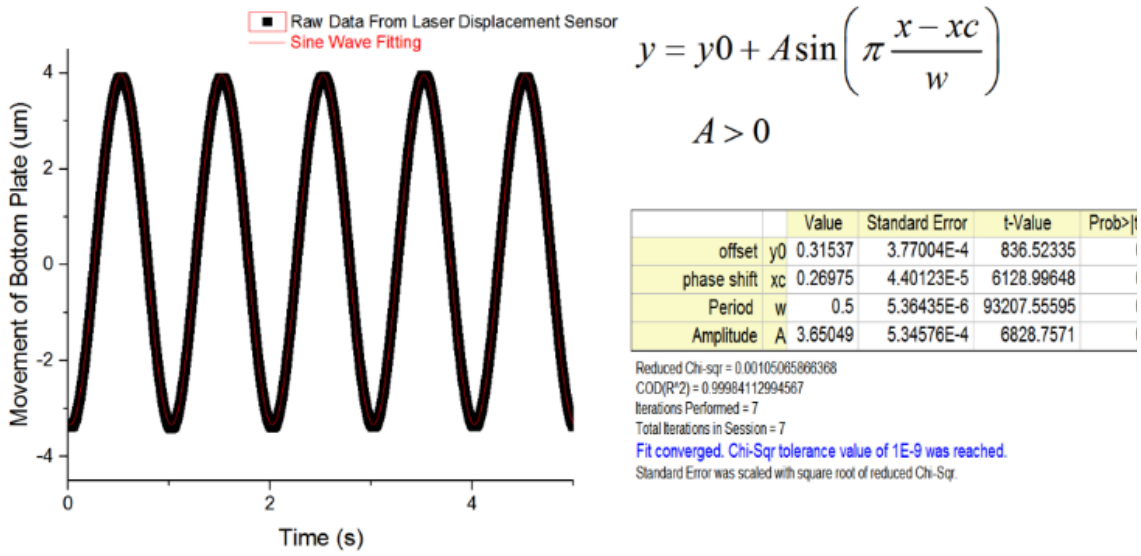

Figure 4-3 Raw Data from Laser Displacement Sensors with Sine Wave Fitting Result at Frequency=1 Hz.

4.5.Results

4.5.1 Calibrations

Aluminum and acrylic cylinders are isotropic and homogeneous. These materials are chosen for the calibration tests as the properties of these two samples have been studied sufficiently. Since aluminum is non-dispersive material(Young's Modulus = 68.9 GPa) it is a suitable material for seismic frequency measurements. The aluminum tested has a cylindrical shape: 126.80 mm in length and 63.63 mm in diameter. The measurement is conducted under the axial stress of 3.14 MPa and 6.28 MPa. The frequency limit is from 0.01Hz to 50 Hz for aluminum. Results of aluminum measurements are shown in Figure 4-4a) and b), confirming that the apparatus is stable and reliable. This agrees with results measured by other apparatus (Spencer, 1981; Lakes, 2009; Takei et al., 2011; Tisato and Quintal, 2014). However, we should notice that when the frequency is at 35 Hz, there is a significant fluctuation for which the reason is unclear. Also, errors in Young's modulus are generally more significant for stiff materials like aluminum shown by Spencer (1981); one of the advantages of our system is that the tuning technique will remove this issue.

The second calibration sample is acrylic (Koppelmann, 1958; Spencer, 1981; Yee and Takemori, 1982; Batzle et al., 2006; Nakagawa, 2011; Takei et al., 2011; Tisato et al., 2012; Madonna and Tisato, 2013). Acrylic is a dispersive material. The specimen had a cylindrical shape: 126.77 mm in length and 63.57 mm in diameter. Results of the acrylic measurements are shown in Figure 4.4 c) and d). For Young's modulus, our seismic frequency system returns a stable result. The result of attenuation measurement is not constant when the frequency is tested to 20Hz as the sampling rate is insufficient. When frequency increases, the time delay will decrease to 0.2s, however, the maximum sampling rate is 0.2414s. Despite this, the overall capacity and stability of the new system have been proven. The frequency limit for the system is between 0.1Hz and 20Hz in this study.

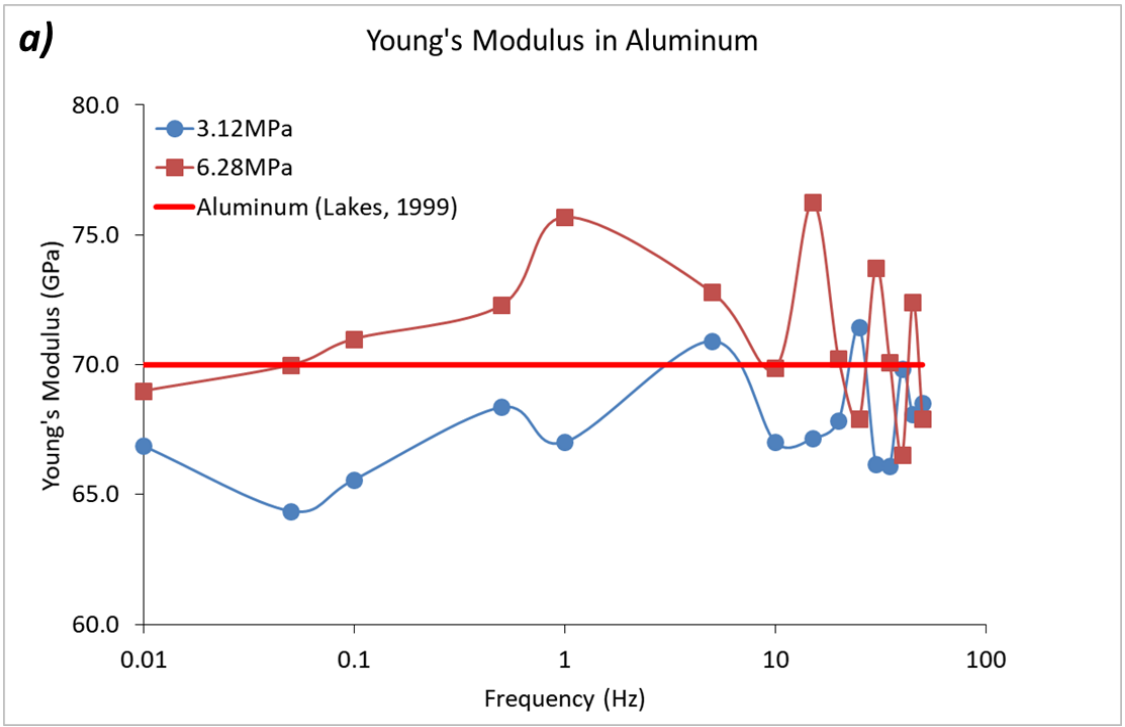

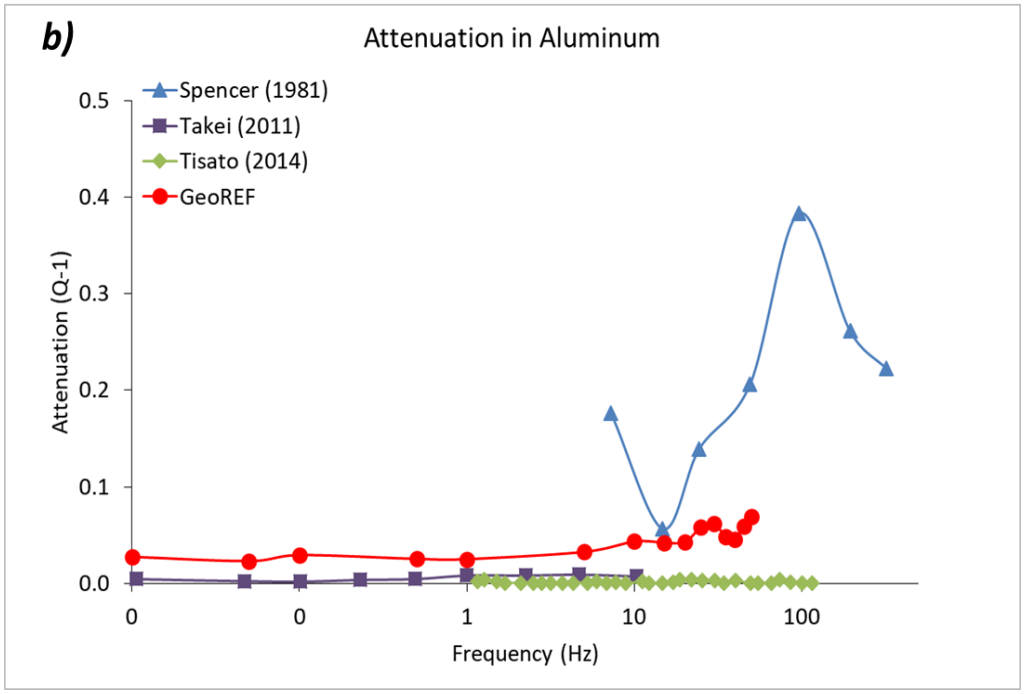
b)
Attenuation in Aluminum
Spencer (1981)
Takei (2011)
Tisato (2014)
GeoREF
Attenuation (Q-1)
0.5
0.4
0.3
0.2
0.1
0.0
0
0
1
10
100
Frequency (Hz)

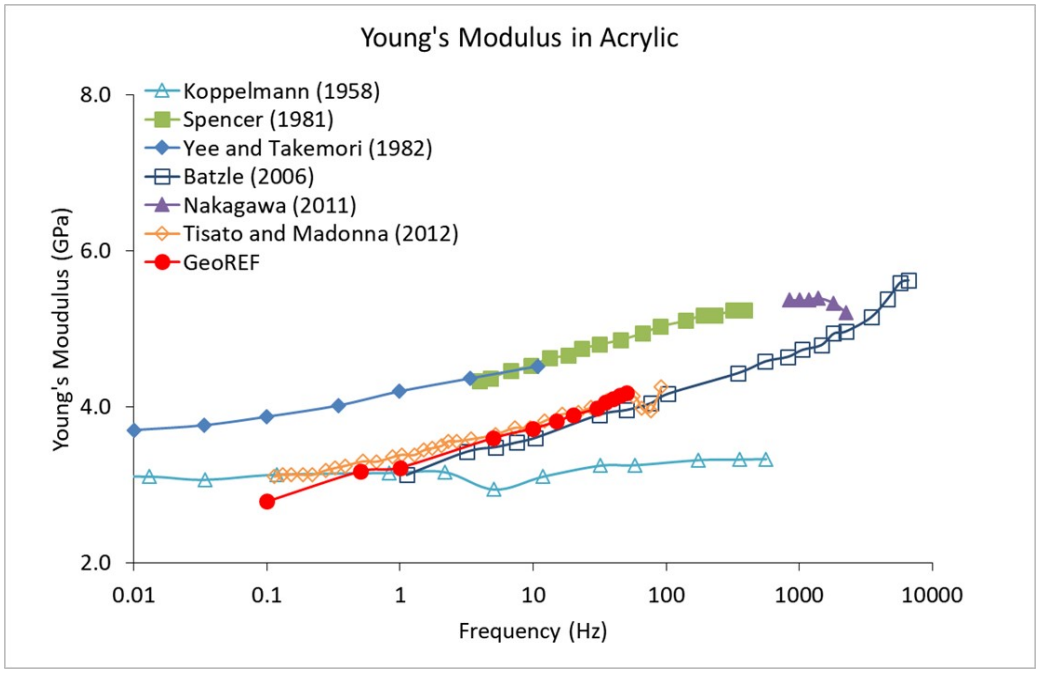
Young's Modulus in Acrylic
Koppelmann (1958)
Spencer (1981)
Yee and Takemori (1982)
Batzle (2006)
Nakagawa (2011)
Tisato and Madonna (2012)
GeoREF
Young's Moudulus (GPa)
8.0
6.0
4.0
2.0
0.01
0.1
1
10
100
1000
10000
Frequency (Hz)

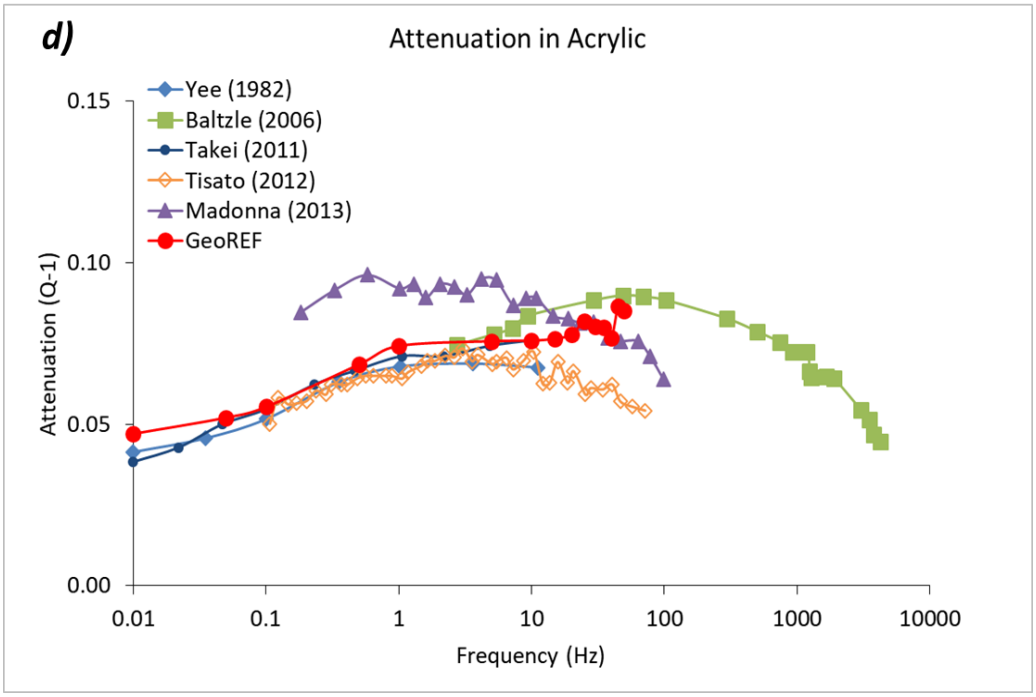

Figure 4-4 a) Young's modulus and b) attenuation of aluminum measured at seismic frequencies (0.01Hz-50Hz). The measurement is conducted under the axial stress of 3.14 MPa and 6.28 MPa. c) Young's modulus and d) attenuation of acrylic measured at seismic frequencies (0.01-50Hz).

4.5.2 3D Print Samples description and preparation

Advances in 3D additive manufacturing binder jet technology have enabled printing sandstone analogs using the ExOne MFlex 3D Printer (2014). The primary procedure is mixing the sand powder (ExOne, PA, USA) with an acid catalyst, alternating deposition of sand and binder on the print bed, then curing the printed pieces in an oven for the desired period. Five differently oriented 3D printed samples were created to investigate the influence of specimen anisotropy on geomechanical properties. The physical parameters of the samples are as follows: porosity is 35.7%, permeability is 1200mD, and particle size distribution of D10, D50, and D90 is 110, 175, and 220 μm, respectively (Osinga et al., 2015). The 3D printed samples are cylindrical in shape and the ratio of the length and diameter is 2:1.

Unconfined compressive strength (UCS) tests are conducted on the MTS system (see below for details) for a precise constant strain rate of 0.1mm/min. Data dropping to zero force due to splitting of the sample, indicated that samples had been loaded to the failure point. From the stress-strain

relationships, Young's modulus and peak stress are obtained (Table 4-1). From the high magnification optically transmitted bright-field image (Figure 4.5), the binder can be found accumulated near the sand grain contracts. The displacement of the specimen during dynamic loading can be at the nm scale. As the uneven surface will increase errors during testing, careful polishing of the specimens was conducted to ensure the cylinders were optimal for use. Before testing, printed pieces are placed in the oven for two days to ensure the samples are completely dry.

Table 4-1 Summary of 3D printer samples physical properties and geomechanical properties.

NO.	Layer Orientation (°)	Sample Dimensions L*R (mm)	Young's modulus (GPa)	UCS (GPa)
1	0	126.89*63.52	2.92	35.56
2	30	127.80*63.56	2.89	25.19
3	45	128.03*64.21	2.67	20.18
4	60	128.03*63.82	2.62	33.44
5	90	127.47*63.76	2.38	31.98

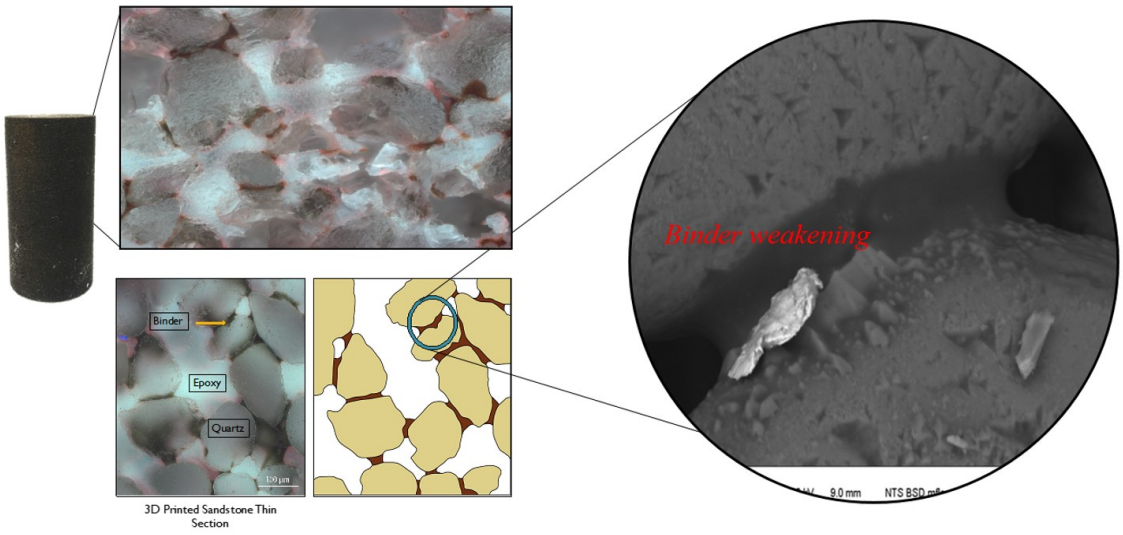

Figure 4-5 Typical grain matrix of 3D printed sandstone analogs. The image was obtained on a polished section of a UV-fluorescent polymer saturated sample. The binding resin shows dark spots between the grains. (modified from (Hodder, Nychka and Chalaturnyk, 2018)).

4.5.3 Analogue Sandstone Tests and Results

Five different specimens are printed at 0°, 30°, 45°, 60° and 90° with respect to the bedding. Each of the specimens follows the same axial stress loading path and is then tested once the stress and displacement have reached equilibrium. The axial stress is set to 3.12 MPa, 6.24 MPa, 9.37 MPa, 6.24 MPa, and then 3.12 MPa. At each axial stress state, the specimen is dynamically tested from 0.1 Hz to 20 Hz. The static Young's modulus was calculated at each incremental stress and then compared with the dynamic measurement (Figure 4.6).

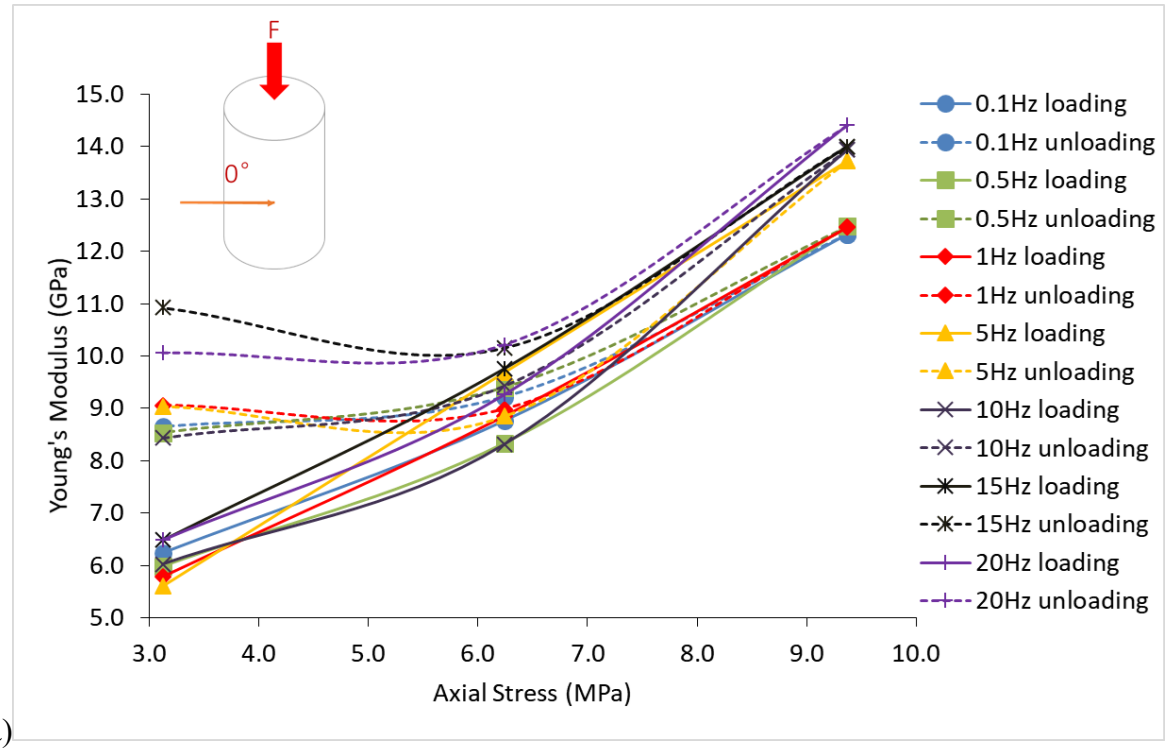
F
0°
Young's Modulus (GPa)
Axial Stress (MPa)
15.0
14.0
13.0
12.0
11.0
10.0
9.0
8.0
7.0
6.0
5.0
3.0
4.0
5.0
6.0
7.0
8.0
9.0
10.0
0.1Hz loading
0.1Hz unloading
0.5Hz loading
0.5Hz unloading
1Hz loading
1Hz unloading
5Hz loading
5Hz unloading
10Hz loading
10Hz unloading
15Hz loading
15Hz unloading
20Hz loading
20Hz unloading

a)

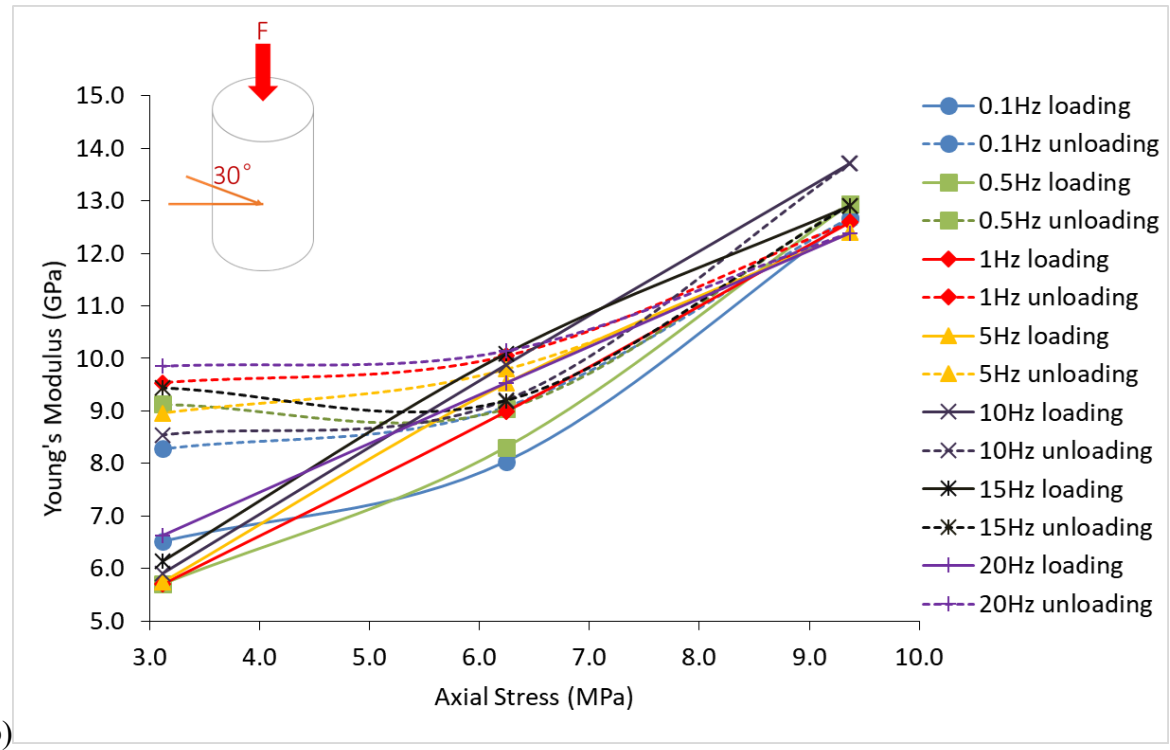
F
30°
Young's Modulus (GPa)
Axial Stress (MPa)
15.0
14.0
13.0
12.0
11.0
10.0
9.0
8.0
7.0
6.0
5.0
3.0
4.0
5.0
6.0
7.0
8.0
9.0
10.0
0.1Hz loading
0.1Hz unloading
0.5Hz loading
0.5Hz unloading
1Hz loading
1Hz unloading
5Hz loading
5Hz unloading
10Hz loading
10Hz unloading
15Hz loading
15Hz unloading
20Hz loading
20Hz unloading

b)

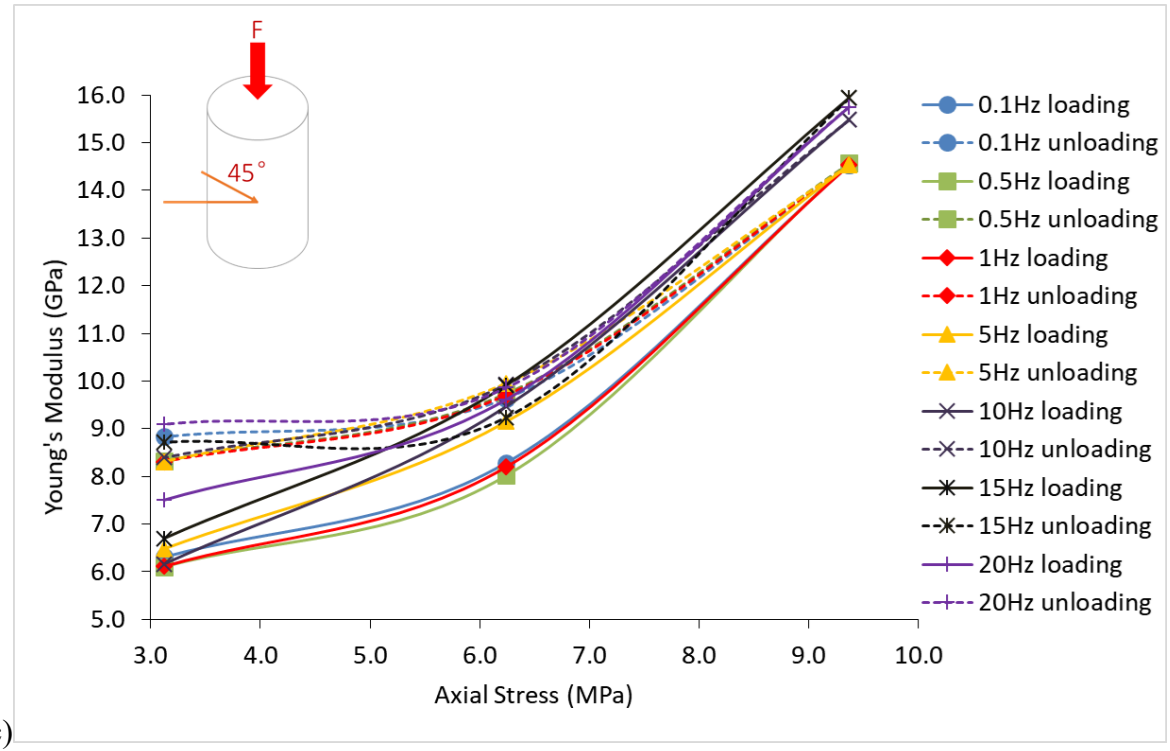
F
45°
Young's Modulus (GPa)
Axial Stress (MPa)
16.0
15.0
14.0
13.0
12.0
11.0
10.0
9.0
8.0
7.0
6.0
5.0
3.0
4.0
5.0
6.0
7.0
8.0
9.0
10.0
0.1Hz loading
0.1Hz unloading
0.5Hz loading
0.5Hz unloading
1Hz loading
1Hz unloading
5Hz loading
5Hz unloading
10Hz loading
10Hz unloading
15Hz loading
15Hz unloading
20Hz loading
20Hz unloading

c)

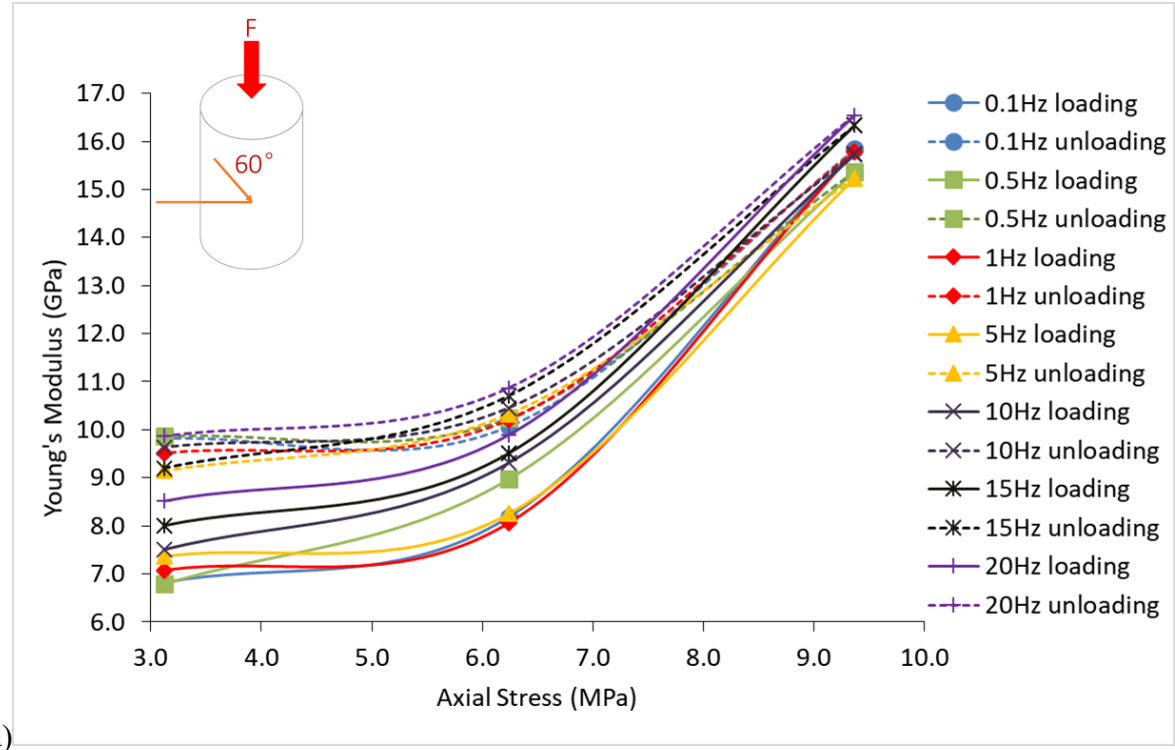
F
60°
Young's Modulus (GPa)
Axial Stress (MPa)
17.0
16.0
15.0
14.0
13.0
12.0
11.0
10.0
9.0
8.0
7.0
6.0
3.0
4.0
5.0
6.0
7.0
8.0
9.0
10.0
0.1Hz loading
0.1Hz unloading
0.5Hz loading
0.5Hz unloading
1Hz loading
1Hz unloading
5Hz loading
5Hz unloading
10Hz loading
10Hz unloading
15Hz loading
15Hz unloading
20Hz loading
20Hz unloading

d)

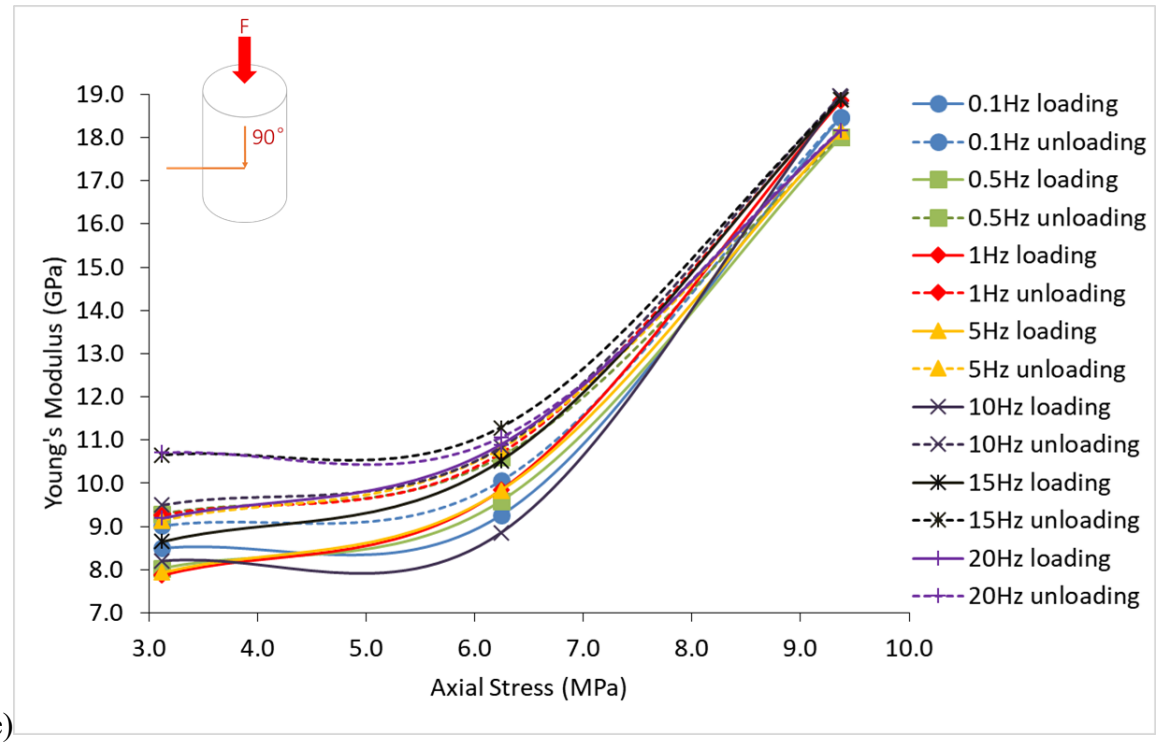

e)

Figure 4-6 Impact of Loading and unloading path on Young's modulus from 0.1Hz to 20 Hz at a) 0°, b) 30°, c) 45°, d) 60° and e) 90° with respect to the bedding

4.6.Discussion

The system in GeoREF allows calculation of both the static and dynamic Young's modulus. Since the tests were conducted under different axial stress, the static Young's modulus changed during the test as well. Figure 4-7 shows the test procedure of this research. In the elastic region, the static Young's modulus is calculated from the slope of the stress-strain curve. The results shown in Table 4-2 summarize the static Young's modulus of the 3D printed samples at each incremental stress. As expected, Young's modulus increases as stress increases. The dynamic Young's modulus is calculated using the stress-strain method (Spencer, 1981; Batzle et al., 2006) at each incremental stress. The displacement (d) was obtained from two laser sensors by simulating the raw experiment data:

$$y = y_0 + dsin(\pi \frac{x - xc}{w}) \qquad 4\text{- }1$$

So the dynamic Young's modulus is (E):

$$E = \frac{\sigma}{\varepsilon} \quad 4\text{-}2$$

$$\sigma = \frac{F}{S} \quad 4\text{-}3$$

$$\varepsilon = \frac{d}{L} \quad 4\text{-}4$$

where σ is the stress, ε is the strain, F is the loading force from the MTS system, S is the cross-sectional area of specimens and L is sample length.

Table 4-2 Summary of 3D printer samples static Young's modulus at each incremental stress.

NO.	Layer Orientation (°)	Young's modulus @3.12 MPa (GPa)	Young's modulus @6.24 MPa (GPa)	Young's modulus @9.37 MPa (GPa)
1	0	1.89	2.36	2.63
2	30	1.94	2.56	2.87
3	45	1.82	2.50	2.69
4	60	1.61	2.18	2.49
5	90	1.46	1.92	2.22

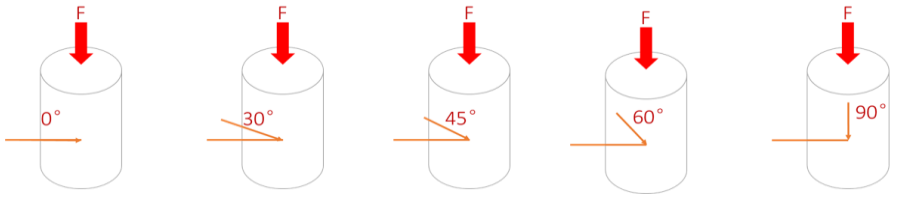

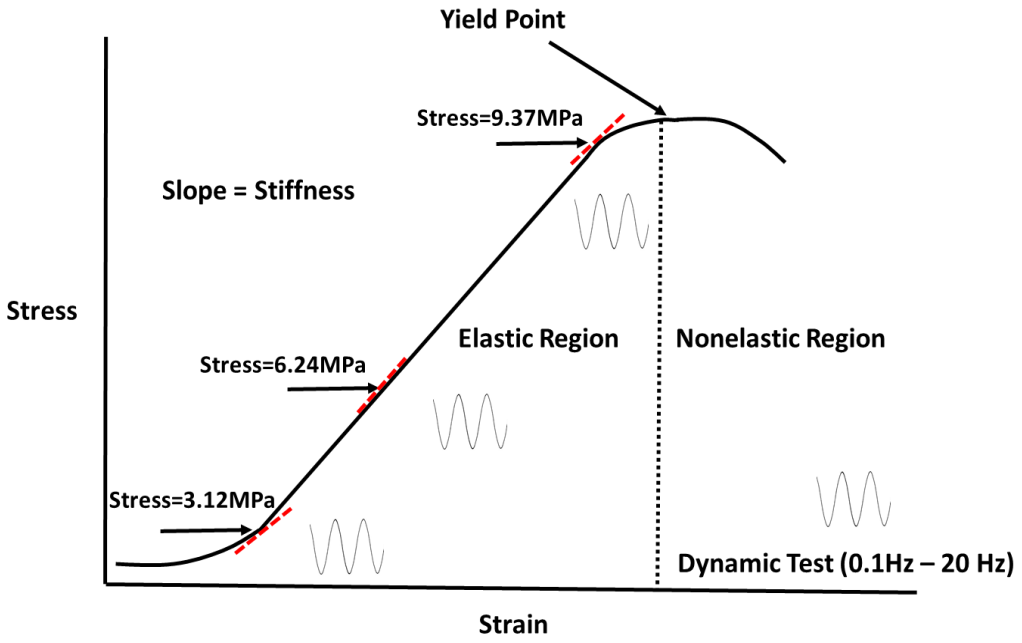

Figure 4-7 The schematic of the test procedure and the calculation method of both static and dynamic Young's modulus during the tests.

Figure 4.6 shows the relationship between the dynamic Young's modulus and the axial stress. The testing runs from 0.1Hz to 20Hz based on the calibration tests. The dynamic Young's modulus of the 3D printed sample increased as axial stress increased, as was the case with the static Young's modulus. In comparison, the dynamic Young's modulus is significantly higher (~300%) than the static Young's modulus. This is because stress-strain relations for 3D printed samples are always nonlinear making the ratio of stress to strain over a UCS test (large strain measurement to the order of 10^{-2}) is different from the ratio of stress to strain over a forced oscillation test (small strain measurement of the order of 10^{-6} or less). Results show that the dynamic Young's modulus of the No.1, No. 2, and No. 3 3D printed samples are almost the same, but the dynamic Young's modulus of the No.4 and No.5 3D printed samples are higher. Also, Young's modulus of the No.4 and No.5 3D printed samples are not sensitive to the lower stress but increased significantly at higher stress under the loading path. This is because when using 3D additive manufacturing binder jet technology more binding resin accumulates on the No.4, and No.5 3D printed samples, increasing the contact area of No.4 and No.5 3D printed samples. Additionally, the axially applied force is parallel to the bedding of the No.5 3D printed sample and vertical to the bedding of the No.1 3D printer sample. The bedding can impede and weaken force such that when the bedding direction

increases from 0° to 90°, the bedding and force attenuation decrease, causing the displacement and the dynamic Young's modulus to increase. The initial non-linear trend for the dynamic Young's modulus of the No.4 and No.5 3D printed samples may be due to the natural microfractures and the induced cracks. During the unloading path, the dynamic Young's modulus decreases with the axial stress. Moreover, the values are higher than the corresponding values in the loading path. The reason is that the sand grain may have rearranged under compression. From Figure 4.5, the binder can be found accumulated near the sand grain contracts and the binder weak under stress and frequencies.

In Figure 4.8, the geomechanical properties of three different sandstones are compared with those of the 3D printed samples. Young's modulus is stable from 0.1Hz to 10 Hz for 3D printer samples. A small trend of the increase can be observed when the frequency goes from 10Hz to 20Hz. This non-frequency-dependent attenuation can be caused by the friction between grain and binder, causing the pore space to reduce if the specimen is under higher stress. The No.1, No.2, and No.3 3D printed samples show that Young's modulus is equal, but for the No.4 and No.5 3D printed samples, Young's modulus will increase due to anisotropic behaviour. The results confirm the low and approximate frequency independence at seismic frequency ranges for dry sandstone. The only differences result from the properties of the sandstone samples and the limitation of the seismic frequency measurement apparatus. From Spencer and Shine (2016), we see that results were not the same, even when repeated under the same experimental conditions with the same apparatus. However, we can infer that 3D printed samples have the same geomechanical properties as the softer sandstone samples. The tests on dry 3D printed samples can provide effective rock physics information for fluid substitution calculation.

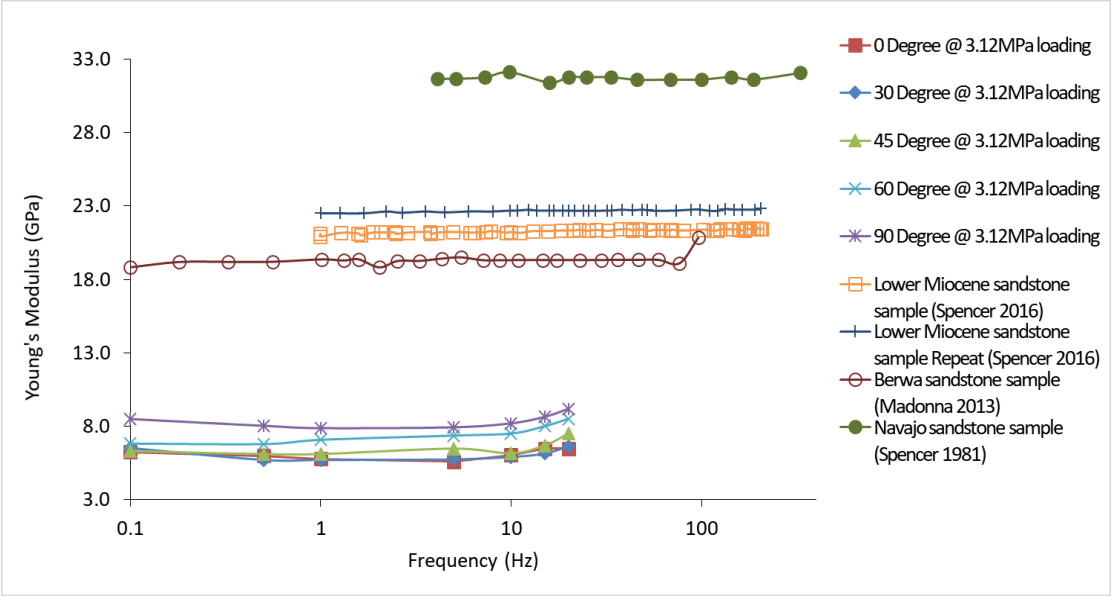

Figure 4-8 Comparison of Young's modulus measured with 0°, 30°, 45°, 60° and 90° 3D printer samples with respect to the bedding and other sandstone publication data. The measurement is conducted under the axial stress of 3.12 MPa.

4.7.Conclusion

A new experimental system has been designed and commissioned to measure dynamic elastic properties at seismic frequencies under deviatoric stress. A specialized servo-hydraulic load frame MTS with a pair of laser displacement sensors is applied in this research. A unique design has been developed to eliminate errors and improve data quality. The calibration has been completed by using aluminum and acrylic, which both have well-known properties. The results show the stability and accuracy from 0.1 Hz to 20Hz. The system performance has been tested using 3D printed sandstone specimens (using sand as the print medium) that provide an unparalleled opportunity to remove inter-specimen variability in the testing. Five different orientation specimens have been tested. Non-dispersion can be found in the 3D printed samples, but anisotropic behaviour can be observed as well as the difference between the loading and unloading paths. The results can be extended to modify and verify the existing models and interpretation templates for seismic and ultrasonic data.

5 TRIAXIAL CELL AND CALIBRATIONS

In this study, a novel experimental system has been developed for static and dynamic elastic property measurement at various seismic frequencies under anisotropic stress. These properties are measured over static and seismic frequency (0.1 Hz to 20 Hz) ranges for poorly consolidated dense sands and highly overconsolidated (clay) shales. The main body of the experimental system is a computer-controlled servo-hydraulic system. A pair of laser displacement sensors measure nanometer-scale displacement during the dynamic tests. A coarse-scale and fine-scale load cell system was developed for measuring force with high precision during dynamic testing. A novel triaxial cell for use with the loading system was also developed to simulate reservoir stress and pore pressure conditions during static and dynamic testing and allows permeability to be measured during testing. The loading system, dual load cell calibration procedure and results, and results for acrylic and 3D printed sand specimens are presented. The stable and reasonable results demonstrate the capacity of the new experimental system.

5.1 **Introduction**

Acoustic measurements have been widely used for oil and gas exploration and production strategy decisions. For example, time-lapse seismic surveys have been widely used for monitoring the fluid saturation, permeability distribution, and pressure changes during production (Lumley, 2001; Helgerud *et al.*, 2011; Schiltz et al., 2014) and the strain magnitude of these acoustic methods are 10^{-6} or less (Iwsaki et al. 1978; Tutuncu et al. 1998; Batzle et al. 2006). Although the strain magnitude of these measurements was the same, the frequency ranges were different. In the laboratory, ultrasonic measurements are conducted at MHz to investigate rock physics properties; geophysical well logging surveys are executed at ~10 KHz to determine the formation information near the borehole, and seismic survey data are collected from 0.1 Hz to 100 Hz to provide detailed images of local structure and reveal reservoir properties. Velocity dispersion occurs and may approach 30% due to the broad frequency ranges in the reservoirs when using different acoustic measurements. Velocity dispersion will cause a significant error when these acoustic measurements data are input to the reservoir simulation if incorrect or no calibration has been completed (Jackson and Paterson, 1987; Batzle and Wang, 1992; Wang, 1997, 2001; King, 2000).

To provide precise predictions on stress-sensitive properties, a rock physics model based on experimental results needs to be developed (Sayers, 2005; Zou et al., 2005; Kato et al., 2008; Vidal-Gilbert et al., 2009; Zhang and Okuno, 2015). However, traditional laboratory measurement of reservoir rocks is conducted at the MHz frequency range which is different from the seismic survey (Tisato and Madonna, 2012; Subramaniyan et al., 2014). Therefore, it is necessary to measure the elastic properties of rocks in the laboratory on core scale samples at seismic frequencies. These measurements are rare since we cannot obtain the velocity directly in the laboratory. For example, if the wave velocity is 3000 m/s, the wavelength will be several orders larger than the test specimen (~3000 m at 1Hz). Therefore, a stress-strain method is an alternative approach to obtain rock dynamic properties in the laboratory (Spencer, 1981; Batzle et al., 2006). By calculating the ratio of the stress to the strain, moduli at seismic frequencies will be obtained under anisotropic stress conditions.

Most current seismic frequencies experimental systems focus on hydrostatic conditions at room temperature using strain gauge measurements (Table 5-1) (Spencer, 1981; Paffenholz and Burkhardt, 1989; Batzle 2006; Tisato and Madonna, 2012; Madonna and Tisato, 2013; Mikhaltsevitch et al., 2014a; Takei et al., 2014; Szewczyk et al., 2016). Rock deformation under high temperature and anisotropic stress will affect the rock physics properties significantly (Li and Chalaturnyk, 2005; Islam and Skalle, 2013; Holt et al., 2018). Therefore, deviatoric stress and pore pressure need to be included in the seismic frequencies measurement system.

Several engineering challenges exist that impede the development of seismic frequencies measurement. First, the applied strain is extremely small. In order to simulate the seismic wave travelling in the formation, the strain level needs to be less than 10^{-6}, which translates to the nanometer scale for the laboratory specimen. Strain gauges are widely used for displacement measurements, but strain gauges are only suitable for local strain and cannot be widely applied for reservoir rocks. Second, a uniform sinusoidal force generator operating in the seismic frequency range is required to induce a very small strain. Finally, a load cell should have the capacity to measure the largely applied stress of a simulated reservoir condition and the small dynamic sinusoidal force. In a large capacity load cell, the error of the cell is larger than the applied dynamic force.

Table 5-1 Summary and comparison of Seismic Frequencies Measurement System under different experimental conditions

	Sample Length × diameter	Displacement Sensor	Frequency Range (Hz)	Confining Pressure (MPa)	Deviatoric Stess	Temperature (□)
Spencer (1981)	140×38.1	Capacitive Transducer	4-400	70 (Nitrogen)	No	No
Paffenholz and Burkhardt (1989)	150×50	Inductive Transducer	0.03-300	No	No	No
Batzle *et al.* (2006)	45×30	Strain Gauges	1-2000	10 (Nitrogen)	No	No
Takei et al. (2011)	15×32.5	Laser Displacement Sensor	0.001-10	No	No	40
Tisato and Madonna (2012)	250×76	Strain Gauges	0.01-100	25(Oil)	No	No
Madonna and Tisato (2013)	60×25.4	Linear Varialbe Differential	0.01-100	50 (Argon)	No	No
Mikhaltsevitch et al. (2014)	70×38	Strain Gauges	0.1-400	70 (Oil)	No	No
Szewczyk et al. (2016)	50.8×25.4	Strain Gauges	1-155	5-20 (Oil)	Yes	No

5.2 **Principle of methods**

The stress-strain technique is the relaxation and noninvasive testing process (Batzle et al., 2006). This is a straightforward method for acquiring core geomechanical properties by recording the stress-strain behaviour of rock (Figure 5-1). The principle is:

- Sinusoidal stress is applied to a right-cylinder rock specimen.
- The strain induced by the applied stress needs to be lower than 10^{-6}, which is at the nanometer scale in a test specimen.
- The displacement is measured with a high-precision displacement sensor, and strain is calculated.
- The Young's modulus of the rock is then calculated using the stress and strain results.

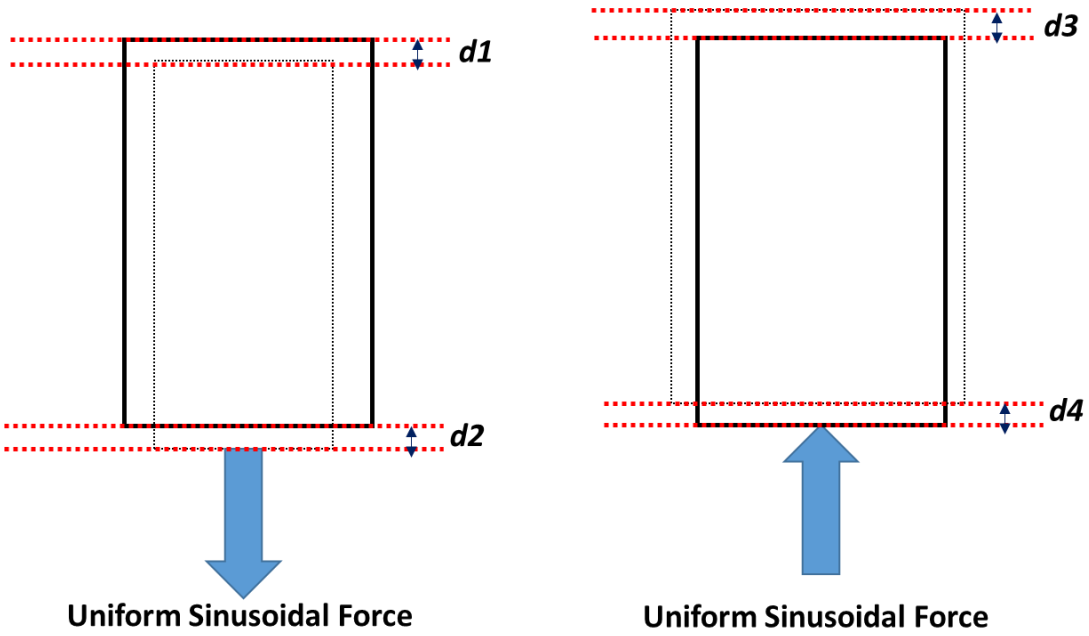

Figure 5-1. Schematic illustration of stress-strain technique assumed by an isotropic specimen.

The displacement of the specimen is calculated through the displacement of the two ends of the specimen:

$$d = \frac{d_2 + d_4 - d_1 - d_2}{2} \qquad 5\text{-}1$$

The stress and strain are:

$$\sigma = F/A \qquad 5\text{-}2$$

$$\varepsilon = d/L \qquad 5\text{-}3$$

where A and L represent sample cross-sectional area and sample length, respectively.

Young's modulus E is

$$E = \sigma/\varepsilon \qquad 5\text{-}4$$

Based on these principles, the stress-strain setups are composed of three main components: (i) force generator to apply the uniform sinusoidal force to the sample; (ii) displacement sensor to record the sample strain response and (iii) force sensor to estimate the applied stress. To simulate actual reservoir conditions, a novel triaxial cell was developed for different pore pressure and confined pressure conditions and is described in the following section.

5.3 **Experimental Apparatus and Sample Preparation**

The experimental apparatus was designed and constructed with a focus on seismic frequency measurements and the determination of deformation-dependent dynamic properties. To investigate these properties at different pore pressure, radial and axial stress, and even high temperatures, the dynamic measurements are conducted in a novel confining triaxial system.

5.3.1 Testing cell

The triaxial cell (Figure 5-2) was designed to have maximum independent axial and radial operating stresses of 45 MPa (6500 psi), maximum pore pressure of 27.5 MPa (4000 psi), and a maximum temperature of 60°C (140°F) with an overall factor of safety of 4.0. The cylindrical cell has a height of 200.7 mm (8.0 in) and a diameter of 114.3 mm (4.5 in). All parts are constructed from AISI 4140 QT steel with a yield stress of 758 MPa (110 000 psi). All flow and cell pressure stainless steel tubing lines are 6.35 mm (¼ in) and enter through the cell base. Split rings are used to seal the testing cell. There are twelve pins in the cell for internal radial, axial, and temperature measurements.

An O-ring system was put into both the top plate and bottom plate to seal the cell and prevent cell fluid from leaking. As the assembly is tightened, the O-rings are compressed against the cell. Another six O-rings are used to seal the sample inside of the membrane. A locking pin was used to connect the cell body and the static load cell for axial loading measurement. Pore pressure and cell pressure can be applied through the upper platen and lower end cap.

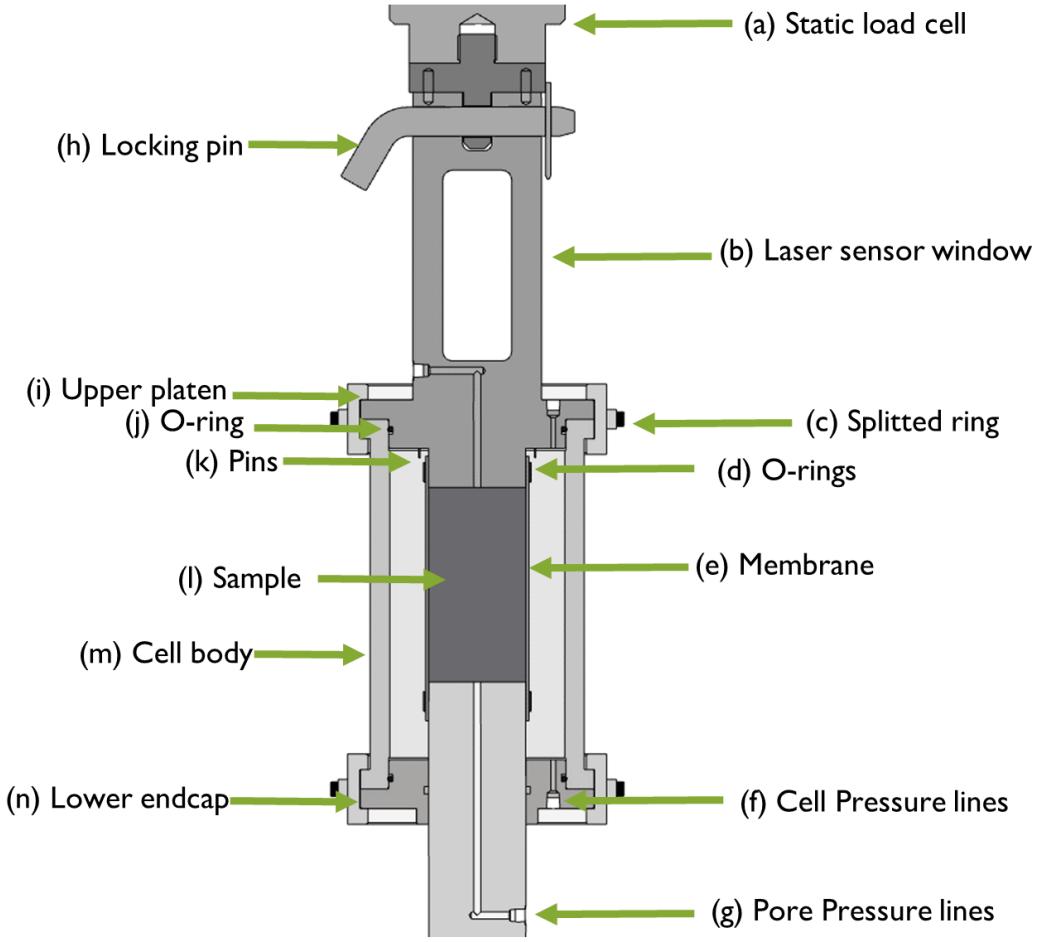

Figure 5-2 Schematics of the triaxial cell. Indicated on the drawing are: (a) static load cell; (b) laser sensor window; (c) split ring; (d) O-rings; (e) membrane; (f) cell pressure lines; (g) pore pressure lines; (h) locking pin; (i) upper platen; (j) O-ring; (k) pins; (l) sample; (m) cell body; (n) lower end cap.

5.3.2 Trust nut system

The thrust nut system (Figure 5-3) was used to apply axial stress on the specimen and protect the low-capacity dynamic load cell. The thrust nut system is sitting on the MTS system with four-cylinder standoffs that support and isolate the axial stress from the system. The greased internal bearing system can increase axial stress on the specimen by turning the split trust nut with an extension bar. The split trust nuts are tightened using split trust nut locators. The ram goes up 0.53 mm with ¼ turn of the bearing system. During the test, the actuator attaches to the bottom of the ram. An additional dynamic mini-load will be applied to the specimen with axial stress acting on the specimen.

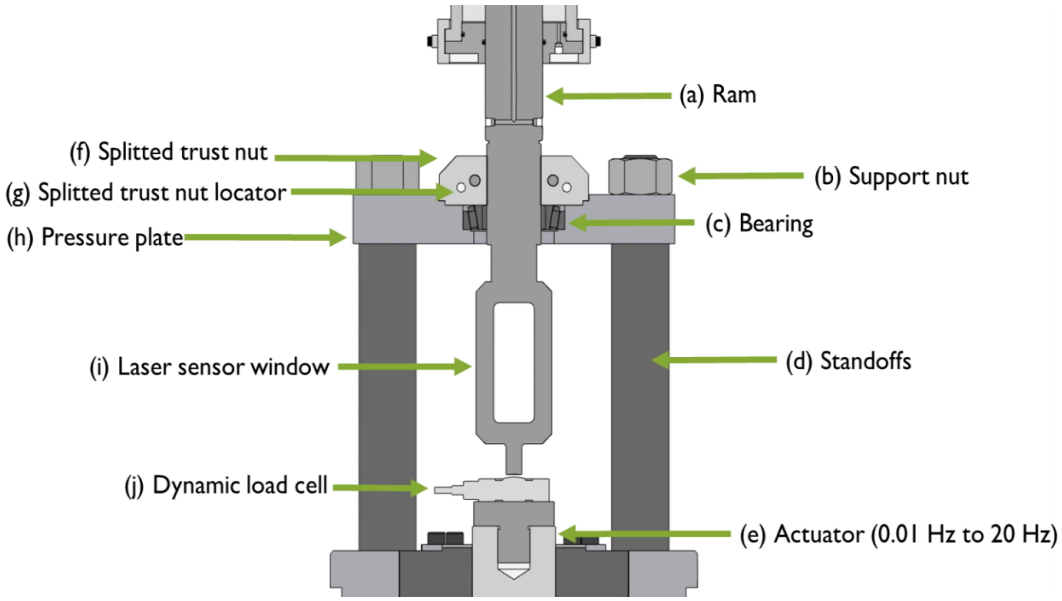

Figure 5-3 Schematics of the triaxial cell. Indicated on the drawing are: (a) ram; (b) support nut; (c) bearing; (d) standoffs; (e) actuator; (f) split trust nut; (g) split trust nut locator; (h) pressure plate; (i) laser sensor window; (j) dynamic load cell.

5.3.3 Servo-hydraulic load cell with laser sensors

The main component of the experimental apparatus is a computer-controlled servo-hydraulic system consisting of a hydraulic power unit and manifold that can deliver up to 250 kN of axial force (Figure 5-4). The static load cell forms part of the system and is used to measure the axial force with 2 N sensitivity. The bottom actuator can induce small strains on the sample at seismic frequencies from 10 mHz to 20 Hz. The actuator is controlled by feedback proportional signals from either the load cell for force control or from the linear variable differential transformer (LVDT) below the actuator for displacement control.

The displacement control mode applies actuator cyclic movement with 1.0 μm precision. The system has been customized to apply force to the load cell through a retainer/displacement nut system. This system allows for large forces to be applied to the specimen, isolating the more accurate dynamic load cell for precise force measurements during dynamic testing. The displacement of the specimen is measured by a pair of laser-based displacement sensors. These sensors are inserted into pockets on the top and bottom of the axial ram, in line with the specimen. The resolution of the laser displacement is 5 nm with a 392 kHz sampling rate, both excellent for

laboratory-based seismic frequencies measurement. These two sensor windows were cut into the ram to ensure the laser displacement sensors measured directly inline the vertical axis of the system. The sensor windows were designed to have cross-sectional areas equal to the ram to ensure there is no differential deformation throughout the ram. These windows increased the accuracy and repeatability of the elastic properties data by reducing miscentering of the axial force measurement. An LVDT was attached to measure the large-scale axial displacement of the specimen during static loading independently.

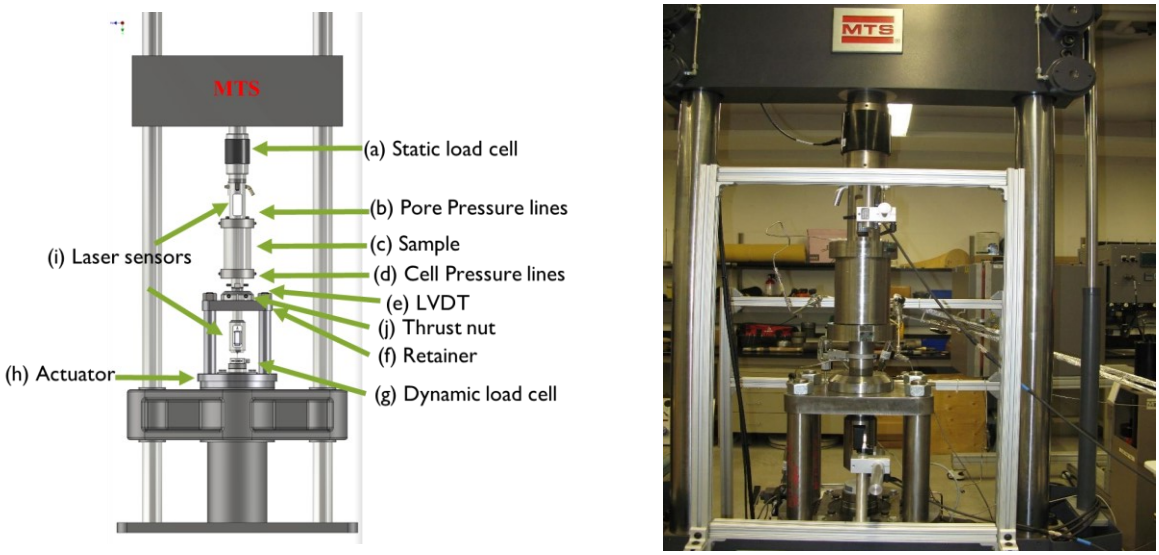

Figure 5-4 Schematics of the experimental setup based on a load cell. Indicated on the drawing are: (a) axial load cell for static axial stress measurements; (b) pore pressure lines; (c) sample with 63.5 mm in diameter by 127 mm in length; (d) confining pressure fluid line; (e) LVDT for axial displacement measurement; (f) retainer to apply the axial stress manually; (g) dynamic 5kN load cell with high sensitivity and seismic frequencies acquisition rates; (h) actuator to generate the dynamic loading at seismic frequencies (0.1 Hz to 20 Hz); (i) nanometer-scale laser displacement sensors; (j)thrust nut to apply static load.

To install the specimen for testing, a pore stone is placed on the lower ram and the specimen is placed on top of the pore stone. A pore stone is placed on top of the specimen and a membrane surrounding the specimen is sealed against the rams to provide separation between confining pressure and specimen pore pressure, as improper jacketing can lead to erroneous results (Gardner et al., 1964; Dunn 1987; Mörig and Burkhardt 18l9; Subramaniyan et al., 2014). The top cell cap is carefully slid over the ram followed by sealing of the cell body at the top and bottom with split rings. The cell pressure and top and bottom pore pressure lines are connected, and the cell is filled with silicon oil. The configuration of the ram and cell body allows for independent application of vertical stress through the axial ram, radial stress through cell pressure, and pore pressure gradient

through the top and bottom flow ports. The cell has a 40 MPa capacity fluid pressure capacity applied by pumps. The top pore pressure and bottom pore pressure are connected to pumps allowing the application of differential pressures for permeability measurements, or constant pressure for consolidation and Biot's coefficient measurements. The pressure sensors connected to the system are FPG models with +/- 0.10% accuracy. The applied confining pressure, top and bottom pore pressures, axial displacements, differential pressure, cell and room temperature, and pump data are each logged at 5-second increments using a custom-built logging software system. The schematic of the seismic dynamic measurement system is in Figure 5-5.

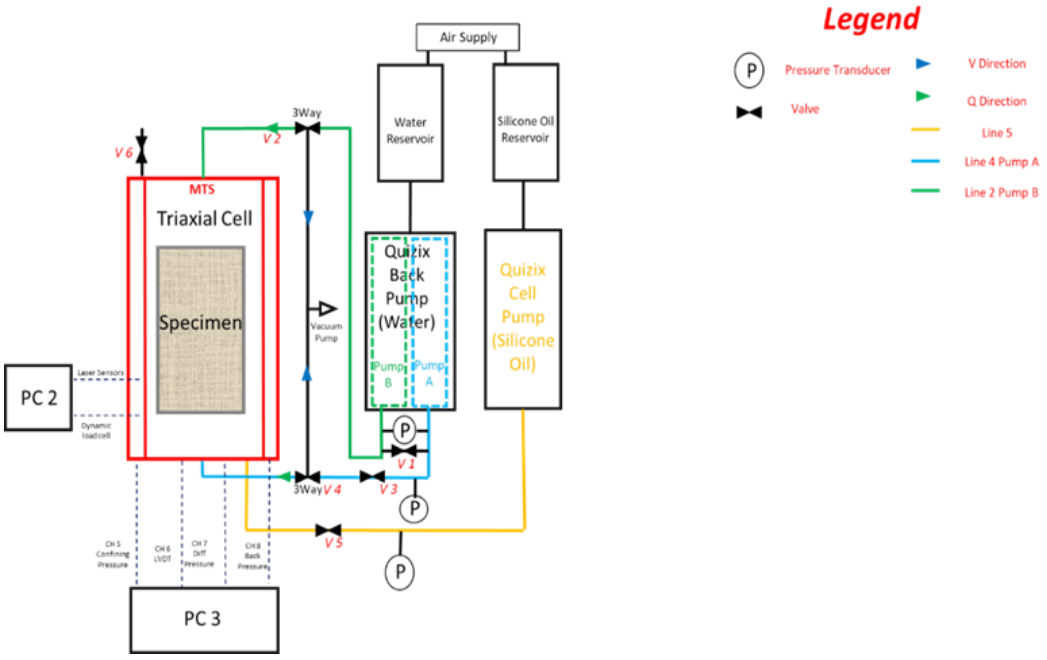

Figure 5-5 Schematic of the seismic dynamic measurement system.

Once the sample is loaded into the system, the axial stress is loaded through the thrust nut (Figure 5-4) threaded onto the ram, which reacts with the retainer. The applied load, cell pressure, and pore pressure are then increased, following the desired axial and radial stress and the pore pressure path. Once the specimen reaches the desired stress/pressure state, the sample is held for a short period. A small amount of heat is generated from turning the thrust nut, causing an increase in axial stress (10-200N). The system must be allowed to come back to equilibrium prior to dynamic load application. After system equilibrium, the dynamic seismic frequency loading is applied through the actuator and measured with the 5kN dynamic load cell.

Due to the nature of adding force from the dual thrust nut actuator system, a 22kN load cell was first used to prove that the two separated load cells could measure the appropriate forces. The testing sequence used an aluminum specimen and was executed by first applying a preload force through the thrust nut and then applying an additional displacement-controlled load with the actuator. The preload was added in increments of 5 kN from 0 kN to 60 kN. In Figure 5-6, the difference between the static load cell and the dynamic load cell shows a linear increase at every initial preload. The results show that the retainer can protect the low capacity dynamic load cell efficiently over small axial displacements (<0.01mm) and small incremental forces (200-500N).

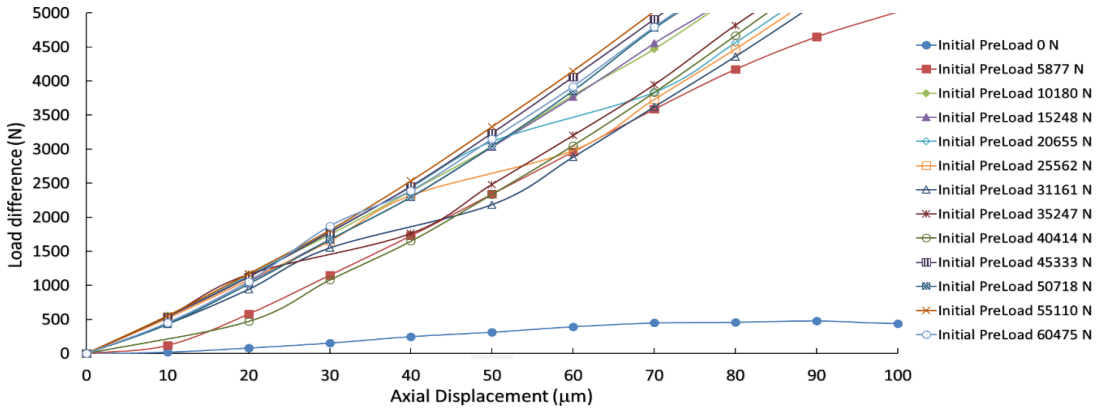

Figure 5-6 Safety trials for the dual load cell setup with several initial preload.

The system has been tested for axial force loading up to 150 kN with 100 N or less dynamic loading. The performance of the system was tested from 0.01 to 20Hz and shows it is adequate for required investigations of dynamic modulus at laboratory scale (Figure 5-7).

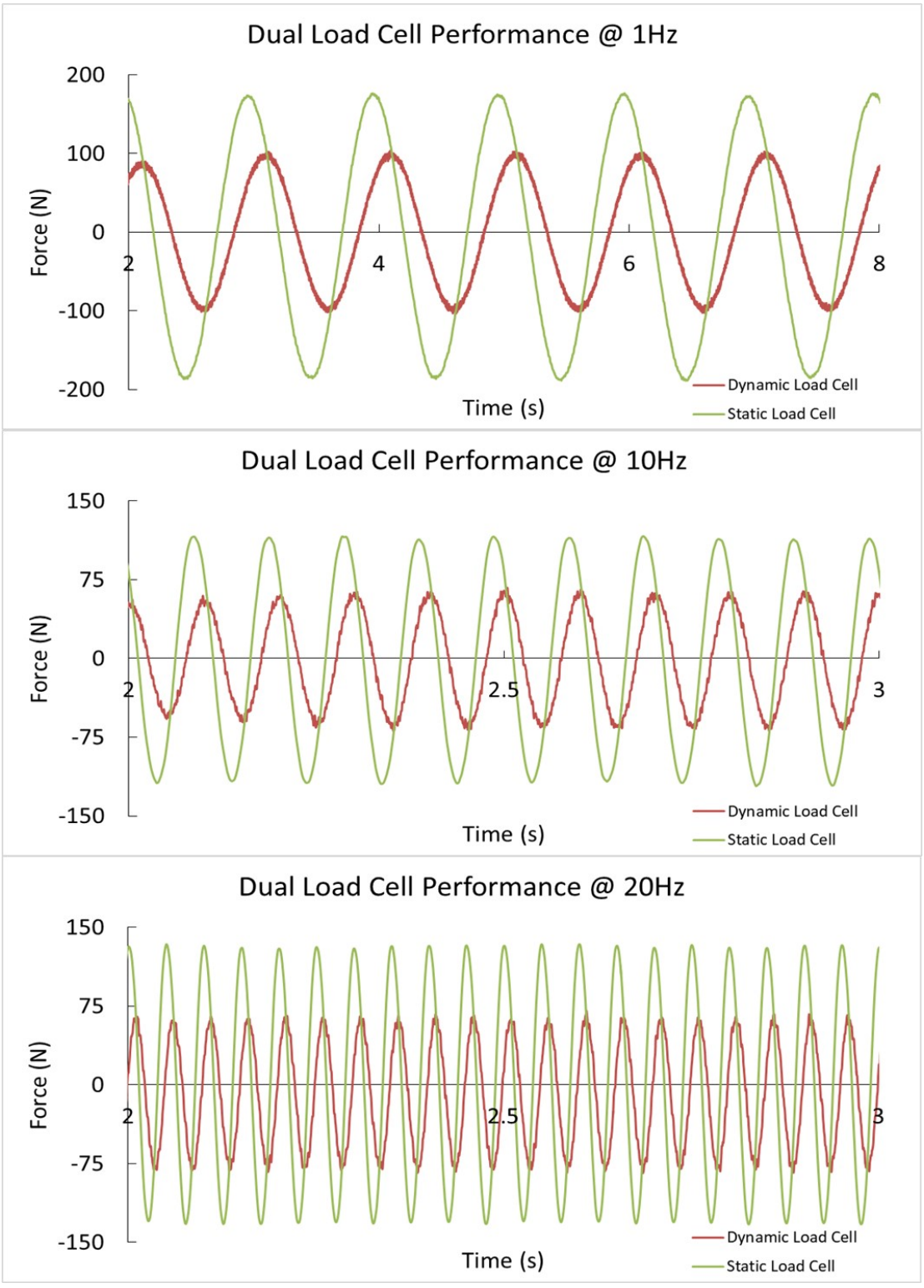

Figure 5-7. Measured loading amplitude with the dual load cell. Three plots show the static load cell and dynamic load cell performance at 1 Hz, 10Hz, and 20 Hz.

5.4 Calibration sample and 3D printer sample

A poly [methyl methacrylate] PMMA (acrylic) sample was chosen for the calibration sample because of its isotropic and homogeneous composition, well-known elastic properties, and negligible porosity. Therefore, the elastic properties will not change during dynamic triaxial tests. Acrylic is a viscoelastic material with frequency-dependent elastic properties, so it has been widely used for the calibration of new apparatuses. The cylindrical acrylic specimen used in this study had a diameter of 63.5 mm and a length of 127 mm.

3D printed sandstone was also tested. The 3D printed samples use the Binder Jetting technology (Ex-One 2014) located in GeoPrint at the University of Alberta. Primkulov et al., (2017) and Gomez et al., (2017) provided a detailed description of the printing process used for the sandstone analogs. The specimens were built using a 20% PFA saturation (~4% of the bulk volume), 0° layer orientation (layers vertical to load application) and a layer thickness of 250 μm. The cylindrical specimen used in this study was 63.5 mm in diameter and 127 mm in length. Figure 5-8 shows a scanning electron microscopy image of the material's grain structure. The porosity of the 3D printed sample was 35.7%, permeability was 1200mD, and the particle size distribution of D10, D50, and D90 was 110, 175, and 220 μm, respectively (Osinga et al., 2015).

5.5 Experimental Results and Discussion

The acrylic specimen is placed in the triaxial cell and Young's modulus is measured with no radial stress and pore pressure of zero. From the load frame control panel, dynamic displacement loading induces a sinusoidal microstrain with frequencies from 0.1 Hz to 20 Hz at each stress stage. All data from the load cells, laser displacement sensors, and LVDTs are logged, and Young's modulus can be calculated based on equations (Figure 5-9). The results show agreement with other seismic frequency testing and prove that the system provides stable results (Koppelmann, 1958; Spencer, 1981; Yee and Takemori, 1982; Batzle et al., 2006; Nakagawa, 2011; Takei et al., 2011; Tisato et al., 2012; Madonna and Tisato, 2013). It was noticed that Young's modulus increased significantly when the frequency went to 10 Hz. This large increase is attributed to servo-hydraulic control of the actuator -the proportional gain value decreased as the frequencies increased. A low proportional gain makes the system slow to respond; however, the force control feedback

controller can drive the actuator to required loading. The advantage of the servo-hydraulic actuator is that there is a higher load rating and acceleration when compared to the piezoelectric actuator technique. The results from testing are stable, repeatable, and in agreement with the previous testing, the results proved the performance suitability of the seismic frequencies testing system.

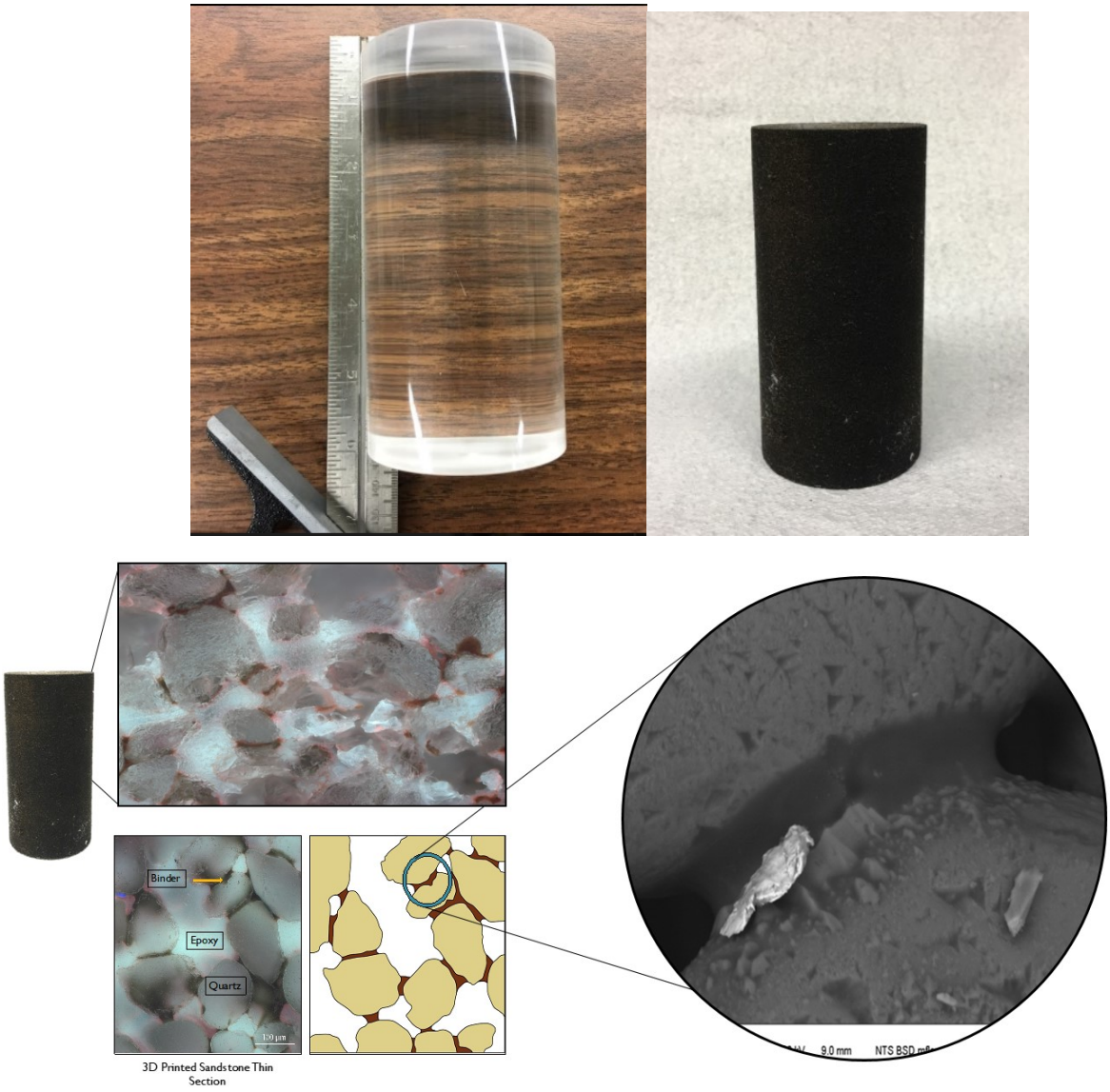

Figure 5-8 The acrylic and 3D printed specimens used for calibration and testing. The 3D printed specimen image was obtained on a polished section of a UV-fluorescent polymer saturated sample. Binding resin shows as dark spots between the grains (modified from (Hodder et al. 2018)).

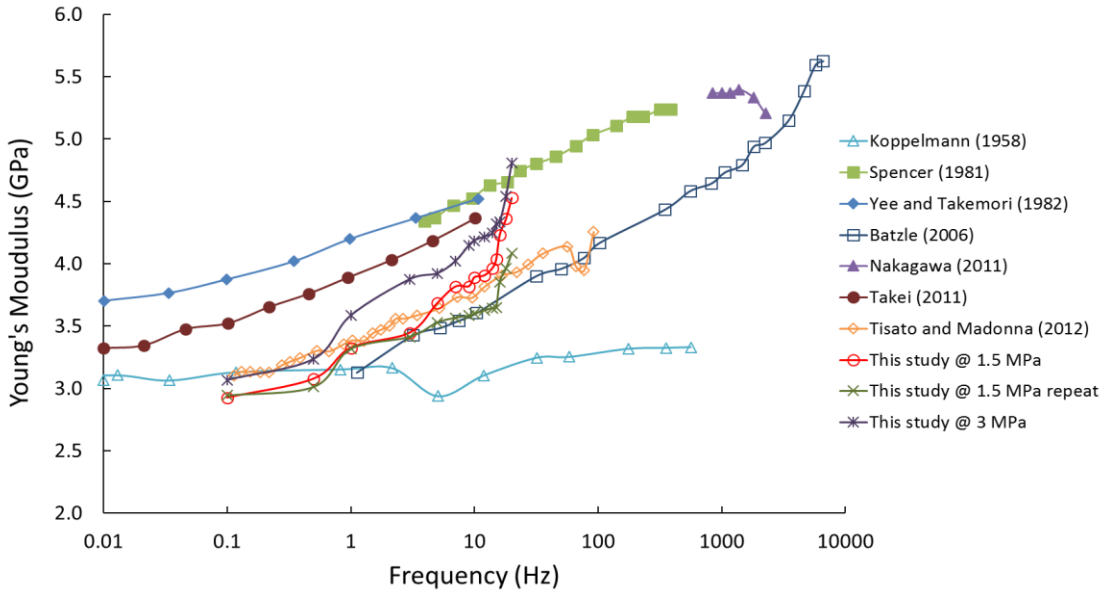

Figure 5-9 Young's modulus of acrylic measured at seismic frequencies under different axial stress (1.5 MPa and 3 MPa).

The second experiment was performed using 3D printed samples under water saturation conditions with variable axial stresses. The axial stress and confining pressure were incrementally increased to 1000 kPa with a pore pressure of 500 kPa. For the first test, the axial stress was increased to 1500 kPa and the dynamic test was executed using the same procedures as the acrylic specimen. Upon completion of the dynamic test, the axial stress was raised to 3000 kPa and the dynamic testing was repeated. Figure 5-10 shows that Young's modulus increased with the axial stress, increasing only slightly with an increase in frequency (7-10%); a negligible attenuation was observed in the results. The results of the 3D printed specimen were compared with other published data (Spencer, 1981; Madonna and Tisato, 2013; Mikhaltsevitch et al., 2014a; Subramaniyan et al., 2015; Spencer and Shine, 2016). Subramaniyan et al. (2015) conducted the tests with 100% water saturation in Fontainebleau sandstone under an isotropic stress field of 5000 kPa. Based on results from Madonna and Tisato (2013) and Mikhaltsevitch et al. (2014b), the confining pressure has a significant effect on Young's modulus. For the same water saturation, Young's modulus of Berea sandstone exhibits a 60% increase from 16 MPa to 26 MPa. The 3D printed specimens exhibited softer behaviour than the sandstones due to several factors still under investigation. The accuracy and reproducibility of Young's modulus data have shown that the seismic frequencies system has the capacity to obtain Young's modulus at seismic frequencies under deviatoric stress.

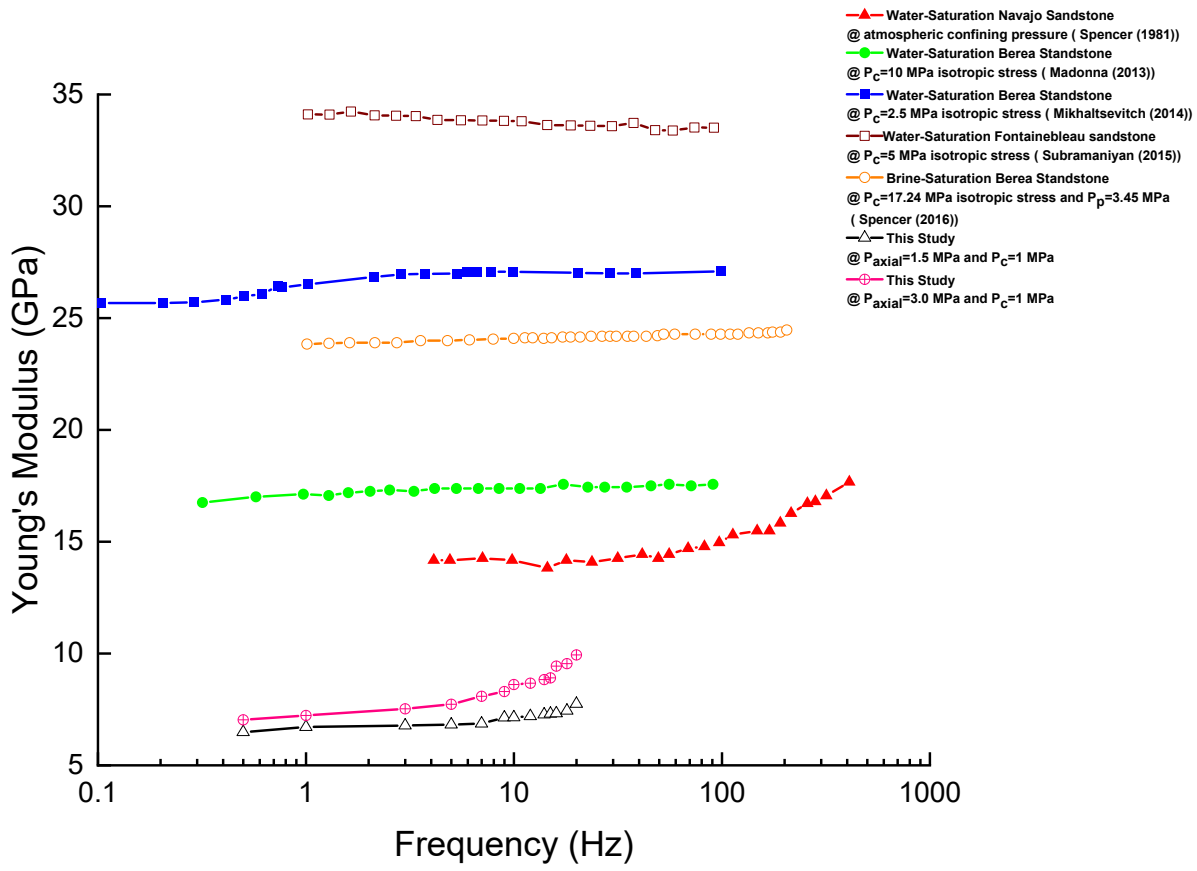

Figure 5-10 Young's modulus of 3D printed and natural sandstone specimens measured at seismic frequencies under variable stress conditions.

5.5 **Conclusion**

This chapter presents an innovative triaxial seismic frequencies testing system that has been proven in the range from 0.01 to 20Hz and nanometer-scale accuracy, axial stress up to 150 kN, and radial and pore pressures up to 40 MPa. The unique cell design can measure the static and dynamic properties under simulated reservoir conditions. Calibration test results for acrylic and 3D printed samples indicate the stability and repeatability of the system that compares well with published data. Ongoing research is focused on obtaining seismic frequency properties of poorly consolidated oil sands. The data can be used for forward modelling using reservoir geomechanical simulations to assess whether improvements in "a priori" predictions of fluid saturations and steam chamber development are altered.

6 EXPERIMENTAL INVESTIGATION OF THE DYNAMIC PROPERTIES OF DENSE SAND SAMPLES

6.1 **Abstract**

In order to investigate the seismic geomechanical responses of dense sands formation in Alberta, Canada during different stress and loading conditions, reconstituted dense sand samples were prepared from unconsolidated sand using a modified technique developed at the University of Alberta (Manual of Artificial Oil Sand Sample Preparation, 2001). The core specimen preparation consists of five successive stages: sand packing, sand densification, fluid saturation, specimen freezing, and specimen extraction. The process can reconstitute high-quality specimens with a 63.5 mm (2.5 inches) diameter and a 127.0 mm (5.0 inch) height. Both water saturation and bitumen saturation can be obtained using this setup. The detailed preparation procedure is shown in the following sections.

After preparing three dense sand specimens, experiments were conducted using the aforementioned test procedure. The triaxial compression test was performed at different effective stress states of 0.5 MPa, 1.5 MPa and 3.0 MPa to measure the stress-strain behaviour of the dense sand specimens at different levels of effective confining stress. At each stress level, dynamic properties were collected at different frequencies (0.01Hz to 20Hz). Permeability tests were performed under the steady-state method before and after the experiment.

6.2 **Dense Sand Sample Preparation**

6.2.1 Sand Packing and sand densification for a Synthetic Core

Preparation of samples was conducted by following the Manual of Artificial Oil Sand Sample Preparation, 2001, a test procedure guide that was developed and tested by the Geotechnical Center at the University of Alberta. First, 1500g of dry sand from Fort McMurray is prepared and its mass recorded. The sand is submerged in deionized (DI) water that has been boiled for at least 30 minutes. These steps remove organic impurities from the sand surface, improving the water

saturation of the rock. Two porous stones should also be placed in DI water and boiled for at least 30 minutes, removed, and allowed to cool down.

Second, the base cell is mounted on the vibrating table. DI water is poured into the cell and end cap lines are saturated with water. Sand and water are slowly and continuously poured into the cylinder to a depth of 1cm. The vibrating table is turned on to the speed of 5 and additional axial stress is applied to the surface through an aluminum rod. This step is repeated until the sand level is close to the cylinder mouth. It will take 2 or 3 hours to finish sand densification.

The third step is to place the second 2½″ porous stone on the surface of the sand and close the assembly with the top end cap. The edge of the cylinder should nearly touch the shoulder of the top cap. The last step is to bolts in both the top and bottom caps and fasten the cell with nuts. The above steps are used to prepare highly uniform specimens while avoiding any air bubbles inside.

6.2.2 Fluid Saturation in a Synthetic Core

First, CO_2 is injected through a tank with 4000 Psi capacity. CO_2 is used because it dissolves in water more easily than air. A pressure gauge is used to monitor the pressure. A Vacuum Pump is used to vacuum the whole system.

After the sand packing cell is vacuumed, it needs to be flushed with brine. Before the test, the brine cylinder needs to be checked to ensure there is enough brine for saturation. Once the air pressure and all the lines are connected, the regulator is adjusted to make sure pressure of 100 Psi is supplied and monitored until the brine outlet is saturated. The brine outlet is connected to the sand pack assembly and water is collected from the open-top valve of the sand pack assembly. Once the volume of water collected is equivalent to 2-3 pore volumes is the Quizix pump is stopped, all valves in the sand pack assembly are closed, and the brine outlet is disconnected.

Remaining lines are disconnected, and the entire assembly is placed in a freezing box with dry ice for at least 30 min. After freezing, the mould is removed, and the sample is extracted.

Oil sand core is cut to the desired length required for testing. If there are significant surface imperfections, and/or dimensional requirements imposed by the testing apparatus, surface

finishing may be required on the circumference of the core. The ends are machined flat and perpendicular to one another.

6.3 **Triaxial Test Procedure**

The synthetic specimen is to be tested in the newly developed triaxial cell following the test procedure mimicking in-situ reservoir pore pressure, temperature, and stress state. Tests are conducted under isotropic stress conditions.

Detailed procedure of installing the setup and conducting an isotropically consolidated triaxial compression test at seismic frequencies can be found in Appendix A-G. The procedures are unique and significantly different from conventional triaxial testing as the triaxial tests are conducted at different frequencies. The installation steps are modified based on the testing conditions. In order to keep the sample frozen to minimize core damage, the installation must be finished within 20 minutes. Fine adjustment devices and vibration pads are used to eliminate the vibrations. To achieve the saturation assessment, a B-test is performed. Isotropic consolidation is conducted before testing. Isotropic consolidation is employed to establish the initial reservoir stress conditions within the specimen. Dynamic testing is conducted with the increasing axial load for deviatoric stress. The frequency for dynamic testing is from 0.1Hz to 20Hz. At last, a constant pressure/head permeability test is conducted to obtain permeability at different stress conditions.

In the triaxial compression testing, axial stress was increased at a constant rate until failure was reached within the specimen. To ensure no additional pore pressure developed during the shearing, all triaxial compression tests are conducted under drained conditions. However, to ensure stability and mimic the same condition as the wave travelling in the specimen, dynamic testing is conducted under undrained conditions. Once the testing has achieved the final level of axial strain, the triaxial cell is disassembled and made ready for further testing.

6.4 **Stress-strain curve of synthetic dense sand**

The B value is determined to make sure the specimen is fully saturated. The B value is the ratio $\frac{\Delta u}{\Delta \sigma}$ which relates the excess pore pressure to corresponding increment deviatoric stress under the undrained conditions of the triaxial tests. Figure 6.1 shows the measurements of B value at the effective stress states of 0.5 MPa, 1.5 MPa, and 3.5 MPa. The slopes of the curve are all above 0.96, which means that the condition of nearly full saturation was achieved along the length of the specimen.

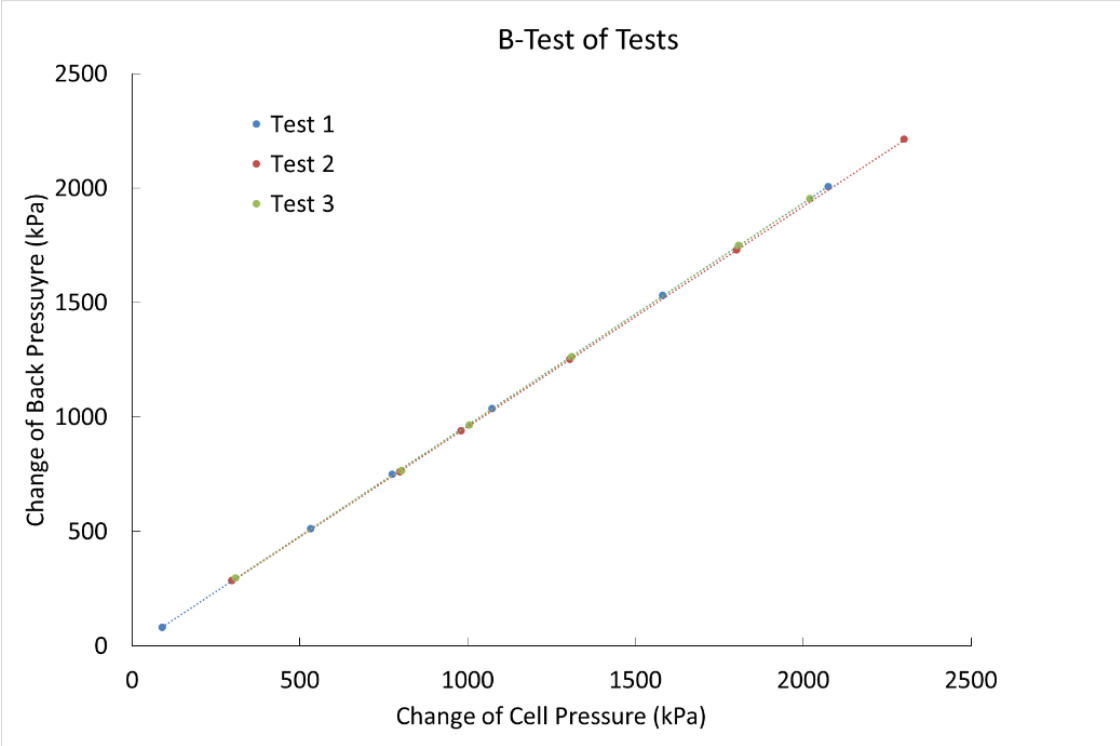

Figure 6-1 B-Test after the core specimen thawed overnight in the triaxial cell at 500, 1500, 3500 kPa effective stress, respectively

Figure 6.2 shows the relationship between the deviatoric stress (kPa) and axial strain (%) under different confined pressure conditions. Both the peak and the residual values show in the figure, which is classic behaviour for the dense sand specimen. The deviatoric stress at failure increased with increasing effective stress. The deviatoric stress reaches the peak value of 2425 kPa at axial strain around 3.00% under the effective stress of 500 kPa. The deviatoric stress increases to 6100

kPa and 9120 kPa at axial strain around 3.75% and 4.75%under the effective stress of 1500 kPa and 3500 kPa, respectively. Young's modulus values of 0.68 MPa, 1.3 MPa, and 1.43 MPa were obtained at an axial strain of 0.1% for effective confining stresses of 0.5 MPa, 0.5 MPa, and 3.5 MPa respectively, indicating that there is an increase in the degree of stiffness of the core sample as confining stress increases.

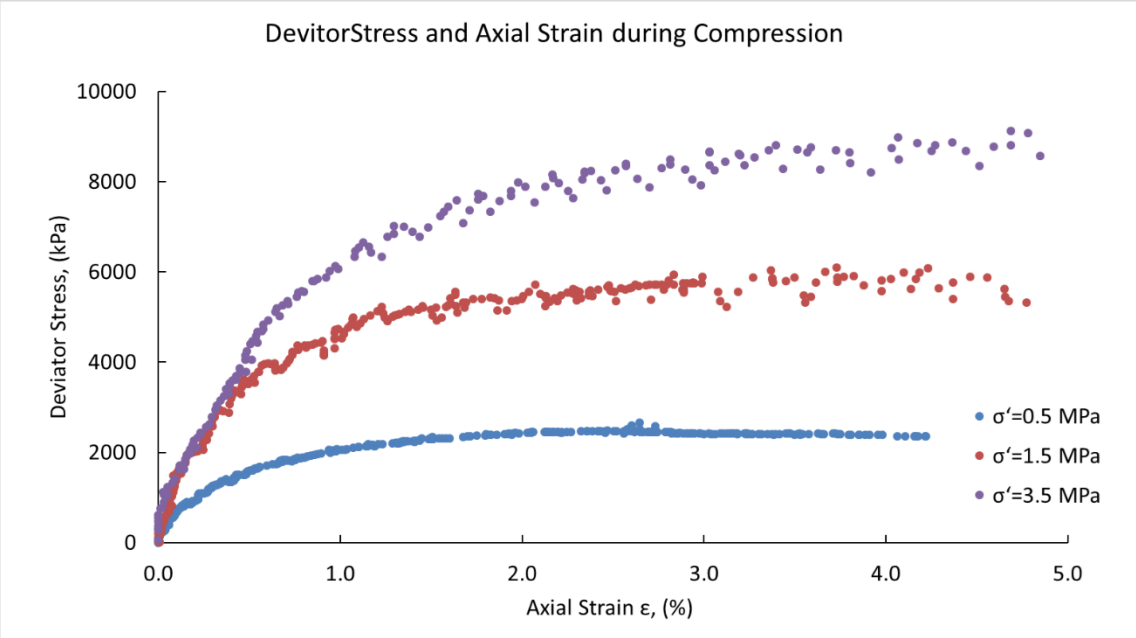

Figure 6-2 Deviatoric Stress variation (kPa) vs. Axial Strain (%) for test specimen in the triaxial cell at 500, 1500, 3500 kPa effective stress, respectively.

Figure 6.3 shows the relationship between the volumetric strain (%) and axial strain (%) under different confined pressure conditions. It is also a classic expected volumetric behaviour for the dense sand specimen. The volume of the specimen is reduced at the beginning of the loading stage followed by a substantial dilation with deviatoric stress increments. At the beginning of the loading stage, the pore volume decreased, and micro-cracks closed. The volumetric strain then increased, and the sand specimen behaved with dilation due to the induced shear distortion. The behaviour of the dilation approach is much quicker at lower effective pressure.

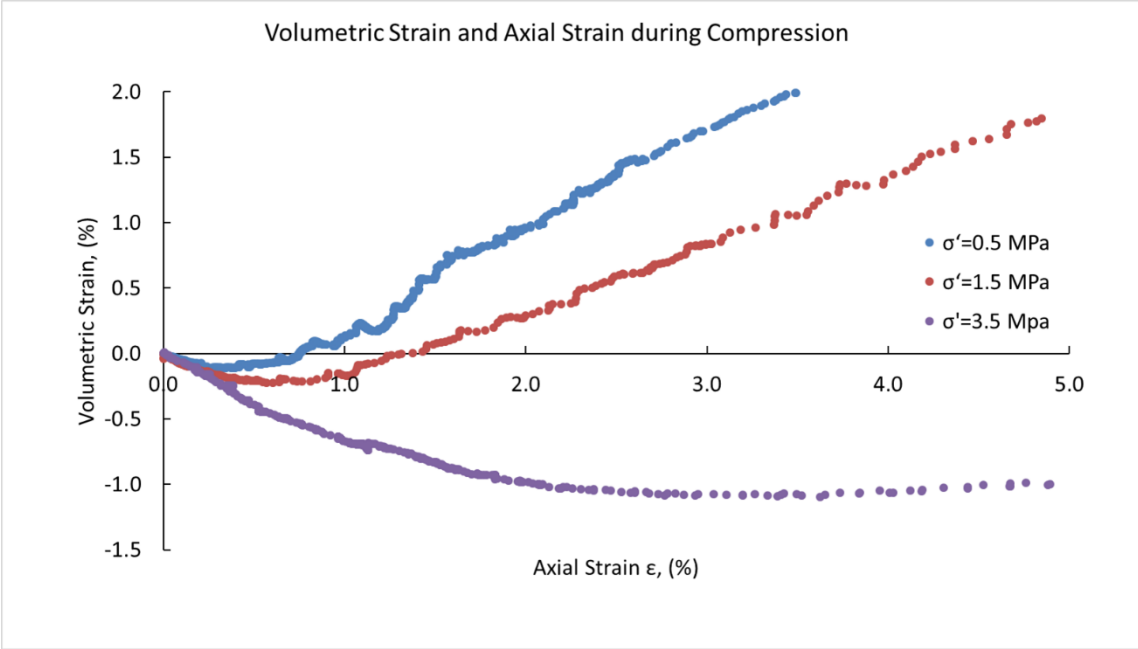

Figure 6-3 The pattern of Volumetric Strain variation (%) vs. Axial Strain (%) at 500, 1500, 3500 kPa of effective stress, respectively, during a shearing test on sands specimens.

Figure 6.4 shows the stress path of each of the three test dense sand specimens, where they are plotted in the t-s' stress field. The variables t is equal to half of the deviatoric stress, and s' is equal to the medium stress between maximum and minimum effective stresses, as defined by equations 6- 1 and 6- 2:

$$s' = \frac{(\sigma_1' + \sigma_3')}{2} \qquad 6\text{- }1$$

$$t = \frac{(\sigma_1' - \sigma_3')}{2} \qquad 6\text{- }2$$

where σ_1' is the effective axial stress and σ_3' is the effective confining stress.

The friction angle $\emptyset'$ can be calculated by determining the slope of a line connecting the peak of each stress path since c' is equal to 0 (the dense sand specimen is a cohesionless material.). Therefore, from the equation 6- 3:

$$tan\,(\alpha) = sin\,(\emptyset') \qquad 6\text{- }3$$

where α is the slope of the line of peak strength points of stress path and $\emptyset'$ is the effective stress friction angle.

The slope of the t-s' curve is 0.57. So, the frictional angle ($\emptyset'$) is 34.75° for the dense sand specimens used in this research.

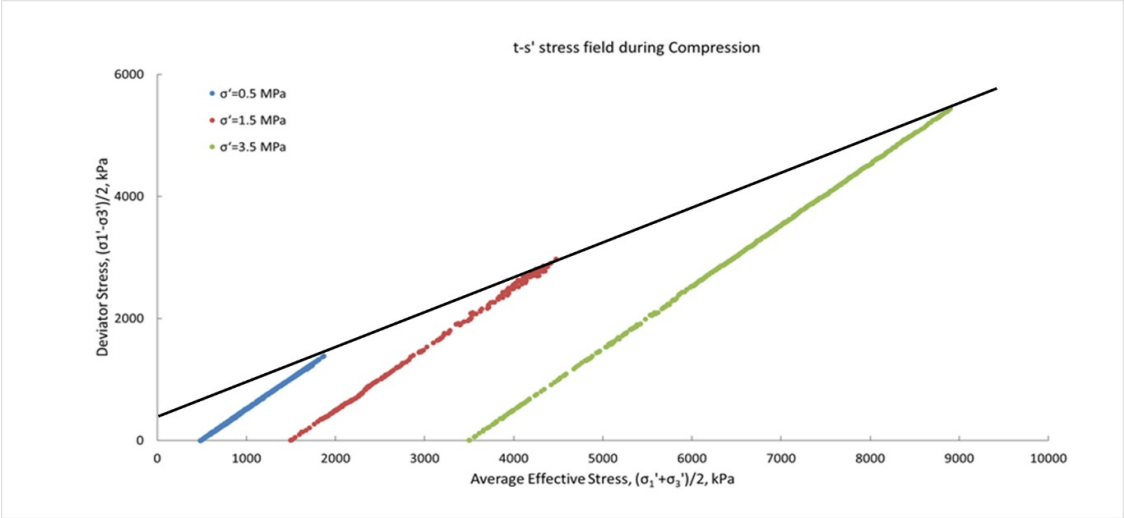

Figure 6-4 Triaxial Test – t vs. s' during Compression for the test specimen.

Young's modulus and Poisson's ratio were also measured after the compression tests. Young's modulus defines the relationship between axial stress and axial strain in the dense sand specimen in the linear elasticity regime. It was determined by calculating the slope of a line drawn from the initial point of the stress-strain diagram and intersecting the curve at the point of 0.25% axial strain. The ratio of the lateral strain to axial strain is referred to as Poisson's ratio of the material. It was determined by the linear fit to the radial strain versus axial strain curves for the range of axial strains from 0 to 0.25 %. The table is a summary of all the stiffness parameters for each dense sand specimen under three effective confining pressure: 0.5 MPa, 1.5 MPa and 3.5 MPa. Young's modulus values of 0.33 MPa, 0.65 MPa, and 0.75 MPa were obtained for effective confining stresses of 0.5 MPa, 1.5 MPa and 3.5 MPa, respectively, indicating that there is an increase in the degree of stiffness of the dense sand sample as confining stress increases.

In order to prove the stability of the entire system and to cross-check the properties of synthetic sand, triaxial results are compared with previous results by using the conventional experimental setups in our research group. The conventional experimental results from Wang (2020), Kais (2013) and Mohamed (2012) by using dense sand specimens under different effective confining pressures. From Figure 6.5 and Figure 6.6, classic dense sand behaviour is almost the same for every experimental result using dense sand specimens. Stiffness parameters proved to have similar properties to the dense sand specimen and the stability of the system. Dense sand specimens showed higher Young's modulus values with a higher peak strength stress. This is first attributed to the different dimensions of the dense sand specimen that might cause mechanical properties to vary. Secondly, the loading rate might affect the test result. Since this experimental setup is manually controlled, the loading rate is only 150 N/s at the beginning of the test and even less when it is up to 4% axial strain. Due to physics difficulties, turning the trust nut is extremely difficult, making it so that the loading rate cannot be controlled at the end of the test. Third, the procedure for synthetic dense sand samples is slightly different. To eliminate the impurity in the original Fort McMurray sand, the sand is boiled and filtered before making the synthetic dense sand sample. Finally, the temperature for conventional triaxial tests is 22 ℃ while the temperature for this new system is 19 ℃.

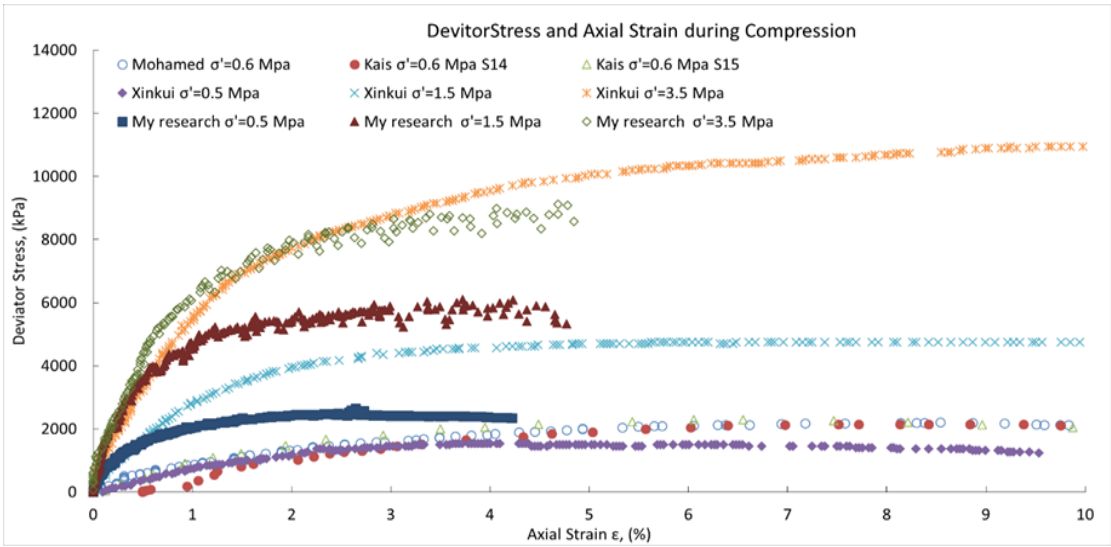

Figure 6-5 Deviatoric Stress variation (kPa) vs. Axial Strain (%) for test from Wang (2020), Kais (2013) and Mohamed (2012).

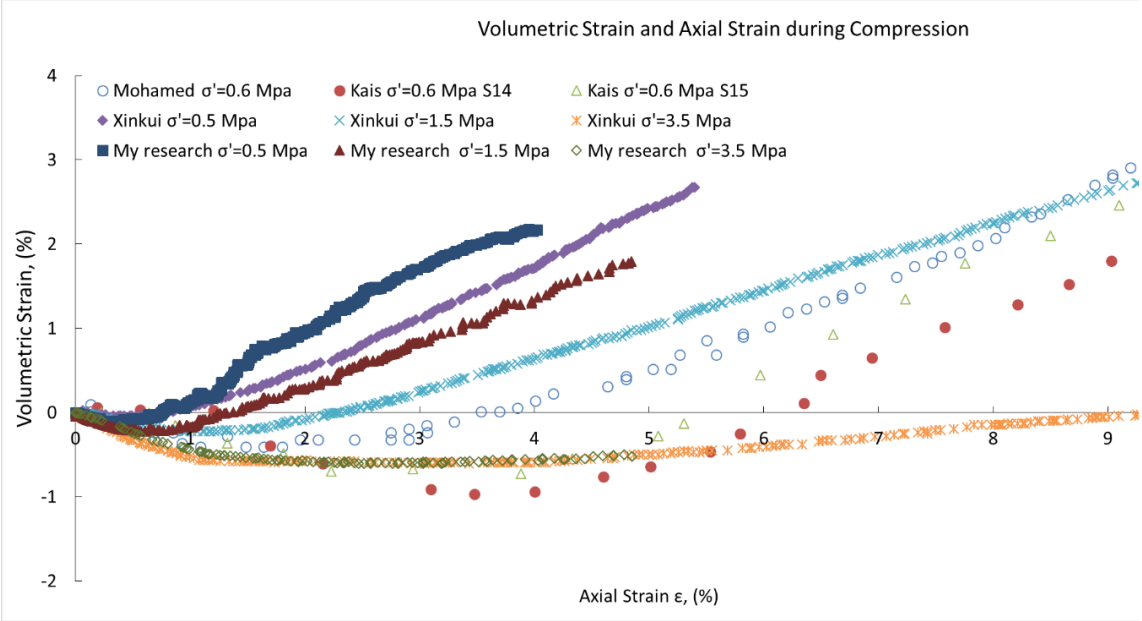

Figure 6-6 The pattern of Volumetric Strain variation (%) vs. Axial Strain (%) for test from Wang (2020), Kais (2013) and Mohamed (2012).

6.5 **Velocity Dispersion**

Figure 6.7, Figure 6.8, and Figure 6.9 show the relationship between static Young's modulus and dynamic Young's modulus at different effective pressure. The static Young's modulus increased in the very beginning, but it decreased with the axial stress increasing. This is the same as previous results and has been widely used for the current simulation. However, the dynamic Young's modulus increases as the axial stress increases. So, the difference between static Young's modulus and dynamic Young's modulus is much more significant when the sample approaches the failure point. For a test under 3.5 MPa effective stress, the dynamic Young's modulus is 7 times bigger than the static Young's modulus. Also, dynamic Young's modulus is always undrained, this also represents a potential difference between static and dynamic modulus since the static modulus is related to a drained deformation.

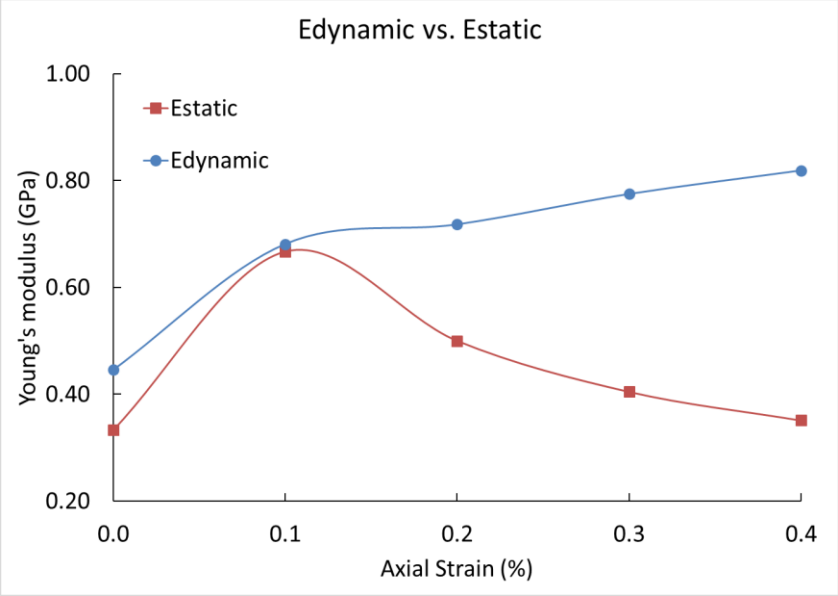

Figure 6-7 Static Young's modulus vs. dynamic Young's modulus at 0.5 MPa effective pressure.

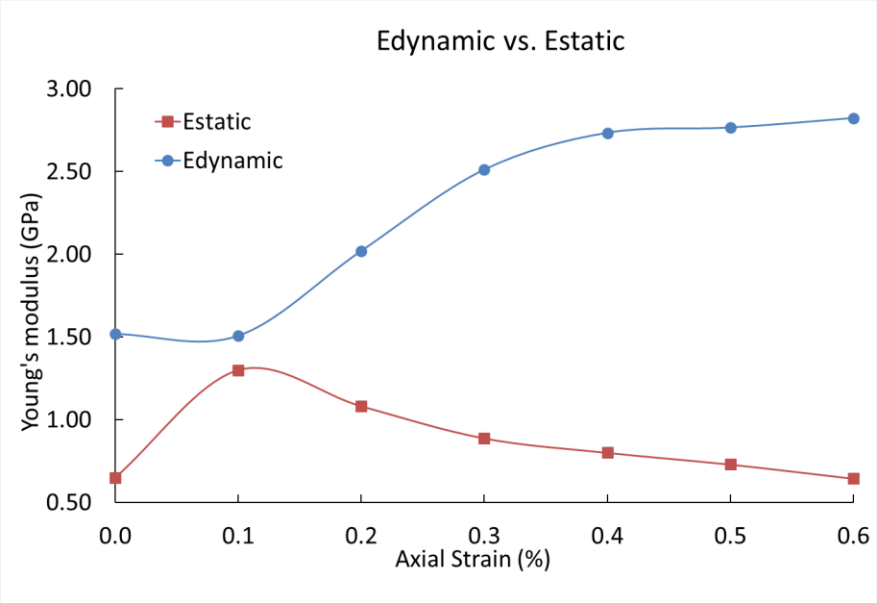

Figure 6-8 Static Young's modulus vs. dynamic Young's modulus at 1.5 MPa effective pressure.

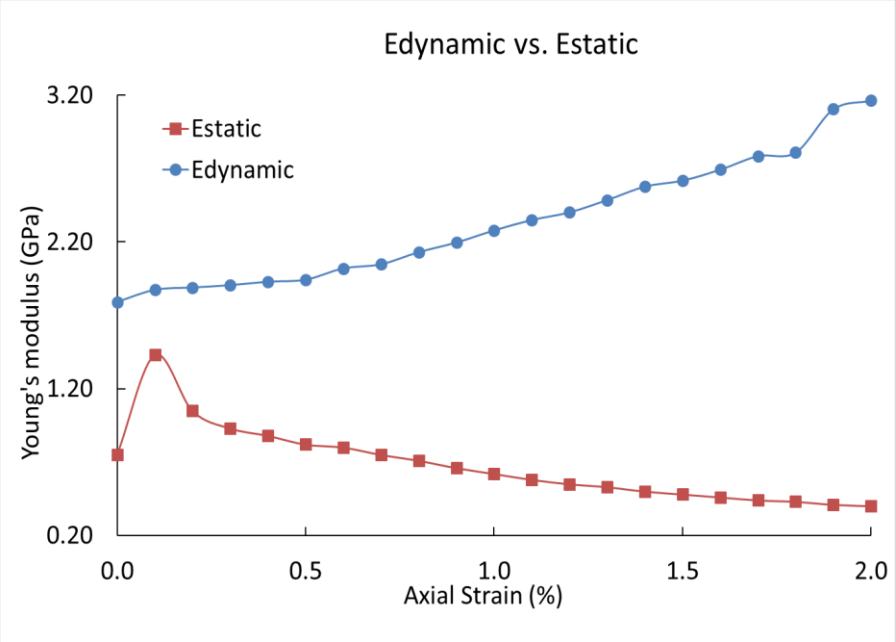

Figure 6-9 Static Young's modulus vs. dynamic Young's modulus at 3.5 MPa effective pressure.

Figure 6.10, Figure 6.11, and Figure 6.12 show the relationship between the dynamic Young's modulus and frequencies. Young's modulus is seen to increase slightly from 0.01 Hz to 20 Hz. The deformation induced by external stress causes pore pressure increment, then the fluid moves between nearby pores. For saturated samples at seismic frequencies, fluid has enough time to move but the sample becomes stiffer as the fluid does not have sufficient time to move at high frequencies. Thus, the dynamic Young's modulus increases as the frequencies increase. The dynamic Young's modulus at 0.1 % axial strain increases 57.14 % at 0.5 MPa while the dynamic Young's modulus increases 50.00 % and 41.25 % respectively at 1.5 MPa and 3.5 MPa. It can be concluded that the dynamic Young's modulus increase is sensitive to frequencies at lower effective pressure. The pore connection will be closed at high effective pressure, so the fluid has limited space to move, and the sample will become stiffer.

Results can also be expected to be sensitive to axial stress and effective pressure. During triaxial tests, the effective pressure changes (confining pressure minus pore pressure) the crack apertures. The distribution of fluid within the fracture network will change, causing changes in the rock stiffness and seismic velocities. The dynamic Young's modulus increases with increases of axial stress and effective pressure. At 0.5 MPa effective stress, the dynamic Young's modulus increases

over 150 % from 0 % axial strain to 0.4 % axial strain at 1 Hz. At 3.5 MPa effective stress, the dynamic Young's modulus increases only 30 % from 0 % axial strain to 0.4 % axial strain at 1 Hz. It is obvious that the dynamic Young's modulus is much more sensitive at lower axial stress and effective pressure.

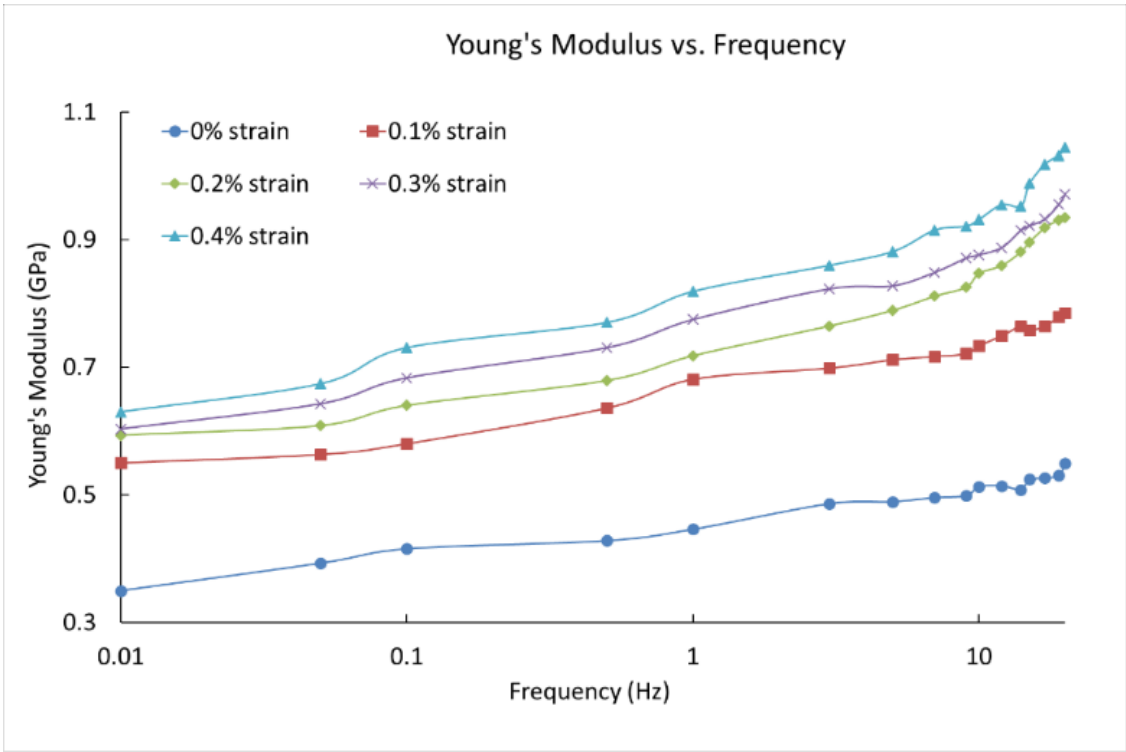

Figure 6-10 Dynamic Young's modulus vs. frequencies (0.01 Hz to 20 Hz) at 0.5 MPa effective pressure.

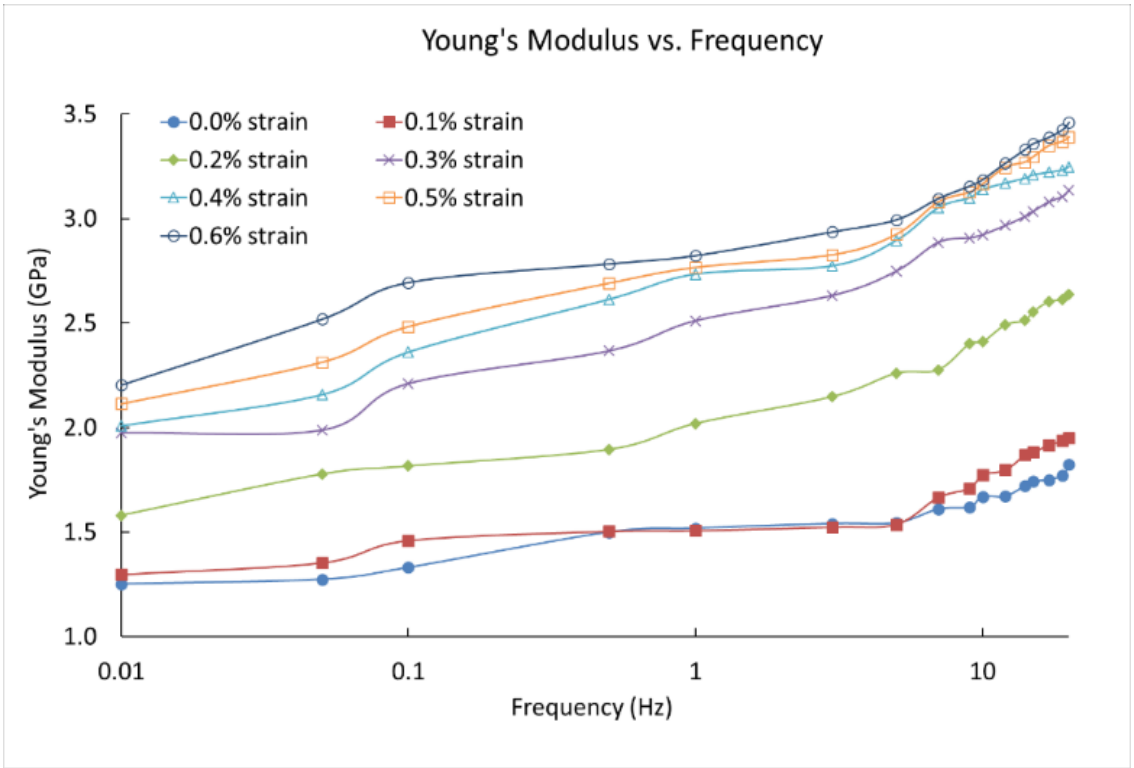

Figure 6-11 Dynamic Young's modulus vs. frequencies (0.01 Hz to 20 Hz) at 1.5 MPa effective pressure.

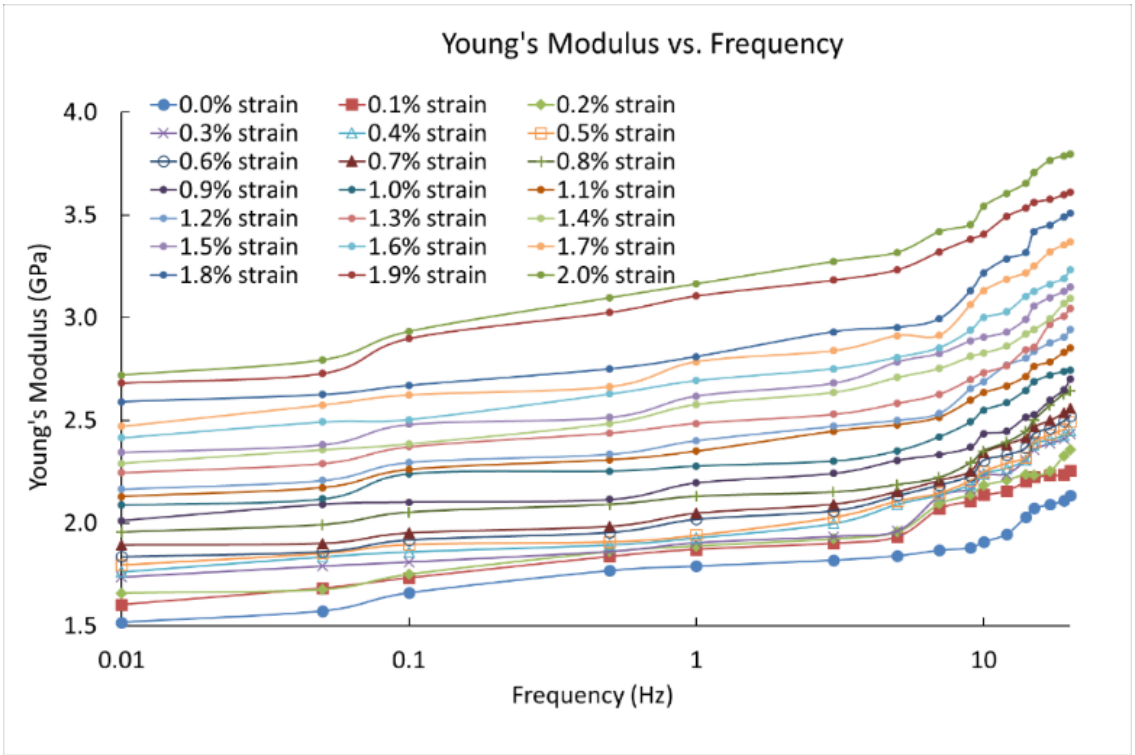

Figure 6-12 Dynamic Young's modulus vs. frequencies (0.01 Hz to 20 Hz) at 3.5 MPa effective pressure.

In order to investigate frequency dependence dynamic properties, the frequency sensitivity factor $\Delta E/\Delta f$ is introduced, which is the ratio of the difference of dynamic Young's modulus and the difference of frequencies. Figure 6.13, Figure 6.14, and Figure 6.15 show the relationship between E/f and axial strain. The E/f increases as the axial strain increases and E/f are bigger at higher effective stress. It is observed that effective stress is a key factor that could influence the dynamic Young's modulus. With increases of effective pressure, the dynamic Young's modulus increases significantly. The frequency sensitivity factor $\Delta E/\Delta f$ increases from 0.0064 to 0.0145, from 0.0161 to 0.0661, and from 0.018 to 0.0567, respectively, at 0.5 MPa, 1.5 MPa and 3.5 MPa effective stress. The same results can also be seen in Figure 6.16, Figure 6.17, and Figure 6.18 where E/E_0 is used as the standard. E/E_0 also increases with increments of axial strain.

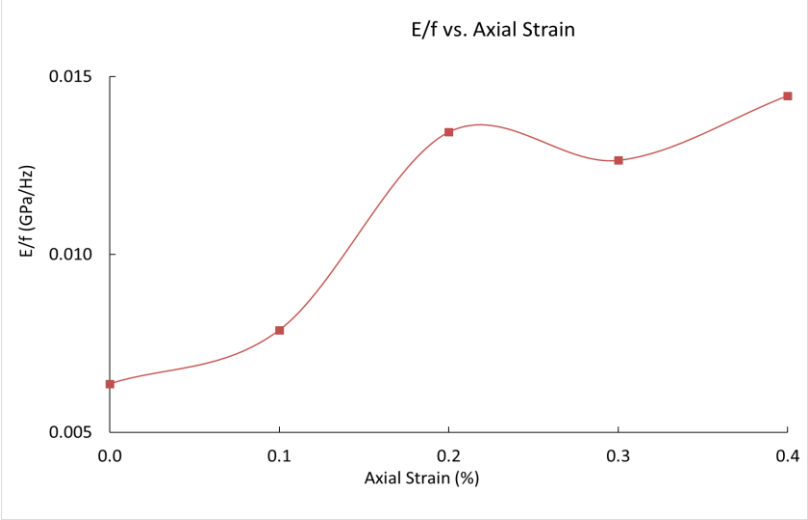

Figure 6-13 The ratio of dynamic Young's modulus and frequencies (0.01 Hz to 20 Hz) vs. axial strain (%) at 0.5 MPa effective pressure.

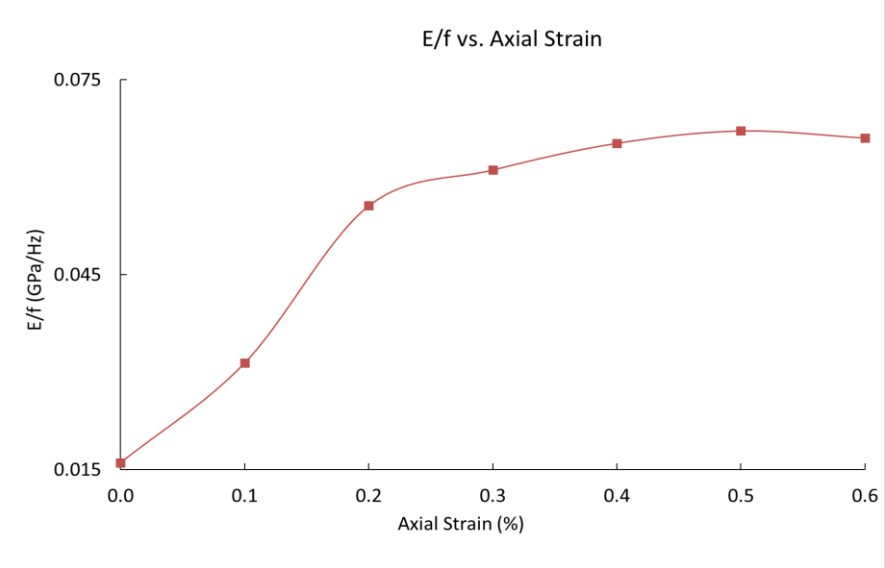

Figure 6-14 The ratio of dynamic Young's modulus and frequencies (0.01 Hz to 20 Hz) vs. axial strain (%) at 1.5 MPa effective pressure.

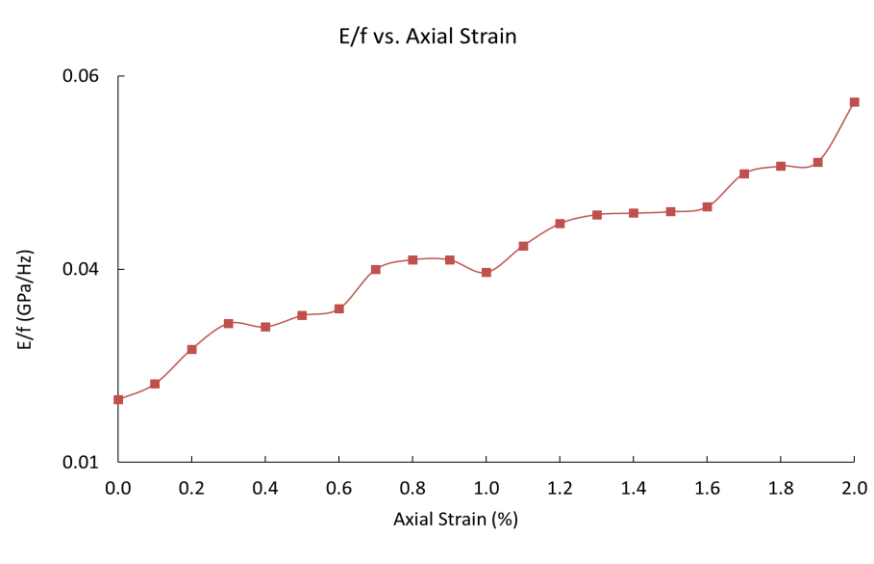

Figure 6-15 The ratio of dynamic Young's modulus and frequencies (0.01 Hz to 20 Hz) vs. axial strain (%) at 3.5 MPa effective pressure.

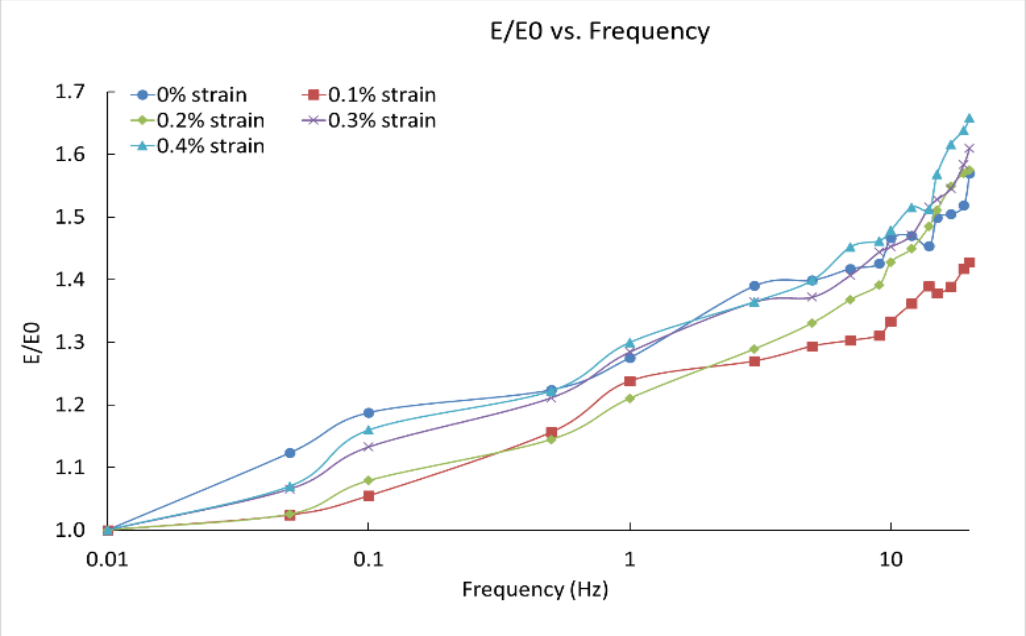

Figure 6-16 The normalized dynamic Young's modulus vs. frequencies (0.01 Hz to 20 Hz) at 0.5 MPa effective pressure.

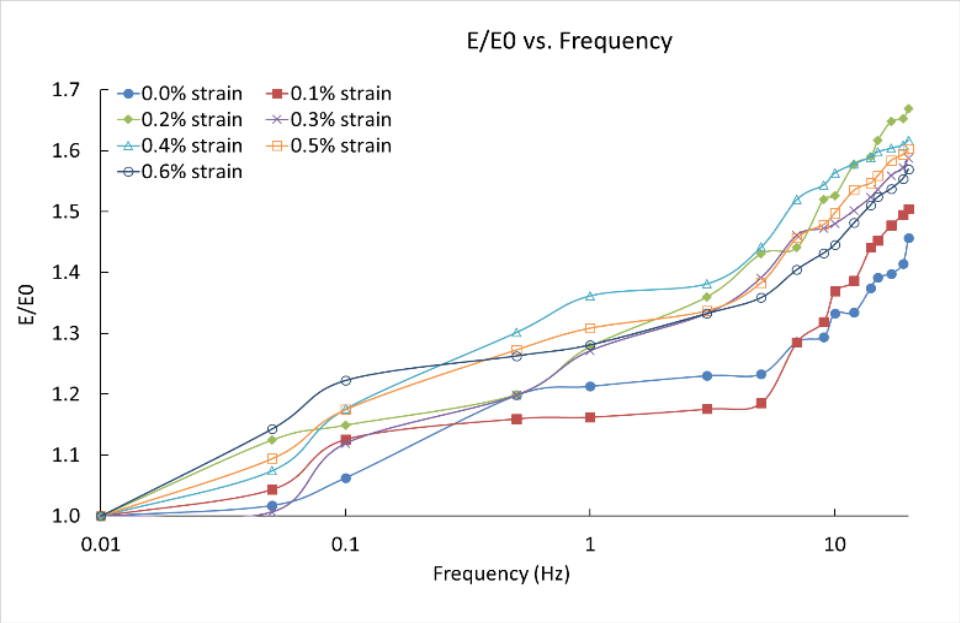

Figure 6-17 The normalized dynamic Young's modulus vs. frequencies (0.01 Hz to 20 Hz) at 1.5 MPa effective pressure.

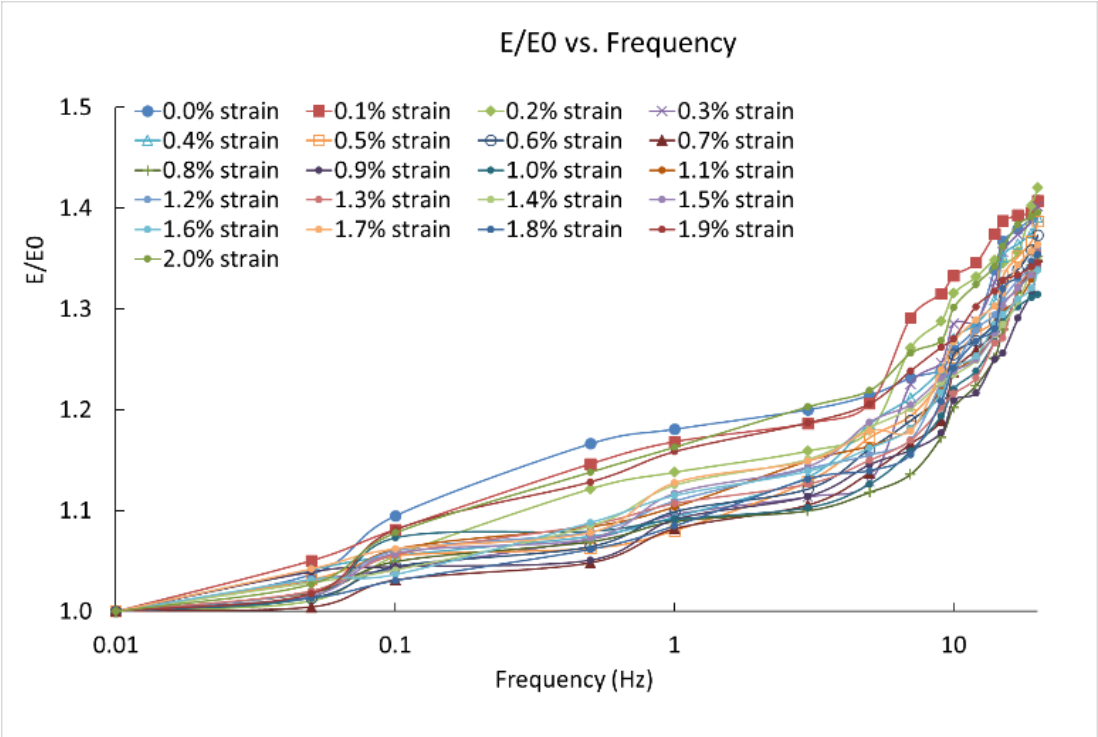

Figure 6-18 The normalized dynamic Young's modulus vs. frequencies (0.01 Hz to 20 Hz) at 3.5 MPa effective pressure.

6.6 **Shear Deformation**

During the compression triaxial tests, both the volumetric strain and axial strain train change. This will affect the density, porosity, and permeability. Based on the following equation porosity changes during shearing stress can be calculated(Equation 6- 4):

$$\emptyset_n = \frac{\varepsilon_v + \emptyset_0}{1 + \varepsilon_v} \quad \text{7- 4}$$

where ϕ_n is corrected porosity at different shearing stress, ϕ_0 is initial porosity before the compression triaxial tests, and ε_v is volumetric strain.

Also, density changes during shearing stress could be obtained based on the volumetric strain curve.

Normalized porosity is introduced for investigating the property changes under shear stress. In Figure 6-19, Figure 6-20, and Figure 6-21, normalized porosity decreases with the axial strain increases due to the contraction of the sample. However, density increases as axial strain increases and is stable as it approaches the failure point (Figure 6-22, Figure 6-23, and Figure 6-24). Density increase can also be explained by the contraction of the sample during the shearing. The contraction that happens at the beginning of loading affects the pore volume reduction and closure of micro-cracks. These findings demonstrate that information about density, porosity, and permeability changes during shear deformation cannot be directly used for simulation. The assumption of Gassmann's equation is no longer valid due to properties changing during deformation (Equation 6- 5 and Equation 6- 6).

$$K^* = K_d + \frac{(1 - \frac{K_d}{K_m})^2}{\frac{\emptyset}{K_f} + \frac{1 - \emptyset}{K_m} - \frac{K_d}{K_m^2}} \quad \text{6- 5}$$

$$\rho = \rho_d + \emptyset\rho_f \quad \text{6- 6}$$

where K^* is the bulk modulus of a sample saturated with a fluid of bulk modulus K_f, K_d is the frame bulk modulus, K_m is the gain bulk modulus, ρ is the fluid-saturated density of the sample, ρ_d is the dry density of the sample, ρ_f is the pore fluid's density, and ϕ is porosity.

It is important to obtain experimental data at seismic frequencies under shear deformation. From the literature review, when solid fill is replaced by liquid, the Poisson ratio decreases insignificantly since shear waves cannot propagate in a fluid. In order to build a time-lapse seismic interpretation template, Poisson's ratio must be assumed as a constant for further analysis.

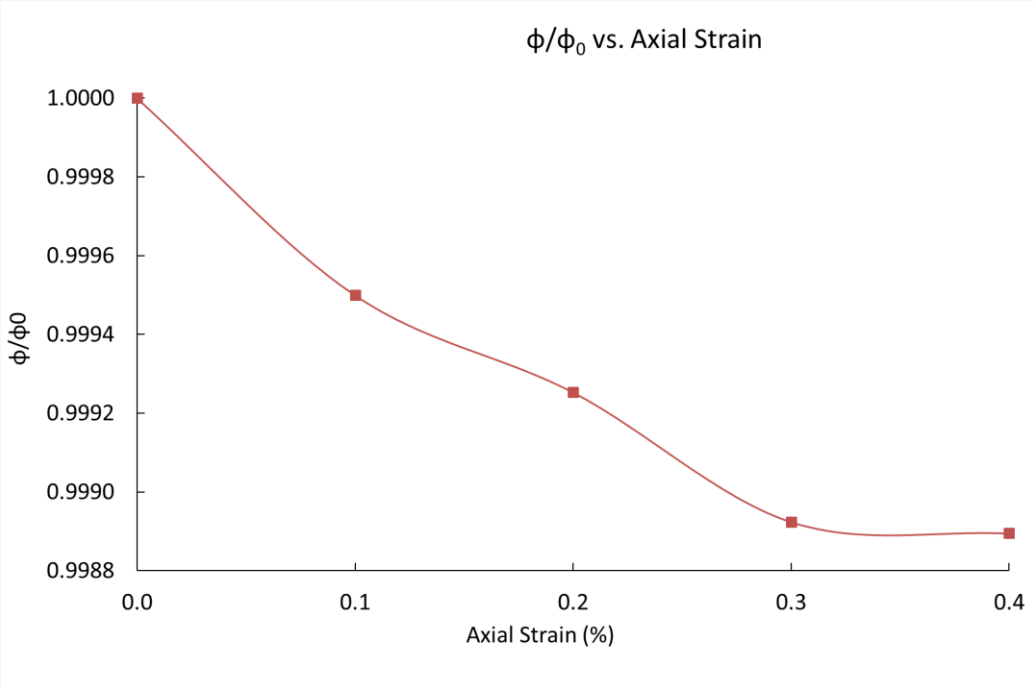

Figure 6-19 The normalized porosity vs. axial strain (%) at 0.5 MPa effective pressure.

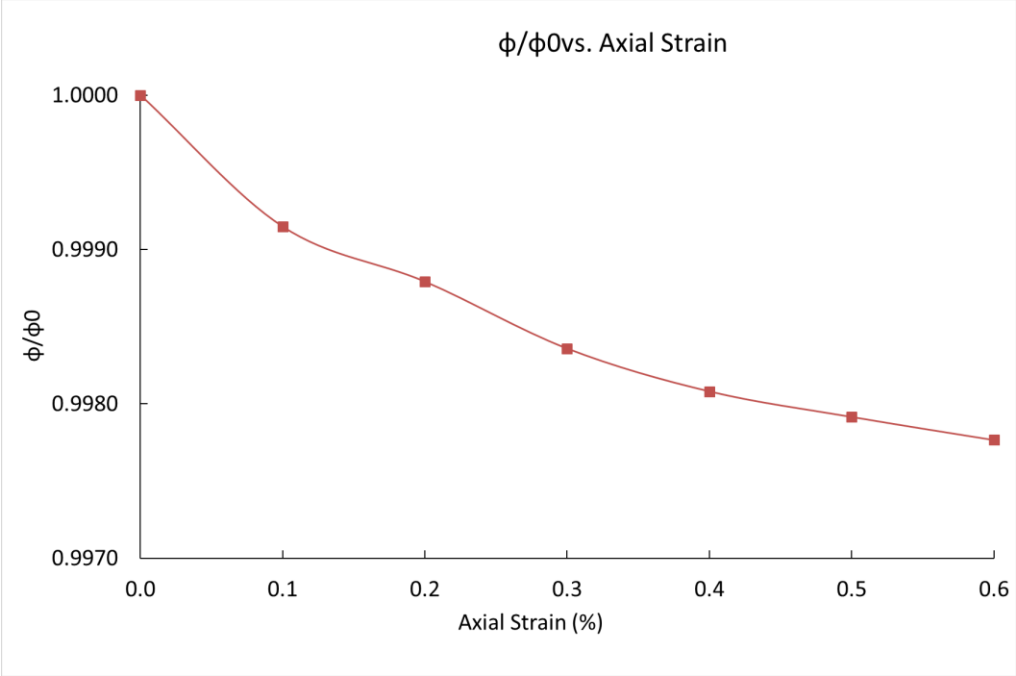

Figure 6-20 The normalized porosity vs. axial strain (%) at 1.5 MPa effective pressure.

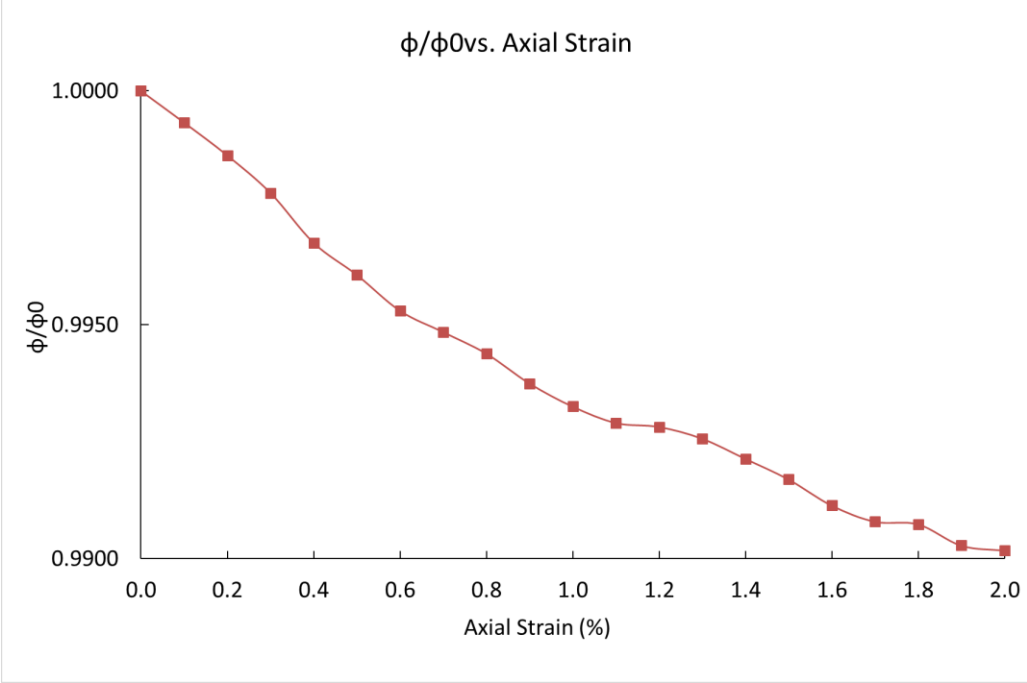

Figure 6-21 The normalized porosity vs. axial strain (%) at 3.5 MPa effective pressure.

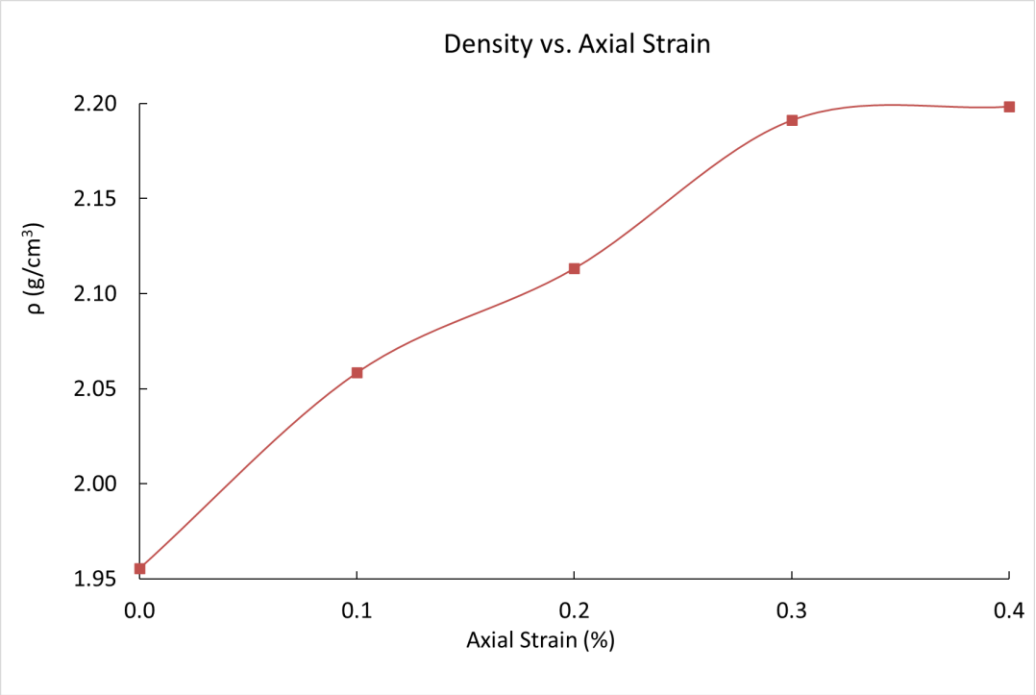

Figure 6-22 Density vs. axial strain (%) at 0.5 MPa effective pressure.

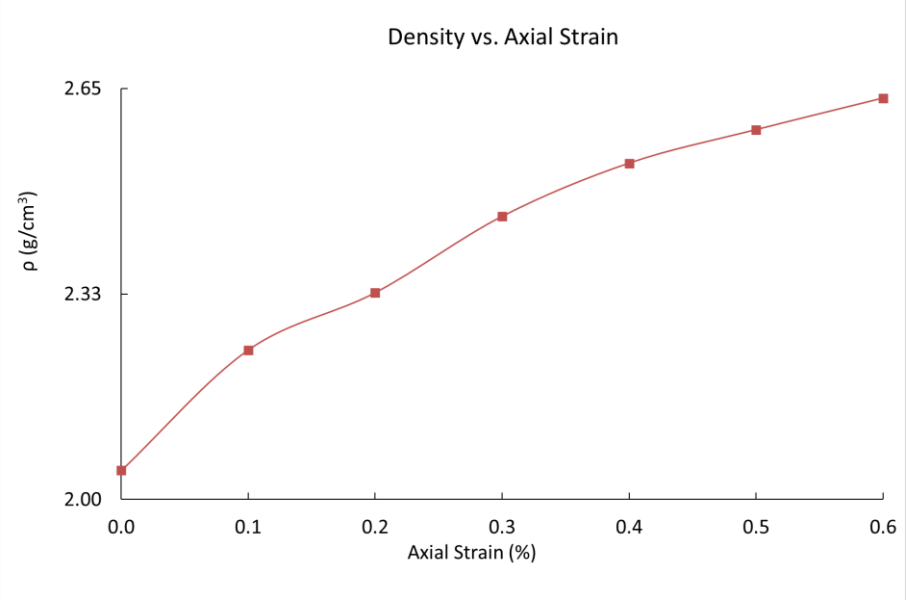

Figure 6-23 Density vs. axial strain (%) at 1.5 MPa effective pressure.

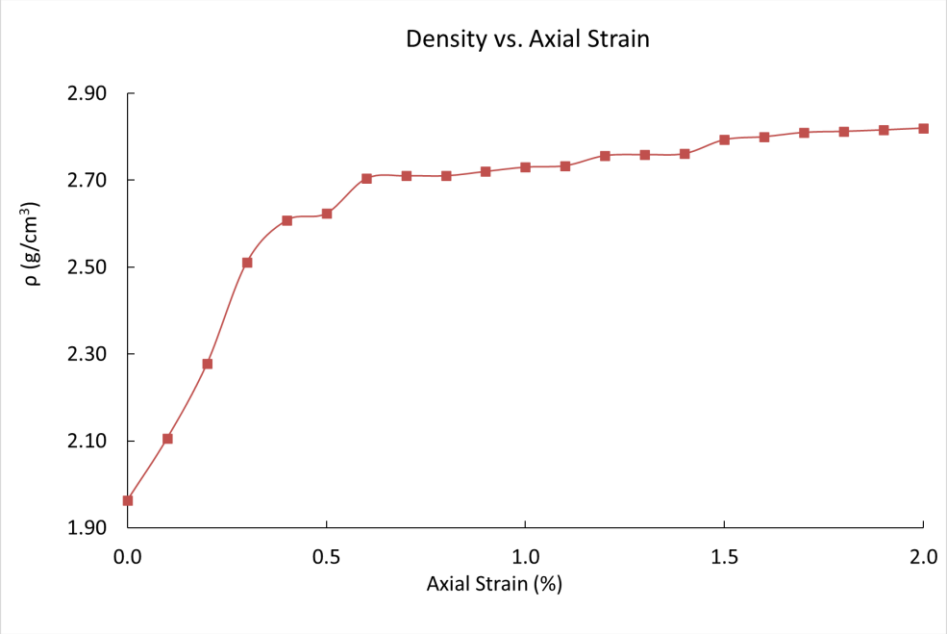

Figure 6-24 Density vs. axial strain (%) at 3.5 MPa effective pressure.

Figure 6-25, Figure 6-26, and Figure 6-27 are the relationship between Young's modulus and porosity. Young's modulus decreased with increasing porosity. At 0.5 MPa, porosity only changed 0.04% but Young's modulus increased 89% at 1 Hz and 20 Hz. Porosity changed 0.3% under 3.5 MPa and Young's modulus increased 76.5% at 1 Hz and 78.4% at 20 Hz. This is because the pore volume and micro-cracks are still sensitive at lower effective pressure.

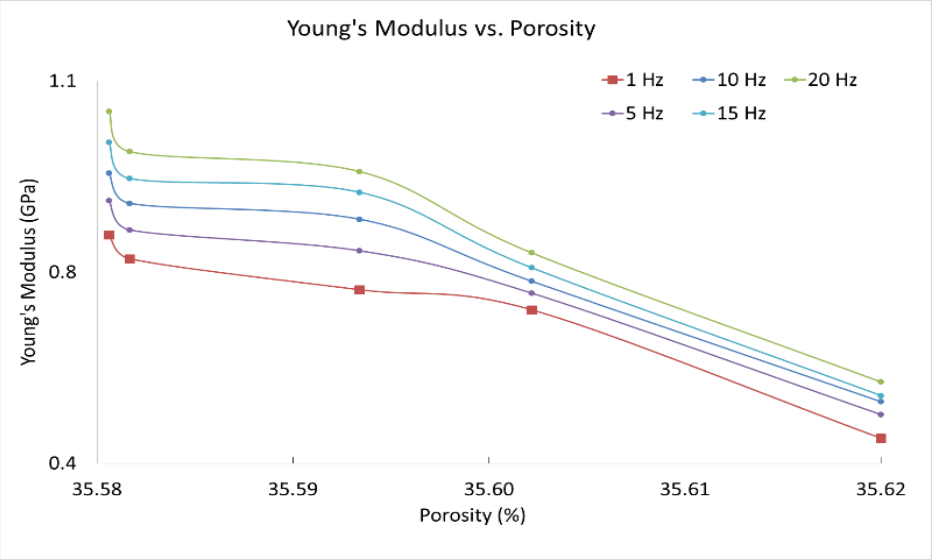

Figure 6-25 The dynamic Young's modulus vs. porosity at 0.5 MPa effective pressure.

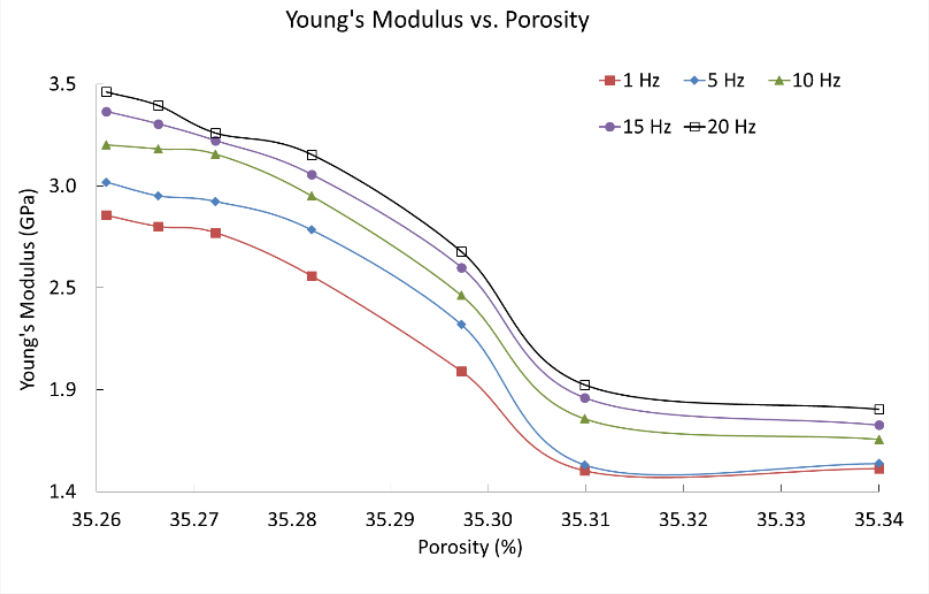

Figure 6-26 The dynamic Young's modulus vs. porosity at 1.5 MPa effective pressure.

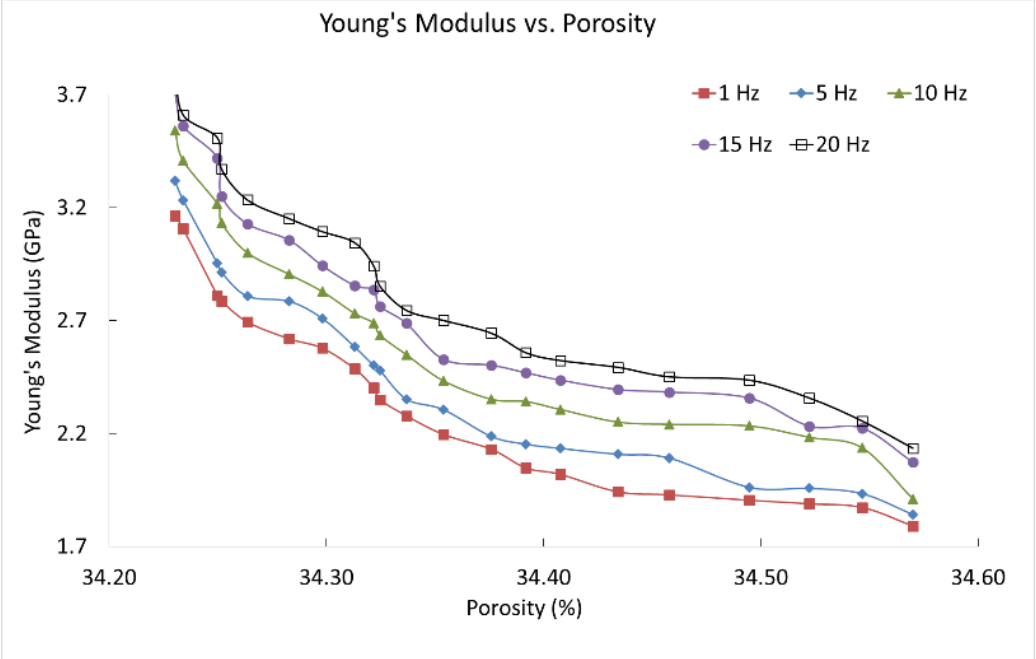

Figure 6-27 The dynamic Young's modulus vs. porosity at 3.5 MPa effective pressure.

In the triaxial test, volumetric strain is required to define the contraction or dilation of the sample and is determined as follows (Equation 6- 7):

$$\varepsilon_v = \varepsilon_{xx} + \varepsilon_{yy} + \varepsilon_{zz} \qquad 6\text{- }7$$

where ε_{xx}, ε_{yy}, and ε_{zz} represent the normal strain in the x-direction, y-direction, and z-direction.

For the tested sample, $\varepsilon_{yy,} = \varepsilon_{zz}$. Strain can therefore be obtained by (Equation 6- 8):

$$\varepsilon_v = \varepsilon_a + 2\varepsilon_r \qquad 6\text{- }8$$

where ε_v represents the volumetric strain, ε_a is the axial strain, and ε_r is the radial strain.

Figure 6-28, Figure 6-29, and Figure 6-30 show the relationship between Young's modulus and axial strain at 0.5 MPa, 1.5 MPa, and 3.5 MPa effective pressure. Young's modulus increases with increasing axial strain and effective pressure. From 0.5 MPa to 3.5 MPa, Young's modulus increased from 0.45 GPa to 1.79 GPa which is a 300% increment at 1 Hz. The Young's modulus increased almost the same amount at 20 Hz indicating that frequencies are not sensitive to effective pressure.

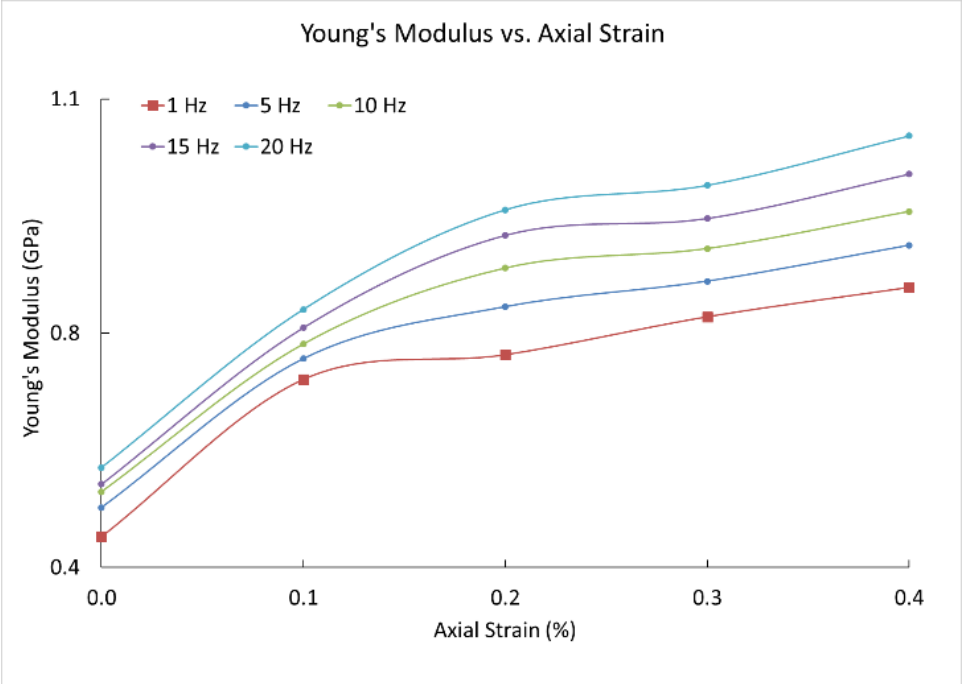

Figure 6-28 The dynamic Young's modulus vs. axial strain at 0.5 MPa effective pressure.

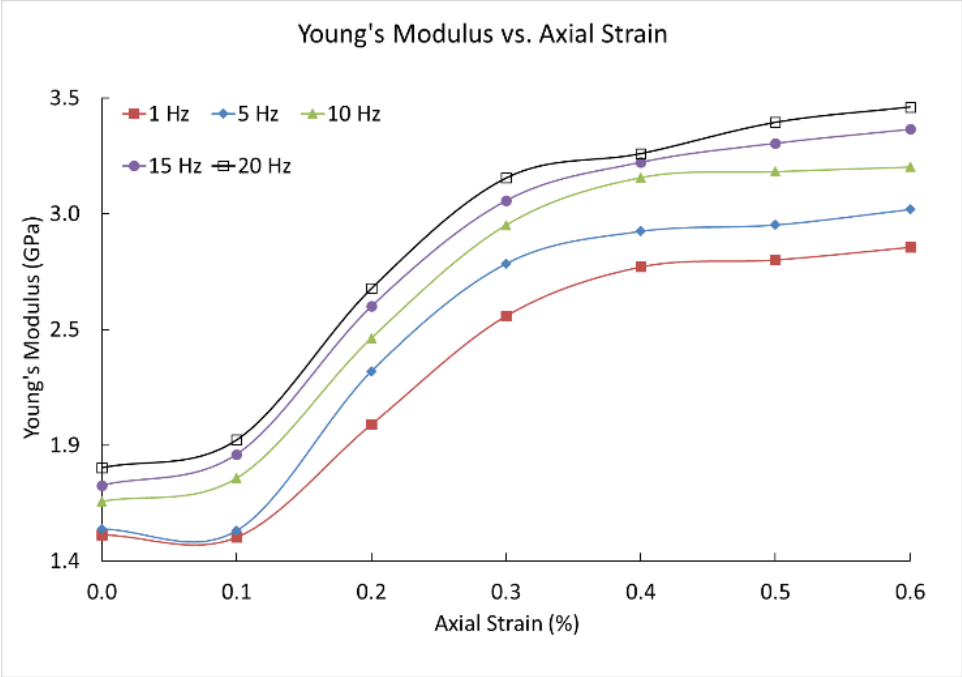

Figure 6-29 The dynamic Young's modulus vs. axial strain at 1.5 MPa effective pressure.

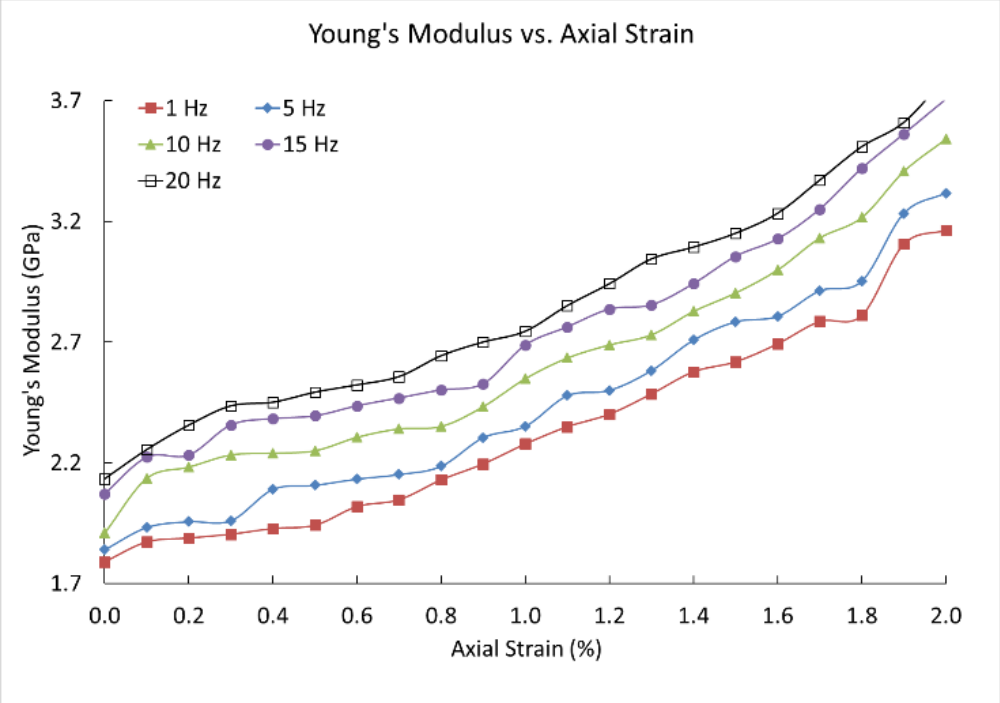

Figure 6-30 The dynamic Young's modulus vs. axial strain at 3.5 MPa effective pressure.

As shown in Figure 6-31, Figure 6-32, and Figure 6-33, the relationship between Young's modulus and shear strain is displayed. At higher effective pressure, the shear strain can be up to 3.5%, while the shear strain is only 0.7% at 0.5 MPa effective pressure. Young's modulus also increased with shear strain increasing.

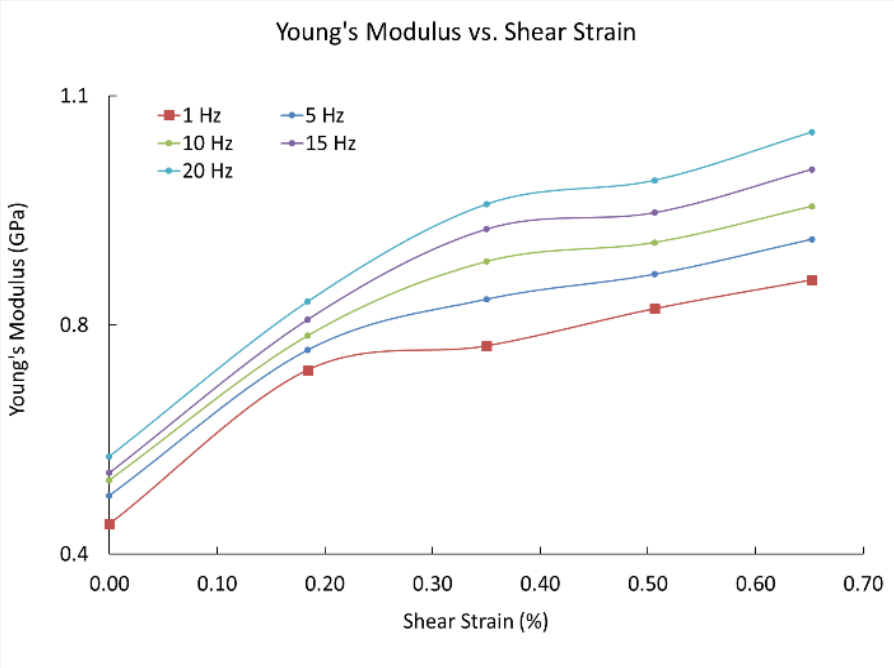

Figure 6-31 The dynamic Young's modulus vs. shear strain at 0.5 MPa effective pressure.

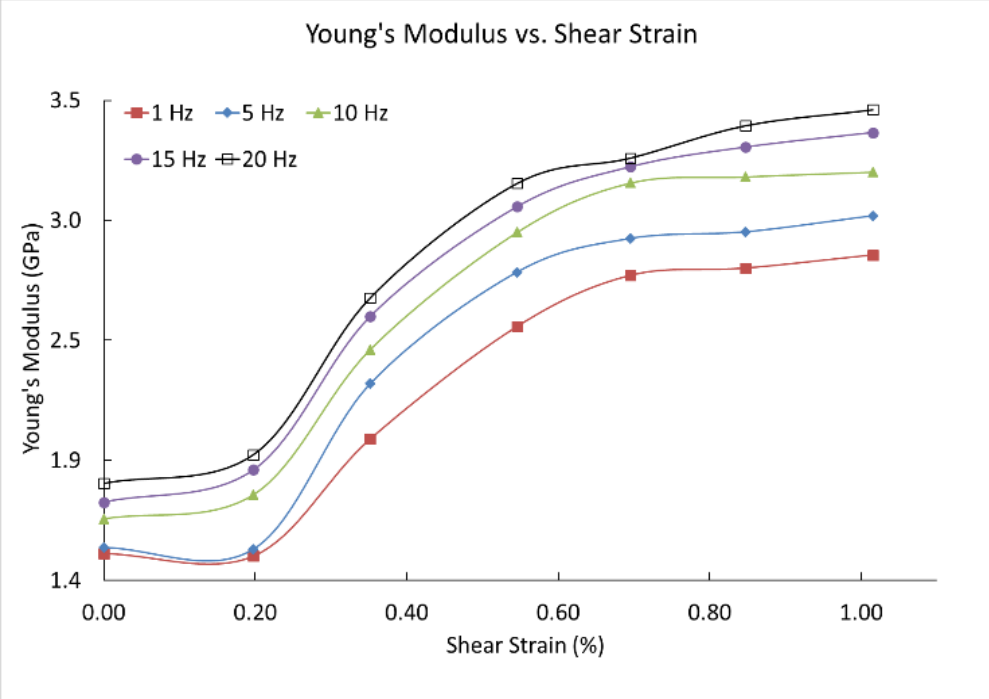

Figure 6-32 The dynamic Young's modulus vs. shear strain at 1.5 MPa effective pressure.

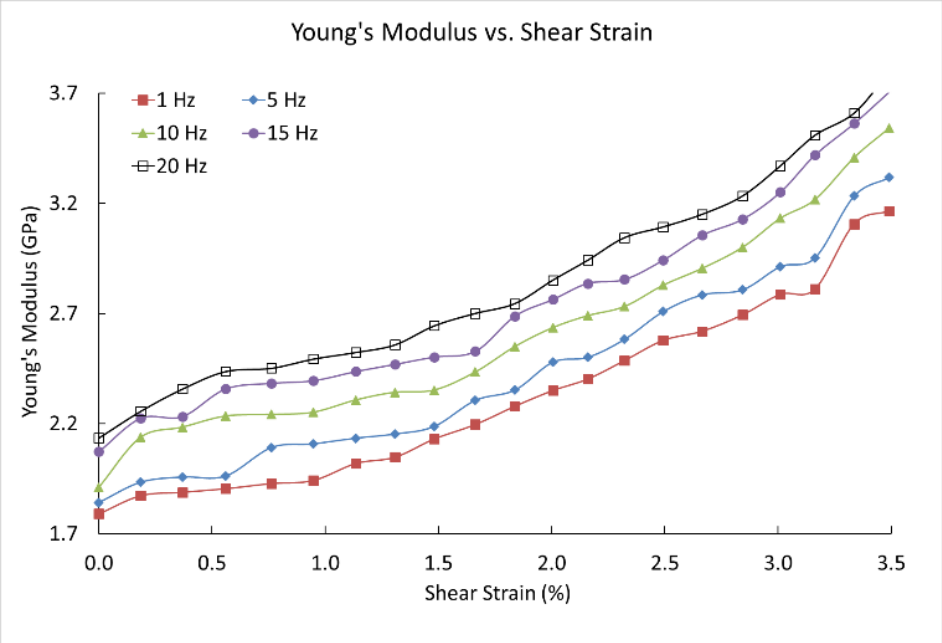

Figure 6-33 The dynamic Young's modulus vs. shear strain at 3.5 MPa effective pressure.

Figure 6-34, Figure 6-35, and Figure 6-36 show that Young's modulus changes as a function of volumetric strain. All samples tested contracted at the beginning of shear deformation. Volumetric strain reaches -1.0% at 3.5 MPa effective pressure. Young's modulus decreases with increasing volumetric strain.

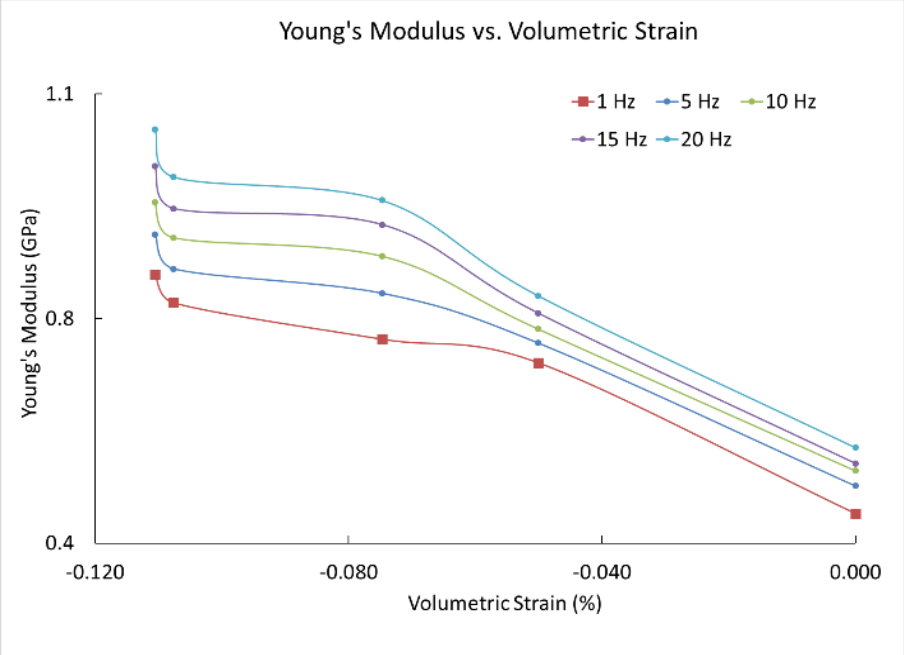

Figure 6-34 The dynamic Young's modulus vs. volumetric strain at 0.5 MPa effective pressure.

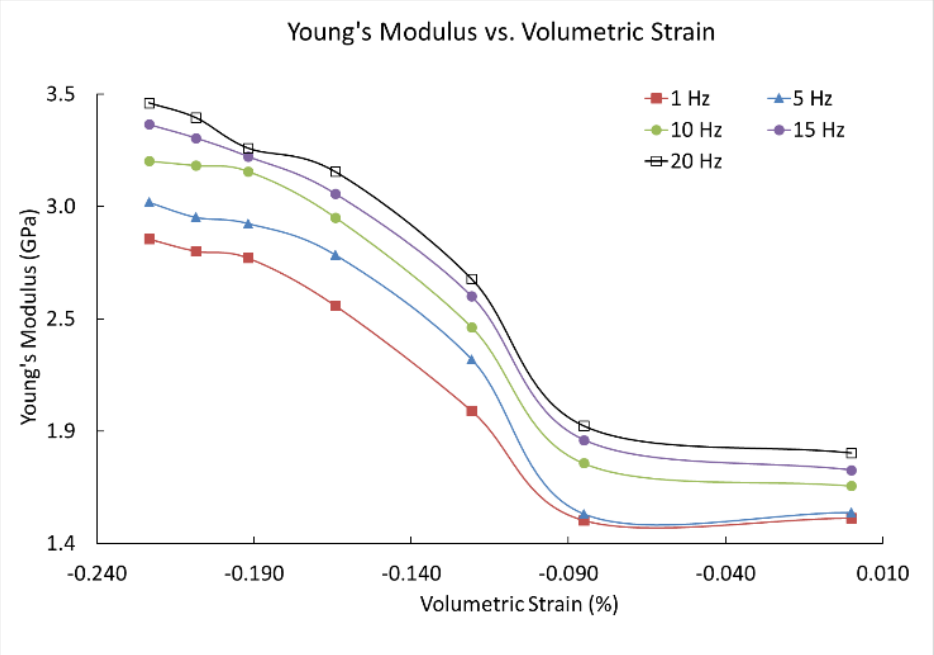

Figure 6-35 The dynamic Young's modulus vs. volumetric strain at 1.5 MPa effective pressure.

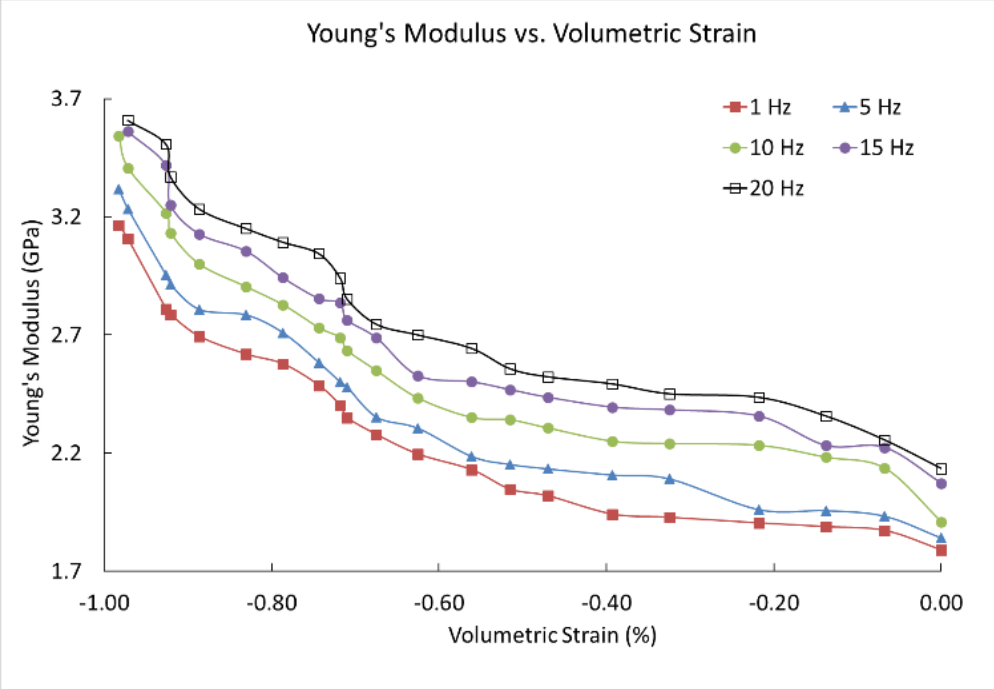

Figure 6-36 The dynamic Young's modulus vs. volumetric strain at 3.5 MPa effective pressure.

It is important to obtain experimental data at seismic frequencies under shear deformation. From the literature review, when solid fill is replaced by liquid, the Poisson's ratio decreases insignificantly since there is no shear wave in the fluid. In order to build a time-lapse seismic interpretation template, the Poisson's ratio is assumed to be constant during further analysis. Compressional wave velocity and shear wave velocity could be obtained using Equation 6- 9 and Equation 6- 10

$$V_p = \sqrt{\frac{E(1-\upsilon)}{\rho(1+\upsilon)(1-2\upsilon)}} \qquad 6\text{- }9$$

$$V_s = \sqrt{\frac{E}{2\rho(1+\upsilon)}} \qquad 6\text{- }10$$

where Vp and Vs represent P wave velocity and S wave velocity, E represents Young's modulus, ν is Poisson's ratio, and ρ is density.

Acoustic impedance (V_p*ρ) can be used to identify changes in lithology, porosity, and saturation, and is essential to use for time-lapse seismic interpretation. Figure 6-37, Figure 6-38, and Figure 6-39 plot the relationship between acoustic impedance and axial strain at different frequencies and various effective pressures. Acoustic impedance is influenced by frequencies, axial strain, and effective pressure. With increases of effective pressure, acoustic impedance changes from 1.01 to 2.32 at 1 Hz. Acoustic impedance changes 59.84% at different effective pressures, which are useful for time-lapse seismic interpretation.

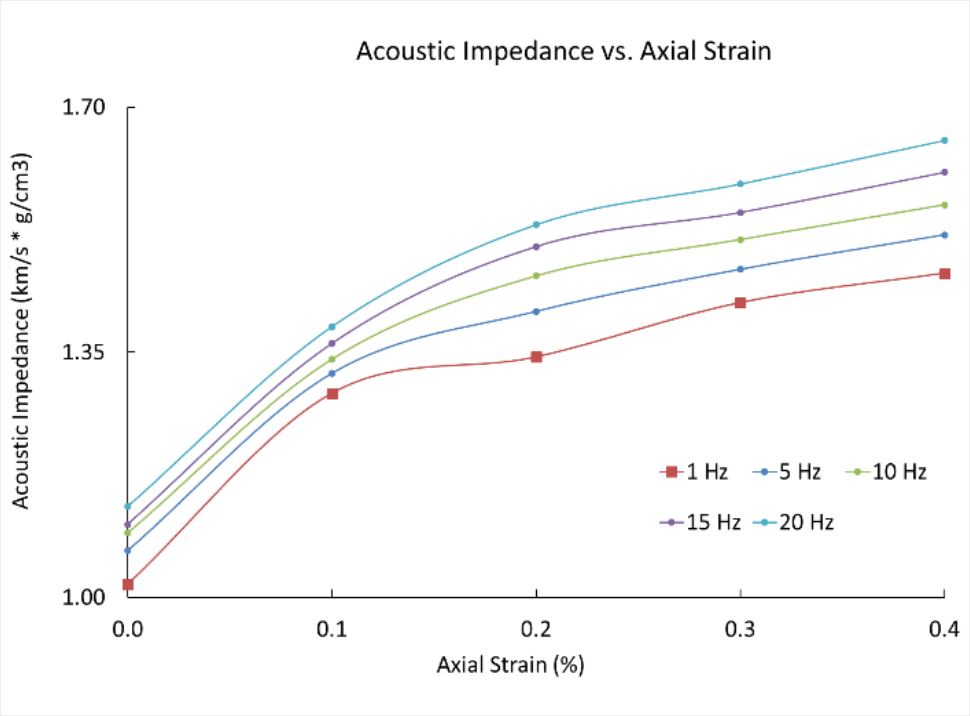

Figure 6-37 Acoustic impedance vs. axial strain at 0.5 MPa effective pressure.

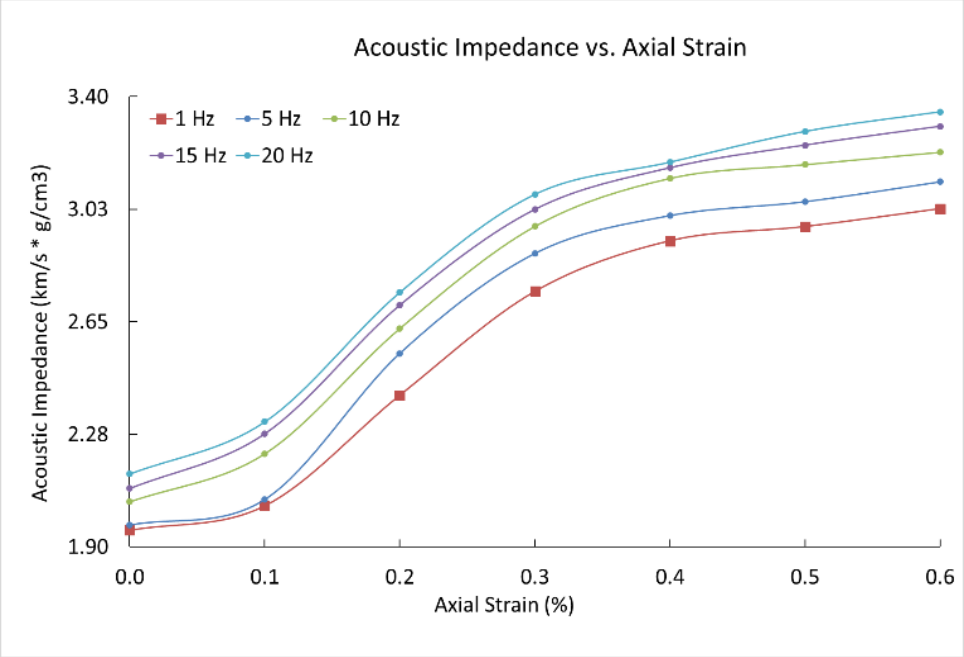

Figure 6-38 Acoustic impedance vs. axial strain at 1.5 MPa effective pressure.

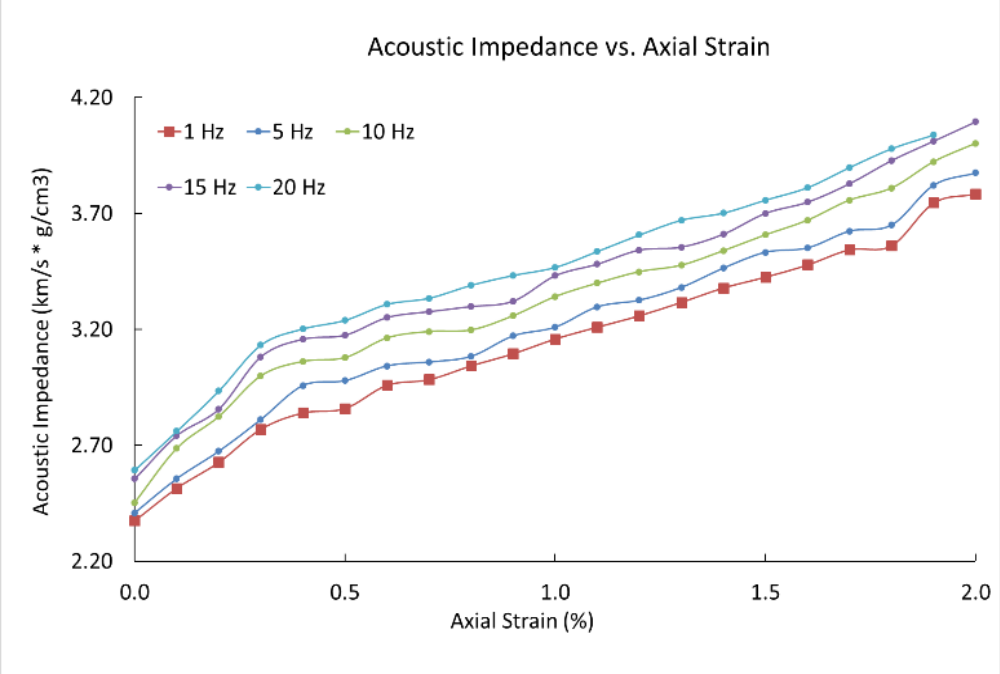

Figure 6-39 Acoustic impedance vs. axial strain at 3.5 MPa effective pressure.

The following is a case study simulating dynamic property changes induced by steam injection. Effective pressure is constant in the beginning with a change from 0% axial strain to 0.2% axial strain. The effective pressure builds up to 1.5 MPa with shear deformation to 0.5% axial strain. In addition, the effective pressure continues to increase to 3.5 MPa due to the steam injection. Finally, the frequency of seismic survey changes from 1 Hz to 5 Hz to enhance the resolution with axial strain up to 2% (approaching failure point). Figure 6-40 shows the relationship between λρ and μρ and Figure 6-41 shows the relationship between V_p/V_s and acoustic impedance.

With increasing axial stress, acoustic impedance increases slightly with the constant V_p/V_s while λρ and μρ increase significantly. The effective pressure increases from 0.5 MPa to 1.5 MPa causing a significant change in λρ and μρ and slightly changing V_p/V_s and acoustic impedance. Both acoustic impedance and μρ drop with increasing axial strain at 1.5 MPa effective pressure. Finally, λρ, μρ and acoustic impedance change with axial strain and frequencies with a stable V_p/V_s.

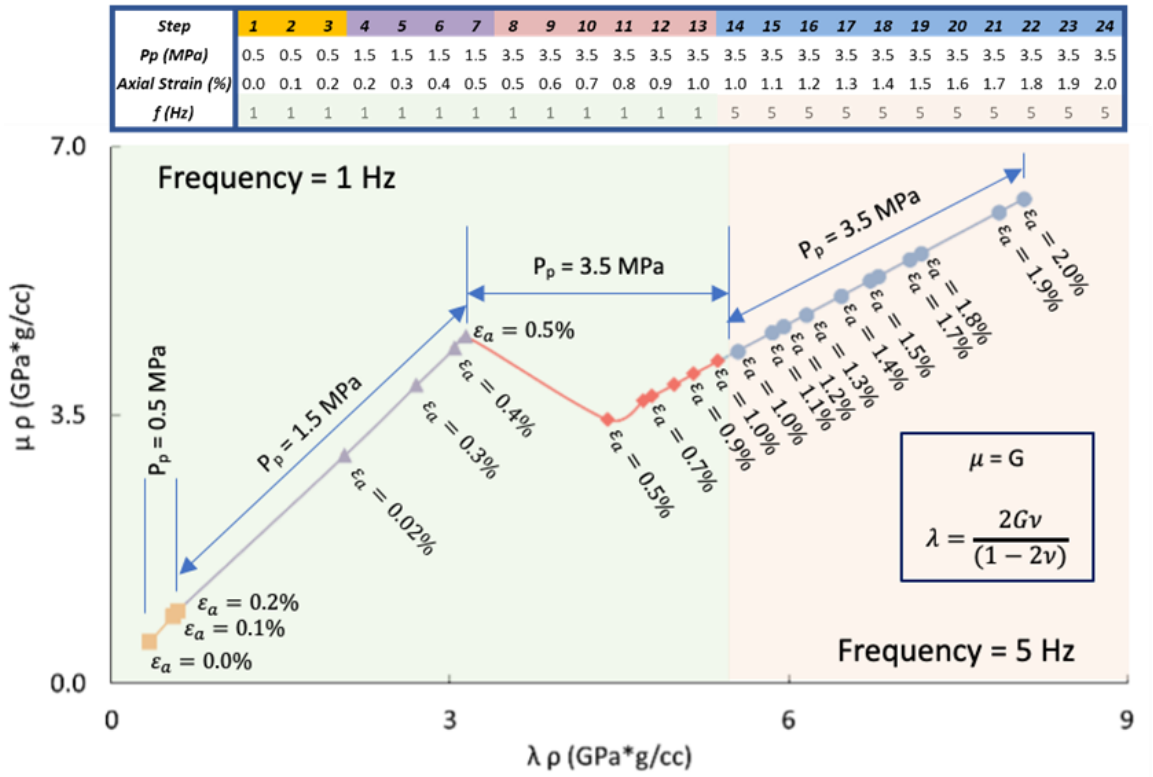

Figure 6-40 Sequential μρ and λρ changes induced by steam injection. Sequential reservoir condition changes are represented by 24 steps.

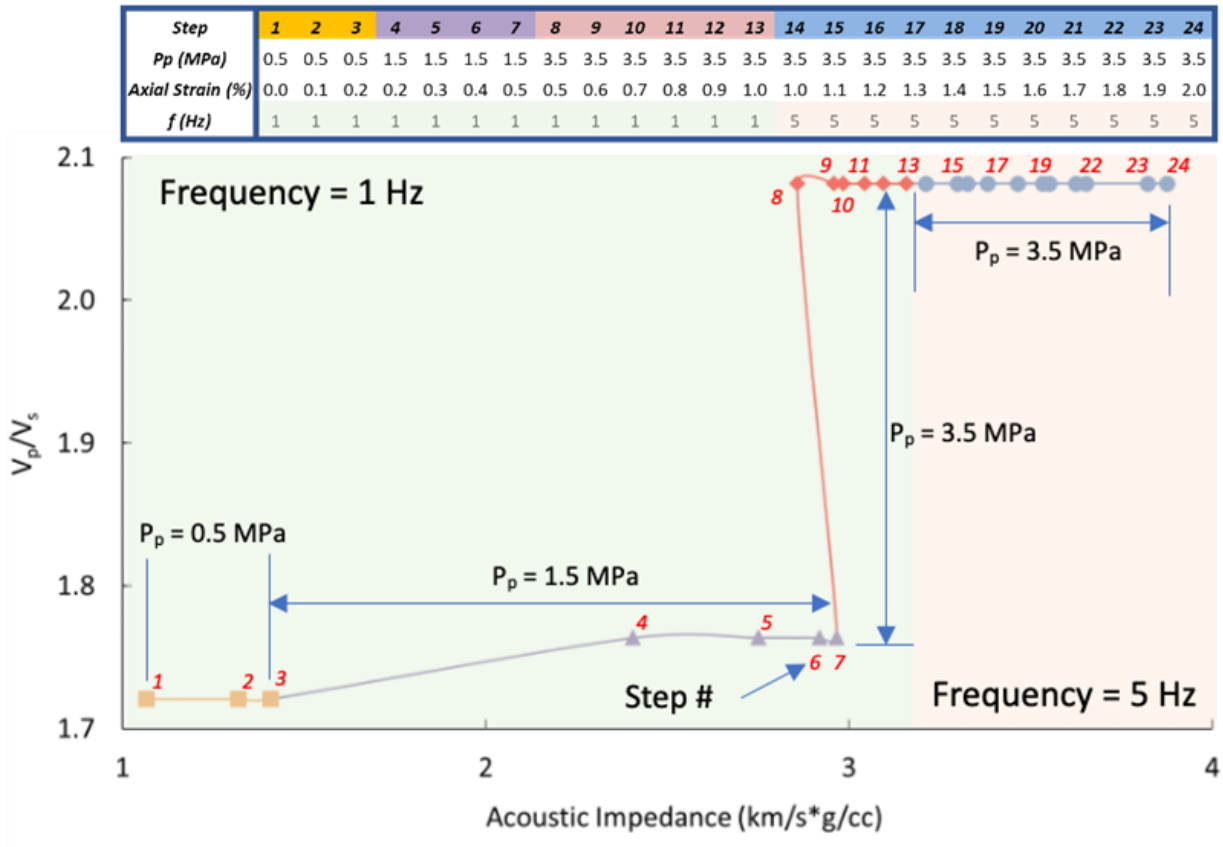

Figure 6-41 Sequential acoustic impedance and V_P/V_S ratio changes induced by steam injection. Sequential reservoir condition changes are represented by 24 steps.

6.7 **Conclusions**

This chapter shows the testing results obtained by the innovative triaxial seismic frequencies testing system. Three compression tests on different stress were conducted by using artificial dense sand samples. One of the most significant findings in the dense sand samples is the frequencies have a significant influence on the dynamic properties under deviatoric stress conditions. The dynamic Young's modulus is much more sensitive at lower axial stress and effective pressure. With the increase of confining pressure and deviatoric stress, the dynamic Young's modulus will increase. A template for 4D seismic interpretation has been developed based on the results. From the template, the influence of the frequencies has been proven.

7 CONCLUSIONS AND RECOMMENDATIONS

7.1 **Conclusions**

This thesis developed a seismic triaxial testing system to study dynamic and static geomechanical properties at seismic frequencies. Seismic frequency measurements are difficult to measure directly in the laboratory, so forced oscillation method based on MTS system and the novel triaxial cell was used in this research. This thesis presents several tests were conducted to study and develop the limitation and the capacity of the MTS system. The tuning and calibration tests prove that the MTS can conduct tests from 0.01 Hz to 20 Hz using force control and displacement control modes with an axial strain of 10^{-6}.

This study took advantage of 3D printer technology to investigate the dynamic properties of 3D printed samples with different orientations. Five different orientation specimens have been tested. Non-dispersion can be found in the 3D printer samples. The 0°, 30°, and 45° 3D printer samples show that Young's modulus is equal, but for 60° and 90° 3D printer samples, Young's modulus will increase due to the anisotropic behavior. And 90° sample shows a highest Young's Modulus. But the anisotropic behavior can be observed. Young's modulus of 90° 3D printer samples are not sensitive to the lower stress but increasing significantly at higher stress under the loading path. This is because the 3D additive manufacturing binder jet technology, so the more binding resin accumulate on the 90° 3D printer samples and the contact area of 90° 3D printer samples increase. Also, the difference between the loading path and unloading path can be found. The reason is that the sand grain may have rearrangement under the compression. The result can be extended to modify and verify the existing models and interpretation temples for seismic data and ultrasonic data.

Based on knowledge of USC tests, a triaxial system was developed. This innovative triaxial system was based on two loading systems, which could protect the dual load cell testing system. The testing system has been proven at seismic frequencies from 0.01 to 20Hz and nanometer scale accuracy, axial stress up to 150 kN, radial pressures and pore pressures up to 40 MPa. By using a pair of laser displacement sensors, the dynamic axial displacement could be obtained at the nm scale. This facility is, therefore, suitable for dense sand specimens.

Three triaxial tests were conducted under three varying effective pressures 0.5 MPa, 1.5 MPa, and 3.5 MPa over a range of frequencies on three dense specimens where the pore pressure was kept constant at 2000 kPa and pore fluid was free to move in or out of the sample. The sample preparation technique, developed and improved in this study, provides a feasible and practical method to produce such oil sands specimens with high quality The dense sand specimens were well characterized, with density, permeability and porosity measured. Both the dynamic and static moduli were obtained at different stress levels. The static elastic and strength parameters of the dense sands were obtained in the lab-scale tests. All the parameters measured through the triaxial compression testing could then input the geomechanical models to assess the impacts of geomechanical dilation as a start-up in full SAGD performance. The dynamic elastic parameters of the dense sands were obtained by stress-strain method at different frequencies. The static Young's modulus increased in the very beginning, but it decreased with the axil stress increasing. However, the dynamic Young's modulus increases as the axial stress increases. So, the difference between static Young's modulus and dynamic Young's modulus is much more significant when the sample approaches to the failure point. Detailed procedures have been developed for preparing the dense sand samples and conducting dynamic triaxial tests in the future. Seismic interpretation templates have been proposed by using this newly acquired experimental data.

The most important contribution of the current work is the comprehensive experimental study on the seismic frequencies measurement system development. A new instrument suitable for measuring seismic frequencies properties in rock samples has been designed, built, calibrated and utilized to produce new datasets serving to understand the static and dynamic geomechanical properties. To the best of my knowledge, this apparatus employs all kinds of rock samples under shear deformation for such experiments to Measure both quasistatic and multi-frequency dynamic responses within a single experiment. The new experimental setup can be used to study the impact of saturation, temperatures, shear stress, and stress path on seismic frequencies, as well as the relation of static to dynamic stiffness.

7.2 **Recommendations for future research**

The following comments provide some recommendations for future research and application of developments presented in this dissertation.

1. The system is still under development to produce more accurate results. The manual turning thrust nut could be upgraded to a motor control system that would monitor loading rate during triaxial testing. Also, a motor control system would ease loading and unloading tests.

2. High-temperature tests need to be conducted in the future. The purpose of the research is to develop a testing system for investigating seismic geomechanics properties at high temperatures and pressure because experimental data that could be used for SAGD projects is insufficient.

3. In order to have a broad frequency measurement system, ultrasonic measurement needs to be added. This will promote a better understanding of attenuation at different frequencies. Comparing ultrasonic measurements with the well logging and ultrasonic core data, full frequency-dependence rock physics and geomechanical models will propose a broad frequency measurement system.

4. Rock physics and geomechanical models need to be validated using seismic data to monitor in situ recovery processes in unconventional reservoirs. A new workflow that guides the procedural integration of 4D seismic data, well logging data, and core data will be tested by using sequentially coupled reservoir geomechanical simulations.

Reference

Adam, L. *et al.* (2009) 'Seismic wave attenuation in carbonates', *Journal of Geophysical Research*, 114(B6), p. B06208. Doi: 10.1029/2008JB005890.

Batzle, M. L., Han, D.-H. and Hofmann, R. (2006) 'Fluid mobility and frequency-dependent seismic velocity — Direct measurements', *GEOPHYSICS*, 71(1), pp. N1–N9. Doi: 10.1190/1.2159053.

Batzle, M. and Wang, Z. (1992) 'Seismic properties of pore fluids', *GEOPHYSICS*, 57(11), pp. 1396–1408. Doi: 10.1190/1.1443207.

Biot, M. a. (1956a) 'Theory of Propagation of Elastic Waves in a Fluid-Saturated Porous Solid. I. Low-Frequency Range', *The Journal of the Acoustical Society of America*, 28(2), p. 168. Doi: 10.1121/1.1908239.

Biot, M. a. (1956b) 'Theory of Propagation of Elastic Waves in a Fluid-Saturated Porous Solid. II. Higher Frequency Range', *The Journal of the Acoustical Society of America*, 28(2), pp. 179–191. Doi: 10.1121/1.1908241.

Birch, F. (1960) 'The velocity of compressional waves in rocks to 10 kilobars: 1.', *Journal of Geophysical Research*, 66(4), pp. 1083–1102. Doi: 10.1029/JZ065i004p01083.

Birch, F. (1961) 'The velocity of compressional waves in rocks to 10 kilobars: 2.', *Journal of Geophysical Research*, 66(7), pp. 2199–2224. Doi: 10.1029/JZ066i007p02199.

Cadoret, T., Marion, D. and Zinszner, B. (1995) 'Influence of frequency and fluid distribution on elastic wave velocities in partially saturated limestones', *Journal of Geophysical Research*, 100(B6), p. 9789. Doi: 10.1029/95JB00757.

Danaei, Shahram, et al. "Using petro-elastic proxy model to integrate 4D seismic in ensemble based data assimilation." Journal of petroleum science and engineering 194 (2020): 107457.

David, E. C. *et al.* (2013) 'Laboratory measurements of low- and high-frequency elastic moduli in Fontainebleau sandstone', *GEOPHYSICS*, 78(5), pp. D369–D379. Doi: 10.1190/geo2013-0070.1.

Dunn, K. J. (1987) 'Sample boundary effect in acoustic attenuation of fluid-saturated porous cylinders', *Journal of the Acoustical Society of America*, 81(5), pp. 1259–1266. Doi: 10.1121/1.394529.

Dvorkin, J., Mavko, G. and Nur, A. (1995) 'Squirt flow in fully saturated rocks', *GEOPHYSICS*, 60(1), p. 97. Doi: 10.1190/1.1443767.

Dvorkin, J. and Nur, A. (1993) 'Dynamic poroelasticity: A unified model with the squirt and the Biot mechanisms', *GEOPHYSICS*, 58(4), pp. 524–533. Doi: 10.1190/1.1443435.

Fjaer, E. (2019) 'Relations between static and dynamic moduli of sedimentary rocks', *Geophysical Prospecting*, 67(1), pp. 128–139. Doi: 10.1111/1365-2478.12711.

Fjær, E. (2015) 'Static versus dynamic moduli another piece in the puzzle', in. Available at: https://www.onepetro.org/conference-paper/ARMA-2015-409.

Gardner, G. H. F., Wyllie, M. R. J. and Droschak, D. M. (1964) 'Effects of Pressure and Fluid Saturation on the Attenuation of Elastic Waves in Sands', *Journal of Petroleum Technology*, 16(02), pp. 189–198. Doi: 10.2118/721-PA.

Gassmann, F. (1951) 'Über die Elastizität poröser Medien', *Vierteljahrsschrift der naturforschenden Gesellschaft*, 96(1), pp. 1–23. Doi: 10.1.1.48.9319.

Gregory, A. R. (1976) 'FLUID SATURATION EFFECTS ON DYNAMIC ELASTIC PROPERTIES OF SEDIMENTARY ROCKS', *GEOPHYSICS*, 41(5), pp. 895–921. Doi: 10.1190/1.1440671.

Han, D.-H. (1986) *Effects of porosity and clay content on acoustic properties of sandstones and unconsolidated sediment*. Standford University.

Helgerud, M. B. *et al.* (2011) '4D in the deepwater Gulf of Mexico: Hoover, Madison, and Marshall fields', *The Leading Edge*, 30(9), pp. 1008–1018. Doi: 10.1190/1.3640524.

Hodder, K. J., Nychka, J. A. and Chalaturnyk, R. J. (2018) 'Process limitations of 3D printing model rock', *Progress in Additive Manufacturing*. Springer International Publishing, 0(0), p. 0. Doi: 10.1007/s40964-018-0042-6.

Holt, R. M., Bauer, A. and Bakk, A. (2018) 'Stress-path-dependent velocities in shales: Impact on 4D seismic interpretation', *GEOPHYSICS*, 83(6), pp. MR353–MR367. Doi: 10.1190/geo2017-0652.1.

Al Hosni, M. *et al.* (2016) 'Case History : Using time-lapse vertical seismic profiling data to constrain velocity-saturation relations: the Frio brine pilot CO 2 injection', *Geophysical Prospecting*, 64(4), pp. 987–1000. Doi: 10.1111/1365-2478.12386.

Islam, M. A. and Skalle, P. (2013) 'An experimental investigation of shale mechanical properties through drained and undrained test mechanisms', *Rock Mechanics and Rock Engineering*, 46(6), pp. 1391–1413. Doi: 10.1007/s00603-013-0377-8.

IWASAKI, T., TATSUOKA, F. and TAKAGI, Y. (1978) 'Shear moduli of sands under cyclic torsional shear loading.', *SOILS AND FOUNDATIONS*, 18(1), pp. 39–56. Doi: 10.3208/sandf1972.18.39.

Jackson, I. and Paterson, M. S. (1987) 'Shear modulus and internal friction of calcite rocks at seismic frequencies: pressure, frequency and grain size dependence', *Physics of the Earth and Planetary Interiors*, 45(4), pp. 349–367. Doi: 10.1016/0031-9201(87)90042-2.

Kato, A., Onozuka, S. and Nakayama, T. (2008) 'Elastic property changes in a bitumen reservoir during steam injection', *The Leading Edge*, 27(9), pp. 1124–1131. Doi: 10.1190/1.2978974.

Ketineni, Sarath Pavan, et al. "Quantitative integration of 4D seismic with reservoir simulation." SPE Journal 25.04 (2020): 2055-2066.

King, M. S. (1966) ‘WAVE VELOCITIES IN ROCKS AS A FUNCTION OF CHANGES IN OVERBURDEN PRESSURE AND PORE FLUID SATURANTS’, *GEOPHYSICS*, 31(1), pp. 50–73. Doi: 10.1190/1.1439763.

King, M. S. (2000) ‘Biot dispersion for P- and S-wave velocities in partially and fully saturated sandstones’, *Geophysical Prospecting*, 48(6), p. 1075. Doi: 10.1046/j.1365-2478.2000.00221.x.

KLIMENTOS, T. (1991) ‘Geometric Corrections in Attenuation Measurements’, *Geophysical Prospecting*, 39(2), pp. 193–218. Doi: 10.1111/j.1365-2478.1991.tb00309.x.

Kobayashi, Y. (2015) ‘Seismic Wave Velocity and Attenuation in Rocks With Mesoscopic-Scale Heterogeneity’, *Stanford University*, 1(February), pp. 1689–1699. Doi: 10.1017/CBO9781107415324.004.

Koppelmann, J. (1958) ‘Über die Bestimmung des dynamischen Elastizitätsmoduls und des dynamischen Schubmoduls im Frequenzbereich von 10−5 bis 10−1 Hz’, *Rheologica Acta*, 1(1), pp. 20–28. Doi: 10.1007/BF01982279.

Lakes, R. (2009) *Viscoelastic Materials*. Cambridge: Cambridge University Press. Doi: 10.1017/CBO9780511626722.

Lebedev, M. *et al.* (2009) ‘Direct laboratory observation of patchy saturation and its effects on ultrasonic velocities’, *The Leading Edge*, 28(1), pp. 24–27. Doi: 10.1190/1.3064142.

Lei, X. and Xue, Z. (2009) ‘Ultrasonic velocity and attenuation during CO2 injection into water-saturated porous sandstone: Measurements using difference seismic tomography’, *Physics of the Earth and Planetary Interiors*, 176(3–4), pp. 224–234. Doi: 10.1016/j.pepi.2009.06.001.

Li, P. and Chalaturnyk, R. J. (2005) ‘Geomechanical Model of Oil Sands’, in *SPE International Thermal Operations and Heavy Oil Symposium*. Society of Petroleum Engineers, pp. 1–5. Doi: 10.2118/97949-MS.

Lienert, B. R. and Manghnani, M. H. (1990) 'The relationship between Q E −1 and dispersion in extensional modulus, E', *Geophysical Research Letters*, 17(6), pp. 677–680. Doi: 10.1029/GL017i006p00677.

Liu, H.-P. and Peselnick, L. (1983) 'Investigation of internal friction in fused quartz, steel, plexiglass, and westerly granite from 0.01 to 1.00 Hertz at 10 −8 to 10 −7 strain amplitude', *Journal of Geophysical Research*, 88(B3), p. 2367. Doi: 10.1029/JB088iB03p02367.

Lumley, D. E. (2001) 'Time-lapse seismic reservoir monitoring', *GEOPHYSICS*, 66(1), pp. 50–53. Doi: 10.1190/1.1444921.

Madonna, C. and Tisato, N. (2013) 'A new Seismic Wave Attenuation Module to experimentally measure low-frequency attenuation in extensional mode', *Geophysical Prospecting*, 61(2), pp. 302–314. Doi: 10.1111/1365-2478.12015.

Mavko, G., Mukerji, T. and Dvorkin, J. (2009) *The Rock Physics Handbook*. Cambridge: Cambridge University Press. Doi: 10.1017/CBO9780511626753.

Mavko, G. and Nur, A. (1975) 'Melt squirt in the asthenosphere', *Journal of Geophysical Research*, 80(11), pp. 1444–1448. Doi: 10.1029/JB080i011p01444.

Mikhaltsevitch, V., Lebedev, M. and Gurevich, B. (2014a) 'A laboratory study of low-frequency wave dispersion and attenuation in water-saturated sandstones', *The Leading Edge*, 33(6), pp. 616–622. Doi: 10.1190/tle33060616.1.

Mikhaltsevitch, V., Lebedev, M. and Gurevich, B. (2014b) 'Measurements of the elastic and anelastic properties of sandstone flooded with supercritical CO 2', *Geophysical Prospecting*, 62(6), pp. 1266–1277. Doi: 10.1111/1365-2478.12181.

Mikhaltsevitch, Vassily, et al. "A Laboratory Forced-Oscillation Apparatus for Measurements of Elastic and Anelastic Properties of Rocks at Seismic Frequencies." Frontiers in Earth Science 9 (2021): 155.

Mörig, R. and Burkhardt, H. (1989) 'Experimental evidence for the Biot-Gardner theory', *GEOPHYSICS*, 54(4), pp. 524–527. Doi: 10.1190/1.1442679.

Murphy, W. F. (1984) 'Acoustic measures of partial gas saturation in tight sandstones', *Journal of Geophysical Research: Solid Earth*, 89(B13), pp. 11549–11559. Doi: 10.1029/JB089iB13p11549.

Nakagawa, S. (2011) 'Split Hopkinson resonant bar test for sonic-frequency acoustic velocity and attenuation measurements of small, isotropic geological samples', *Review of Scientific Instruments*, 82(4), p. 044901. Doi: 10.1063/1.3579501.

O'Connell, R. J. and Budiansky, B. (1978) 'Measurements of dissipation in viscoelastic media', *Geophysical Research Letters*, 5(1), pp. 5–8. Doi: 10.1029/GL005i001p00005.

Osinga, S., Zambrano-Narvaez, G. and Chalaturnyk, R. . (2015) 'Study of geomechanical properties of 3D printed sandstone analogue', in *American Rock Mechanics Association*, pp. 15–547.

Paffenholz, J. and Burkhardt, H. (1989) 'Absorption and modulus measurements in the seismic frequency and strain range on partially saturated sedimentary rocks', *Journal of Geophysical Research*, 94(B7), p. 9493. Doi: 10.1029/JB094iB07p09493.

Raymer, L. L., Hunt, E. R. and Gardner, J. S. (1980) 'An Improved Sonic Transit Time-to-Porosity Transform', *SPWLA Annual Logging Symposium*, pp. 1–13.

Ruiz, F. and Cheng, A. (2010) 'A rock physics model for tight gas sand', *The Leading Edge*, 29(12), pp. 1484–1489. Doi: 10.1190/1.3525364.

Sayers, C. M. (2005) 'Sensitivity of elastic-wave velocities to stress changes in sandstones', *The Leading Edge*, 24(12), pp. 1262–1266. Doi: 10.1190/1.2149646.

Schijns, H., Jackson, I. and Schmitt, D. R. (2018) 'Shear Modulus Dispersion in Cracked and Fluid-Saturated Quartzites: Experimental Observations and Modeling', *Journal of Geophysical*

Research: Solid Earth, pp. 1–16. Doi: 10.1002/2017JB014633.

Schiltz, K., Zeigler, L. and Gray, D. (2014) 'Improved reservoir characterization and monitoring of the Long Lake heavy oil SAGD project using time-lapse multicomponent seismic data', *First Break*, 32(7), pp. 87–94.

Simmons, G. and Brace, W. F. (1965) 'Comparison of static and dynamic measurements of compressibility of rocks', *Journal of Geophysical Research*, 70(22), pp. 5649–5656. Doi: 10.1029/jz070i022p05649.

Spencer, J. W. (1981) 'Stress relaxations at low frequencies in fluid-saturated rocks: Attenuation and modulus dispersion', *Journal of Geophysical Research*, 86(B3), p. 1803. Doi: 10.1029/JB086iB03p01803.

Spencer, J. W., Cates, M. E. and Thompson, D. D. (1994) 'Frame moduli of unconsolidated sands and sandstones', *GEOPHYSICS*, 59(9), pp. 1352–1361. Doi: 10.1190/1.1443694.

Spencer, J. W. and Shine, J. (2016) 'Seismic wave attenuation and modulus dispersion in sandstones', *GEOPHYSICS*, 81(3), pp. D211–D231. Doi: 10.1190/geo2015-0342.1.

Subramaniyan, S. *et al.* (2014) 'An overview of laboratory apparatuses to measure seismic attenuation in reservoir rocks', *Geophysical Prospecting*, 62(6), pp. 1211–1223. Doi: 10.1111/1365-2478.12171.

Subramaniyan, S. *et al.* (2015) 'Laboratory-based seismic attenuation in Fontainebleau sandstone: Evidence of squirt flow', *Journal of Geophysical Research: Solid Earth*, 120(11), pp. 7526–7535. Doi: 10.1002/2015JB012290.

Szewczyk, D., Bauer, A. and Holt, R. M. (2016) 'A new laboratory apparatus for the measurement of seismic dispersion under deviatoric stress conditions', *Geophysical Prospecting*, 64(4), pp. 789–798. Doi: 10.1111/1365-2478.12425.

Szewczyk, D., Bauer, A. and Holt, R. M. (2018) 'Stress-dependent elastic properties of shales—laboratory experiments at seismic and ultrasonic frequencies', *Geophysical Journal International*, 212(1), pp. 189–210. Doi: 10.1093/gji/ggx392.

Takei, Y., Fujisawa, K. and McCarthy, C. (2011) 'Experimental study of attenuation and dispersion over a broad frequency range: 1. The apparatus', *Journal of Geophysical Research*, 116(B9), p. B09204. Doi: 10.1029/2011JB008382.

Takei, Y., Karasawa, F. and Yamauchi, H. (2014) 'Temperature, grain size, and chemical controls on polycrystal anelasticity over a broad frequency range extending into the seismic range', *Journal of Geophysical Research: Solid Earth*, 119(7), pp. 5414–5443. Doi: 10.1002/2014JB011146.

Tisato, N. *et al.* (2012) 'Experimental investigation of flash weakening in limestone', *Journal of Structural Geology*. Elsevier Ltd, 38, pp. 183–199. Doi: 10.1016/j.jsg.2011.11.017.

Tisato, N. and Madonna, C. (2012) 'Attenuation at low seismic frequencies in partially saturated rocks: Measurements and description of a new apparatus', *Journal of Applied Geophysics*, 86, pp. 44–53. Doi: 10.1016/j.jappgeo.2012.07.008.

Tisato, N. and Quintal, B. (2014) 'Laboratory measurements of seismic attenuation in sandstone: Strain versus fluid saturation effects', *Geophysics*, 79(5), pp. WB9–WB14. Doi: 10.1190/geo2013-0419.1.

Tisato, N., Zhao, Q. and Grasselli, G. (2016) 'Experimental rock physics under micro-CT', *SEG Technical Program Expanded Abstracts 2016*, (September), pp. 3251–3255. Doi: 10.1190/segam2016-13949603.1.

Toksöz, M. N. *et al.* (1976) 'Velocities of Seismic Waves in Porous Rocks', *Geophysics*, 41(4), pp. 621–645. Doi: 10.1190/1.1440639.

Toms, J. *et al.* (2006) 'Comparative review of theoretical models for elastic wave attenuation and dispersion in partially saturated rocks', *Soil Dynamics and Earthquake Engineering*, 26(6–7), pp.

548–565. Doi: 10.1016/j.soildyn.2006.01.008.

Tutuncu, A. N., Podio, A. L. and Sharma, M. M. (1998) 'Nonlinear viscoelastic behavior of sedimentary rocks, Part II: Hysteresis effects and influence of type of fluid on elastic moduli', *GEOPHYSICS*, 63(1), pp. 195–203. Doi: 10.1190/1.1444313.

Vanorio, T., Nur, A. and Ebert, Y. (2011) 'Rock physics analysis and time-lapse rock imaging of geochemical effects due to the injection of CO2 into reservoir rocks', *Geophysics*, 76(5), pp. O23–O33. Doi: 10.1190/geo2010-0390.1.

Vidal-Gilbert, S., Nauroy, J.-F. and Brosse, E. (2009) '3D geomechanical modelling for CO2 geologic storage in the Dogger carbonates of the Paris Basin', *International Journal of Greenhouse Gas Control*, 3(3), pp. 288–299. Doi: 10.1016/j.ijggc.2008.10.004.

Walsh, J. B. (1965) 'The effect of cracks on the uniaxial elastic compression of rocks', *Journal of Geophysical Research*, 70(2), pp. 399–411. Doi: 10.1029/jz070i002p00399.

Wang, Z. (1997) 'Feasibility of time-lapse seismic reservoir monitoring: The physical basis', *The Leading Edge*, 16(9), pp. 1327–1330. Doi: 10.1190/1.1437796.

Wang, Z. (Zee) (1988) *Wave velocities in hydrocarbons and hydrocarbon saturated rocks*.

Wang, Z. (Zee) (2001) 'Fundamentals of seismic rock physics', *GEOPHYSICS*, 66(2), pp. 398–412. Doi: 10.1190/1.1444931.

White, J. E. (1975) 'Computed Seismic Speeds and Attenuation in Rocks With Partial Gas Saturation.', *Geophysics*, 40(2), pp. 224–232. Doi: 10.1190/1.1440520.

Winkler, K. and Nur, A. (1979) 'Pore fluids and seismic attenuation in rocks', *Geophysical Research Letters*, 6(1), pp. 1–4. Doi: 10.1029/GL006i001p00001.

Winkler, K., Nur, A. and Gladwin, M. (1979) 'Friction and seismic attenuation in rocks', *Nature*,

277(5697), pp. 528–531. Doi: 10.1038/277528a0.

Winkler, K. W. and Nur, A. (1982) ‘Seismic attenuation: Effects of pore fluids and frictional-sliding’, *GEOPHYSICS*, 47(1), pp. 1–15. Doi: 10.1190/1.1441276.

Wyllie, M. R. J., Gregory, A. R. and Gardner, G. H. F. (1958) ‘AN EXPERIMENTAL INVESTIGATION OF FACTORS AFFECTING ELASTIC WAVE VELOCITIES IN POROUS MEDIA’, *GEOPHYSICS*, 23(3), pp. 459–493. doi: 10.1190/1.1438493.

Xu, S. and White, R. E. (1995) ‘A new velocity model for clay-sand mixtures’, *Geophysical Prospecting*, 43(1), pp. 91–118. doi: 10.1111/j.1365-2478.1995.tb00126.x.

Yee, A. F. and Takemori, M. T. (1982) ‘Dynamic bulk and shear relaxation in glassy polymers. I. Experimental techniques and results on PMMA’, *Journal of Polymer Science: Polymer Physics Edition*, 20(2), pp. 205–224. doi: 10.1002/pol.1982.180200204.

Zemanek, J. and Rudnick, I. (1961) ‘Attenuation and Dispersion of Elastic Waves in a Cylindrical Bar’, *The Journal of the Acoustical Society of America*, 33(10), pp. 1283–1288. doi: 10.1121/1.1908417.

Zhang, B. and Okuno, R. (2015) ‘Modeling of capacitance flow behavior in EOS compositional simulation’, *Journal of Petroleum Science and Engineering*. Elsevier, 131, pp. 96–113. doi: 10.1016/j.petrol.2015.04.014.

Zou, Y. *et al.* (2005) *Integration of seismic methods with reservoir simulation, Pikes Peak heavy-oil field, Saskatchewan*, *The Leading Edge*. doi: 10.1190/1.2210076.

APPENDIX A Dynamic Triaxial Cell System Set-up Installation

This section introduces the installation procedures. The installation procedures were modified to have faster and fewer steps to keep specimens frozen. All sensors are finely adjusted to make sure accurate during the seismic frequencies testing. The main steps of setting up a dynamic triaxial cell system are summarized below:

1. Make sure the base plate is sitting on the MTS actuator (0.01 Hz to 20 Hz).
2. Remove all the fittings on the bottom ram and move the crosshead to create 44 inches to make enough room for the installation.
3. Install the spanner.
4. Install the two thrust nut retainers, the LVDT holder, and a temporary 30° angle cap with vacuum grease applied.
5. Install the sealing plate and install sealing plate retainer over the ram, mind ¼ inch NPT fitting alignment towards Swagelok ¼" line.
6. Install sealing plate retainer between sealing plate and LVDT holder then move the sealing, sealing plate retainer and LVDT holder to the lowest position on the ram.
7. Remove the temporary 30°angle cap (3/16 allen key will be used) and bottom pore stone.
8. Install membrane and o-rings onto specimen, place specimen on the ram.
9. Roll down the bottom of the membrane and 2 to 3 o-rings.
10. Place cell onto the bottom sealing plate and two people push down to engage o-rings.
11. Install the split rings at the bottom, ensure split rings are matched. Finger tight the ¼ inch locking screws.
12. Install and grease o-rings on the top of the sealing plate.
13. Install two o-rings for membrane sealing on top ram.
14. Move down the MTS crosshead until the gap between the top of the specimen and ram is enough to slide in pore stone.
15. Slide-in pore stone.
16. Remove locknut retainers (7/16 spanner).
17. Use special vice grips to lock the ram in position with a window open and perpendicular to the crosshead. The Vice grips handle must rest against the left steel pillar.

18. With two people: one person holds the cell body to prevent cell body rotation. Another person turns the thrust nut with a spanner to close the distance between the top pore stone and ram. Ensure alignment of specimen and pore stone and ram.
19. Roll up the membrane over top ram, roll down o-rings to help seal. Use a spatula to help.
20. Have a 9/16 wrench ready. Two people lift the cell body, then pass over the o-ring at the top sealing plate, and close the gap.
21. Lock the bottom sealing plate retainer to hold the cell in place.
22. Ensure split rings are matching, install the top split ring for final cell closing. Use a rubber mallet to help with closing the split ring. Finger tight the split ring clasp.
23. Turn thrust nut clockwise to move sample up and touch the top ram (with ~200N load on the sample)
24. Remove the sealing plate retainer (9/16 wrench).
25. Move LVDT holder to 1 inch above the ram ports. Lock in place with 1/8 allen key.
26. Install fittings for bottom pressure onto the bottom of ram. One 1/8 inch NPT to ¼ inch Swagelok elbow for bottom pore pressure (line 4) and connect line.
27. Connect line 2 (top pore pressure); Connect line 5 (cell pressure); Connect line 6 (relief cell pressure).
28. Install LVDT into the holder.
29. Remove vice grips.
30. Open V5 and V6. Fill the cell with silicon oil using pump 1. Both the fill and deliver valves are open on the Quizix pump program and are directly connected to the oil reservoir.
31. Increase confining pressure to 200 kPa.
32. Increase axial load to 200 kPa while the sample is still frozen.
33. Increase confining stress and axial stress in 100 kPa increments to 500 kPa total.
34. Monitor line 6 for fluid, once oil flows, the cell is full. Close V6. Close fill valve on Quizix software.
35. Place vibration pad in front of MTS machine.
36. Install the laser displacement sensor frame in front of the machine. Adjust sensor positions using beams and locks on the frame to the rough position.
37. Slide frame so laser sensors fit into cell window. Hold the frame in place with sandbags.
38. Connect laser sensor cable.

39. Turn on the power, wait approximately 30 minutes before using the LK-G5000 Series. The circuit is not stable immediately after the power is turned on, the measured value may gradually change during this period. Check signal, check height etc.
40. Adjust sensors to final position using fine-tuning dials using readings on data logger to read 0.

APPENDIX B Back Saturation

1. Melting at cell pressure 500 kpa and pore pressure 200 kpa.
2. Open the Quizix PumpWorks software to operate all pressure pumps.
3. Start the GeoREF Feedback Datalogger to record both the pressure and volume values of confining (Pump1) and pore pressure (Pump2).
4. Ensure the axial load is at 0.9 kN (600 kPa axial stress, this is the stress level after the vacuum).
5. Open V5 to connect the pump to cell. Increase cell pressure to 400 kPa.
6. Open V1, V3, and V2 to Q and V4 to Q to connect top and bottom pore pressure lines to the Quizix pump. Increase pore pressure to 100 kPa.
7. Incrementally increase cell pressure (confining/radial stress), axial load (axial stress) and pore pressure respectively in 100 kPa increments. First, increase confining stress 100 kPa, then axial load/stress 100 kPa, then pore pressure 100 kPa until pore pressure reaches in-situ stress condition (pore pressure 2000kPa). For the final confining stress and axial load increment, do not increase the axial stress until equilibrium for confining pressure and pore pressure are reached (Poisson's ratio will add some vertical load). Once equilibrium is reached make the final axial load increment to the final axial stress requirement. CAUTION: to increase the force, may need a snipe bar/extension arm to turn the thrust nut spanner wrench (Figure 6. 2).
8. Hold the system for a minimum 12-hour period (or overnight) to achieve full-back saturation for the specimen (the confining pressure is at 2200 kPa and the back pressure is at 2000 kPa).

Figure B The picture of snipe bar/extension arm to turn thrust nut spanner wrench when applied axial force to the sample.

APPENDIX C B-test

1. Stop Quizix Pump 2 (Figure C) and close the delivery valve (Cylinder 2B).
2. Increase the Quizix Pump 1 (cell pressure) by 100 kPa to 2300 kPa. Wait for confining pressure equilibrium. Then increase axial stress to 2300 kPa (total effective stress increment of 100 kPa).
3. Monitor pore pressure increment on GeoREF logger back pressure sensor graph/log. Once the pore pressure reaches equilibrium, the first stage of the B-Test is complete.
4. Repeat the previous step; increase the confining pressure and cell pressure incrementally (in 100 kPa increments) to reach: 2500 kPa, 3200 kPa, and 4500 kPa (first increment cell pressure, then increment axial load in 100 kPa increments – 2 people are helpful for this) to obtain the effective stress σ' of 500, 1200, and 2500 kPa, respectively.
5. The confining pressure and back pressure values are recorded and used to calculate the degree of saturation.
6. Decrease axial stress and confining pressure. Unload confining stress first, then unload axial stress in 100 kPa increments. Stop at 2200 kPa axial stress and confining pressure.
7. Set Quizix pump pressure to 2000 kPa, open the Quizix pump delivery valve.
8. End of B-test.

   B value is equal to the ratio of the change of the pore pressure and the change of the confining pressure. For this case, the B value should be greater than 0.91.

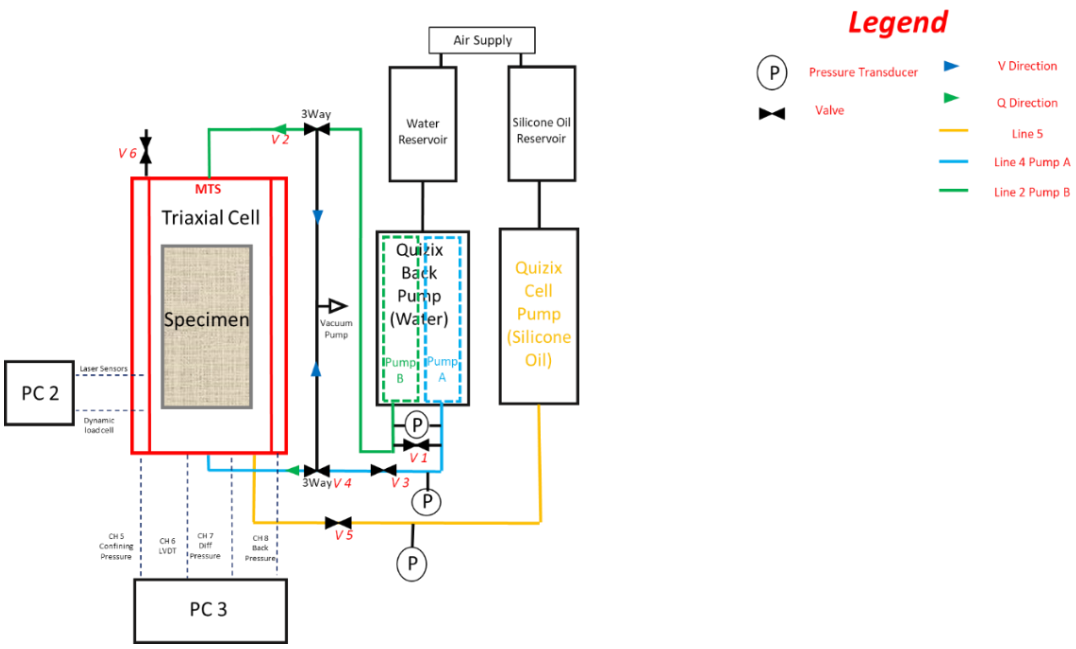

Figure C Schematic of the seismic dynamic measurement system.

APPENDIX D Isotropie Consolidation (K0=1)

1. Determine final axial and confining stress levels required for testing (should know prior to starting).
2. Incrementally increase Pump 1 cell pressure and axial stress in 100 kPa increments until final isotropic stress is reached. Be aware of the failure stress state of the specimen and do not fail the specimen. See Table 6-1for axial force load to stress conversion for 63.5mm diameter specimen.

   Test 1: total axial and confining stress = 2500 kPa. Isotropic effective stress σ′ of 500 kPa

   Test 2: total axial and confining stress = 3200 kPa. Isotropic effective stress σ′ of 1200 kPa

   Test 3: total axial and confining stress = 4500 kPa. Isotropic effective stress σ′ of 2500 kPa

Table D Pressure to Force conversion for 63.5mm diameter specimen.

Conf. Pressure (kPa)	MTS Axial load (KN)
1000	3.17
1500	4.75
2000	6.33
2500	7.92
3000	9.50
3500	11.08
4000	12.67
4500	14.25

In the course of stress loading for consolidation, if the volume on the backpressure pump (Quizix Pump Cylinder 2B) is stable, the next axial and radial stress increment can be

applied. Monitor and record each volume change in the backpressure pump during each corresponding confining pressure.

APPENDIX E Constant Pressure/Head Permeability Test (Flow bottom to top, then top to the bottom)

1. Close V2 and V4.
2. Lower the pump's pressure. Open the fill valves. Refill Quizix Pump 2 Cylinder A and Cylinder B so they are both at ~270mL (Cylinder 2A and 2B are ~50% full).
3. Set Quizix Pump 2 Cylinder A and Cylinder B to IND CP Mode. Set pressure in Pump 2 Cylinder A and Cylinder B to the current sample pore pressure (2000 kPa). Start pumps.
3. Open Pump 2 Cylinder A to deliver and Cylinder B to deliver.
4. Close V1 (bypass valve).
5. Open V2 and V4 to position Q.
6. Set Quizix Pump 2 Cylinder B (Line 2 Top) to 2000 kPa, start the pump.
7. Set Quizix Pump 2 Cylinder A to IND CR and Extend (Line 4 Bottom) and set to constant rate to 5 mL/min. Start Pump. Increment at 2 mL/min every 15s until a differential of 5 kPa is reached. Run the test until cylinder 2B has 10 mL of volume remaining.
8. Monitor differential pressure and wait for equilibrium.
   Permeability - Flow top to bottom
9. Set Quizix Pump 2 Cylinder B to IND CP and set to (Line 4 Bot) to 2000 kPa, start the pump. (Drop too fast, lower from 20ml/min to 5 ml/min).
10. Set Quizix Pump 2 Cylinder A to IND CR and set to Extend (Line 2 Top). Set to constant rate to 5 mL/min and start the pump. Increment at 2 mL/min every 15s until a differential of 5 kPa is reached. Run the test until cylinder 2A has 10 mL of volume remaining.
11. Perm Test, stop Quizix Pump 2. Set pore pressure to 2000 kPa and start the pump. Open by-pass valve V1 and let the pore pressure system be stable.
    D'Arcy's law is:

$$k = \frac{\mu q L}{\Delta p A}$$

APPENDIX F Dynamic Triaxial Test Increase Axial Load for Deviator Stress Application

1. Increase axial load with thrust nut to desired strain. Turn Nut (clockwise increase, counter-clockwise to decrease) to desired force or strain and monitor load cell or displacement LVDT reading.
2. Decrease axial load with thrust nut to “0” stress with the same as increasing loading rate.
3. Increase axial load with thrust nut to desired strain as step 1.
4. Monitor and record volume change of Quizix Pump 1 to track bulk volume change of specimen.
5. Monitor and record volume change of Quizix Pump 2 to track pore volume change of specimen.

NOTE: Pump volume and axial displacement required for total volume change of specimen. The pore volume change and total volume change can be used to calculate Biot’s coefficient, data may not be sensitive enough for this calculation.

APPENDIX G Dynamic Triaxial Test

1. Turn on DCS-100 dynamic load cell software (PC2).
2. Increase axial stress increment at determined load by moving ram with thrust nut.
3. Start the MTS system and move the actuator slowly with the Landmark MTS (PC1) software until the reading of the dynamic load cell is -3kN (PC2), monitor change in static MTS load cell, ensure you are at desired load.
4. Input the required dynamic load parameter to the Landmark MTS software. The test requires amplitude, force/strain control, frequency.
5. Run the cyclic test at the required frequencies.
6. Stop the Landmark MTS system, which will unload the actuator.
7. Repeat steps from 1 to 5 if more testing is required.